University of Cagliari

PhD Degree
Industrial Engineering
Cycle XXXII

COMPRESSIVE SENSING-BASED METHODOLOGIES FOR SMART GRID MONITORING

Scientific Disciplinary Sector:
ING-INF/07

PhD Student:	**Ing. Daniele Carta**
Coordinator of the PhD Programme:	**Prof. Ing. Francesco Aymerich**
Supervisor:	**Prof. Ing. Sara Sulis**
Co-Supervisor:	**Prof. Ing. Paolo Attilio Pegoraro**

Dedicated to
Federica

Contents

Introduction

Modern distribution networks are currently subjected to a deep change. Originally meant only to distribute the electric energy to the consumers, nowadays, due to the deregulation of the energy market and the massive penetration of unplanned generation units directly connected to both Medium and Low Voltage levels (respectively MV and LV), an increasing presence of aleatory generation provided by renewable energy sources is deeply modifying the original concept of distribution networks.

All these aspects are transforming the distribution grid from a passive network to a highly complex active system, thus leading to new management, control and protection issues. Significant intermittency on generations and loads is expected, with important consequences on how intensively the electric grid may be exploited. Nevertheless, it is worth underlining that these factors, if properly managed, have the potentiality to bring important benefits to the electric systems, in terms of reliable and efficient operation. In this scenario, which we commonly refers to with the term *Smart Grid*, the use of an accurate, effective, and real-time monitoring of the electric grid status is mandatory to pursue the goal of a strong modernization of the management and control tools.

The possibility to perform an efficient management and control of the distribution grids strictly depends on the capability to achieve an accurate knowledge of the real operating conditions of the system. This, as an example, can prevent wrong decisions by the distribution management system and can allow avoiding needless actions aimed at keeping too conservative safety margins. An accurate snapshot of the operating conditions of the electric systems could be obtained by means of measurements gathered from the field, which permit to estimate the most probable network conditions at a given time. Now, in distribution systems, the penetration of measurement and monitoring devices is usually minimal. In general, to address the poor installation of measurement devices, a commonly adopted solution is to use historical and statistical data to obtain the so-called "pseudo-measurements". Despite the importance of these pseudo-measurements to get information necessary for observability, it is clear that their limited ac-

curacy (commonly pseudo-measurements are associated with 50% of tolerance) cannot lead to the achievement of high accuracies in the results.

Since the operation of every management or control tool is based on the processing of the measurements collected from the grid, a key role to obtain accurate results is played by the metrological characteristics of the deployed instrumentation but also by the measurement infrastructure available on the field. For example, it is known that when a fault occurs into the system, both voltage and current signals are characterized by high dynamics, and magnitude variations. These working scenarios denote particularly stressful conditions for the measurement devices, leading to a decrement in the measurement accuracies, and thus in the performance of the implemented Fault Location (FL) procedures. Similar considerations hold for the harmonic analysis, necessary to monitor one of the main Power Quality (PQ) phenomena in distribution systems, the harmonic pollution. It is well known that the presence of harmonics affects the performance of the equipment, for example decreasing their lifetime. The accurate detection of the polluting sources is useful for the grid operator, since these disturbances are spread through the whole system involving all devices connected to the same nodes, and it can help in the mitigation process, also reducing the maintenance costs. Based also on the well-known State Estimation (SE) principles, harmonic State Estimation solutions have been proposed, in order to estimate the harmonic levels in the system. In the distribution grid scenario, this type of analysis suffers the same problems of lack of measurements from the field as other applications and analysis.

In Smart Grid perspective, it is therefore evident that an upgrade in number and quality of the measurements usable in FL and harmonic sources estimation techniques is absolutely needed. From this point of view, the increasing presence of new smart meters could also be considered. Their number is rapidly increasing and, moreover, they can provide PQ information, surely useful to estimate the harmonic sources of the grid. In this regard, from one side, many instruments would be important to get distributed information on the electrical quantities in different points of the network, and to ensure robustness with respect to possible malfunctions of measurement system components. On the other hand, different type of measurement devices, with different quantities monitored and different (or even absent) synchronization capabilities, must be appropriately considered, in order to make the use of these various information possible and effective. Thus, intense research activity is necessary to use all the available information in the best way for the achievement of given accuracy targets.

In lasts years, an increasing interest raised on the use of the Phasor Measurement Units (PMUs) for distribution system applications. The PMUs are new generation devices, able to provide accurate measurements of voltage and

current phasors, frequency and rate of change of frequency, synchronized with respect to the Coordinated Universal Time (UTC). The use of the common time reference allows the comparison of the synchronized measurements performed in different remote points of the network. Considering the expected continuous variations of the status of modern distribution systems, the possibility to use synchronized measurement can play a key role in obtaining an accurate monitoring of the system. Despite all the benefits that these instruments can bring to the analysis on distribution networks, a large scale deployment is currently thwarted by the high cost of these devices. Currently, the overall estimated costs for installing a PMU can vary between $ 10000 and $ 30000, of which hardware cost is around $ 5000. Nevertheless, the costs of these instruments are nowadays decreasing, thus, it is reasonable to consider that the cost will decrease even more in the near future and the use in distribution systems will become really possible.

It is important to remember that the PMUs were originally designed for the transmission systems monitoring, as a consequence, the expected "measurand" signals were basically sinusoidal. Nowadays, thanks to the new reference standards, these instruments also need to demonstrate their capacity to measure dynamic signals, by combining a high reporting rate with the use of proper algorithms. Nonetheless, current commercial PMUs do not permit accurate power quality monitoring and harmonic sources estimation. In this regard, solutions for developing harmonic PMUs are currently under study.

In this context, new algorithms and methodologies capable to perform accurate FL and harmonic sources estimation with the available measurement devices, in a cost-saving environment and considering the specificity of the new distribution system scenario, are needed.

In this regard, in the last years, the theory of Compressive Sensing (CS) has raised as an alternative method to reconstruct incomplete signals in presence of a limited number of measurements. For its application, CS has only two main requirements: the signal to be recovered must be sparse (which means having only few non-zero components with respect to the size of the signal itself) and the availability of a minimum number of information, depending on both the size of the system and the sparsity level. This second requirement matches distribution systems conditions since they are generally characterized by a limited number of measurements. Instead, the satisfaction of the first requirement depends on the problem under study. With particular reference to fault location and the identification of prevailing harmonic sources, it is possible to affirm that both can be considered as sparse problems. In fact, the number of faults occurring contemporaneously into the system is limited and, considering the large size of the distribution networks, it is way lower than the dimension of the system

itself. Same considerations hold for the identification of the harmonic sources. The number of actual polluting loads/sources (at least the main ones) is lower than the number of loads connected to the system and thus, the model of the system can be considered as sparse.

The monitoring applications, in charge to perform FL and harmonic sources estimation, should be designed to appropriately use the best available information for any evaluation, suitably considering measurement uncertainty sources, synchronization levels, and so on. Only in this case, the estimation results could be used in order to support appropriately possible management decisions.

This thesis is the result of a deep research activity on the study, and the analysis, of Compressive Senging-based methodologies for the accurate estimation of the harmonic sources and the fault location in modern distribution systems. In Chapter 1, the fundamentals of Compressive Sensing (CS) are presented, in other to give the reader a basic knowledge of this innovative technique. In Chapter 2 a CS solution for the identification of the main harmonic sources in a distribution network is presented. Finally, Chapter 3 deals with the impact of the measurement accuracies on a CS-based fault location algorithm and discusses a proposal for an effective fault location approach in realistic measurement scenarios.

"Engineering isn't about perfect solutions, it's about doing the best you can with limited resources."

Randy Pausch, The Last Lecture

Chapter 1

Compressive Sensing

Compressive Sensing (CS), also called Compressed Sensing, is a mathematical technique whose name derives from the discovery that it was possible to sense a signal from a limited, and thus compressed, set of information.

Before this intuition, any data reconstruction method was governed by the well-known works of Nyquist and Shannon [1, 2]. According to these principles, the full recovery of a bandwidth-limited signal needed a set of information sampled at the Nyquist rate, which must have been twice the maximum frequency of the signal of interest. The required number of samples, derived from this approach, was not always easy to get, due to high costs and the physical limitations. Such limitation from the signal processing point of view, was in contrast with the increase of the available computational power.

Alternative techniques based on the compression, such as the transform coding, leaded to the sparse approximation, which in turn leaded to compressibility schemes, and standards, such as JPEG, MP3 and so on. Nevertheless, it has to be notice that in these cases, the compression implied the loss of information, considered not important for the final goal (such has frequency components of a song, not included in the frequency range of human hearing).

Then, in 2004 by a pure chance, a former student of Donoho, Emmanuel Candes, while working on magneto resonance imaging, was able to perfectly reconstruct an image from undersampled data. From that episode, and thanks to the help of the Field medallist, Candes was able to outline the general theory of compressive sensing. Since then, compressive sensing completely renewed the idea behind the sampling of a signal. Instead of sampling at high rates and post-compressing the samples, CS suggests to directly sense the data in a compressed form. In particular, the amount of data needed for a robust signal recovery is directly proportional to some characteristics of both signal and system representation. This enables a large reduction in the sampling require-

ments and, consequently, the opportunity to develop new sensors and standards based on lower computational costs. Nowadays, CS is applied to many different fields and applications: astronomy, biology, medicine, power systems, radars, statistics, and so on.

Due to the complexity of CS theory, in this chapter, the general concepts will be introduced with an increasing level of complexity.

1.1 Norm definitions

The use of the ℓ_p-norm is a key point in the CS theory, thus, before to proceed, a brief introduction on the norms is mandatory.

Definition 1.1.1. Given a Euclidean space $\mathcal{R}$ of dimension n, for $1 \leq p < \infty$, the Lebesgue ℓ_p-norm of a vector $\mathbf{x} = (x_1, x_2, \ldots, x_i, \ldots, x_n) \in \mathcal{R}^n$ is defined as:

$$\|\mathbf{x}\|_p = \left(\sum_{i=1}^{n} |x_i|^p \right)^{\frac{1}{p}} \tag{1.1}$$

and it must follow the following properties:

- $\|\mathbf{x}\| \geq 0$ for each $\mathbf{x} \in \mathbb{R}^n$ and $\|\mathbf{x}\| = 0$ is and only if $\mathbf{0} = 0$;

- $\|\alpha\mathbf{x}\| = |\alpha| \|\mathbf{x}\|$ for each $\mathbf{x} \in \mathbb{R}^n$ and for each $\alpha \in \mathbb{R}^n$;

- $\|\mathbf{x} + \mathbf{y}\| \leq \|\mathbf{x}\| + \|\mathbf{y}\|$ for every $\mathbf{x}, \mathbf{y} \in \mathbb{R}^n$.

The ℓ_p-norm of a vector, can be seen as a function which measure the distances between points or the length of a vector. Different values of p correspond to different meaning of each measurement.

The ℓ_1-norm is often called "Manhattan Distance", and it corresponds to the sum of the magnitudes of the vectors in the space. It is also used to measure the distance between two vectors, by summing the absolute difference of the components of each vector.

$$\|\mathbf{x}\|_1 = \sum_{i=1}^{n} |x_i| \tag{1.2}$$

By setting $p = 2$, it is possible to obtain the more famous "Euclidean" norm (ℓ_2). It is the square root of the sum of the squares of the components of the vector. It is commonly used to measure the magnitude of a vector, and it gives the shortest distance between two points.

$$\|\mathbf{x}\|_2 = \sqrt{\sum_{i=1}^{n} |x_i|^2} \tag{1.3}$$

Moreover, by considering the definition of inner product between two vectors $\mathbf{x}$ and $\mathbf{y}$:

$$\langle \mathbf{x}, \mathbf{y} \rangle = \mathbf{y}^T \mathbf{x} = \sum_{i=1}^{n} x_i y_i \tag{1.4}$$

it is possible to see that it leads to the ℓ_2-norm: $\|\mathbf{x}\|_2 = \sqrt{\langle \mathbf{x}, \mathbf{x} \rangle}$.

Another interesting norm is the ℓ_∞. It is obtained by setting $p = \infty$ and it gives the absolute value of the largest magnitude among all elements of a vector.

$$\|\mathbf{x}\|_\infty = \max_{i=1,2,..,n} |x_i|^2 \tag{1.5}$$

In figure 1.1, these three norms are represented graphically in relation to the unit spheres in $\mathbb{R}^2$.
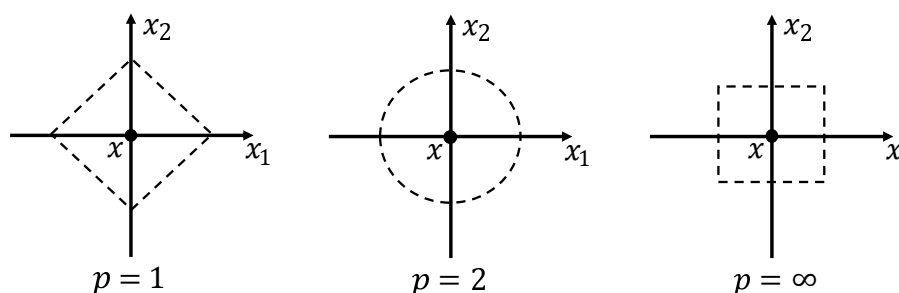
Figure 1.1: Unit spheres for ℓ_p norms with $p = 1$, $p = 2$, and $p = \infty$.

In the CS context it is useful to extend the notion of norm also for $p = 0$. This particular norm cannot be properly called as "norm", since it does not respect all the properties of the norms. For example, scaling its argument by a positive constant does not change the "norm". Due to this, the ℓ_0-norm is also known as "quasi-norm", and it is defined as the limit of the ℓ_p-norm, for $p \to 0$, and it counts the number of non-zero entries in a vector.

$$\|\mathbf{x}\|_0 = \lim_{p \to 0} \|\mathbf{x}\|_p^p = \lim_{p \to 0} \sum_{i=1}^{n} |x_i|^p \tag{1.6}$$

In many engineering problems, norms are used to measure the approximation error, thus the residuals, for problems in the form $argmin_{\mathbf{x} \in \mathbb{R}} \|\mathbf{x} - \hat{\mathbf{x}}\|_p$, where $\hat{\mathbf{x}}$ denotes the approximated vector. It is intuitive that different norms give different measurements, thus different residuals.

In figure 1.2, the research of the optimal approximation of the point x belonging to the set $\mathbb{H}$ (represented by the line) is shown by means of different norms. Once the set $\mathbb{H}$ is defined according to the constraints, minimizing the ℓ_p-norm is equivalent to increase the size of the ℓ_p-sphere centred in the point

x, until it intersects the line $\mathbb{H}$. The intersection point $\hat{x}$ will correspond to the minimum ℓ_p-norm point which satisfies all the constraints, and best approximates x. By comparing the selected points in figure 1.2, it can be seen that only when considering $p = 1$ and $p = \frac{1}{2}$, the minimum norm point, $\hat{x}$, is characterized by only one component different than zero, which in general holds for any ℓ_p-norm with $p \leq 1$. It has to be notice that, among these, the ℓ_1-norm is also the only convex norm since the linking segment between any two point, taken inside the sphere, is always fully included in the sphere, as shown in figure 1.3. Only the ℓ_1 norm keeps both convex and sparse characteristics [3].
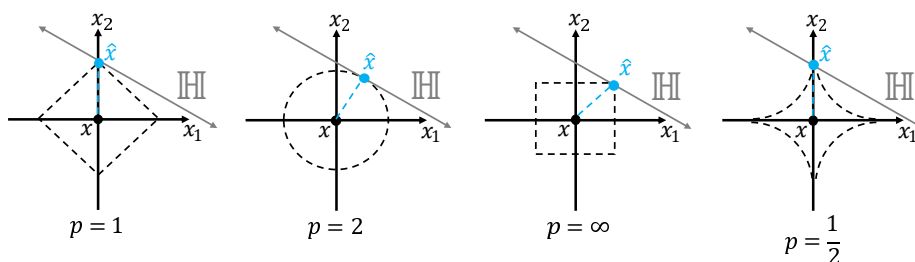
Figure 1.2: Best approximation of a point by using a one-dimensional subspace obtained with different norms [4].
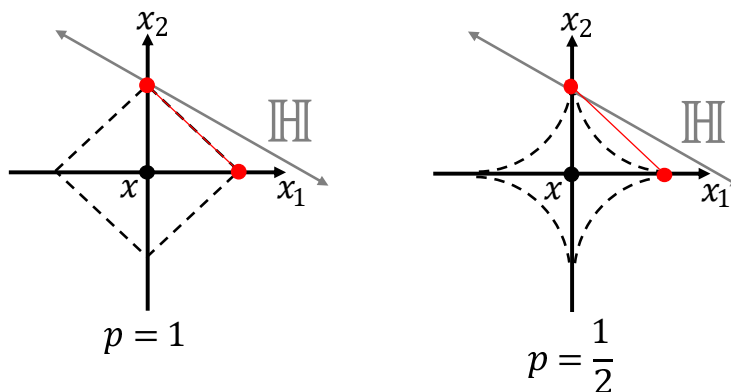
Figure 1.3: Graphic representation of convex property for norm ℓ_1 and $\ell_{\frac{1}{2}}$.

1.2 General theory

Now that some norm theory has been presented, it is possible to proceed with the CS discussion. As starting point, let consider a system in the form

$$\mathbf{y} = \mathbf{A}\mathbf{u} \tag{1.7}$$

where $\mathbf{u} \in \mathbb{R}^n$ is a vector representing the state of the system, $\mathbf{y} \in \mathbb{R}^m$ is the measurements vector, and $\mathbf{A} \in \mathbb{R}^{m \times n}$ is the measurement matrix. When (1.7) is

overdetermined, $m \geq n$, the system can be easily solved, and the trivial solution is unique if the columns of the measurement matrix are linearly independent. Instead, when $m < n$, thus (1.7) is underdetermined, the system is characterized by an infinite number of possible solutions.

In this thesis, we focus on the analysis of underdetermined systems, which are common when studying distribution electric systems. In order to solve these kind of problems, additional information, such as constraints, must be considered. In the CS case, the considered constraint is that only few entries of the vector $\mathbf{u}$ are different than zero. We refer to this peculiarity of the state vector by defining the sparsity of the system, S.

Definition 1.2.1. A vector $\mathbf{u} \in \mathbb{R}^n$ is sparse if $\|\mathbf{u}\|_0 \ll n$, where $\|\cdot\|_\alpha$ denotes the ℓ_α norm. In particular, it is defined S-sparse when it has at most S non-zero entries such that $\|\mathbf{u}\|_0 \leq S < n$.

Consequently, given an S-sparse vector $\mathbf{u}$ it is possible to define the set of all the S-sparse vectors as:

$$\Sigma_S = \{\mathbf{u} : \|\mathbf{u}\|_0 \leq S\} \tag{1.8}$$

Obviously, in the reality, not all the vectors are sparse as in Definition 1.2.1. It is possible that a non-sparse vector admit a sparse representation when represented in a different base, and thus Definition 1.2.1 holds with reference to the new base. In general, the measurement matrix corresponding to the base which allows to represent the state vector as sparse, is also called "sensing matrix". Furthermore, it is worth underlying that some vectors are characterized by entries with different order of magnitude. In these cases, for example, the entries with lower value can be neglected, and considered as if they are zeros. These vectors are termed compressible, approximately sparse or relatively sparse. In particular, when their entries are sorted in a decreasing order based on the magnitudes, they decay according to a power law.

Definition 1.2.2. A vector $\mathbf{u}$ is compressible if there exist two positive constants, $c > 0$ and $r > 1$, which verify the following inequality:

$$\|\mathbf{u} - \hat{\mathbf{u}}\|_p \leq cS^{-r} \tag{1.9}$$

where $\hat{\mathbf{u}}$ denotes the sparse approximation of $\mathbf{u}$.

Definition 1.2.3. Given a vector $\mathbf{u}$ and its sparse approximation $\hat{\mathbf{u}} \in \Sigma_S$, the compressibility of the original vector can be quantified by evaluating the approximation error:

$$\sigma_S(\mathbf{u})_p = \min_{\hat{\mathbf{u}}} \|\mathbf{u} - \hat{\mathbf{u}}\|_p \tag{1.10}$$

It is clear that the minimum in (1.10) can be easily reached by keeping only the higher magnitude entries of $\mathbf{u}$ while replacing the others with zeros, whereas if $\mathbf{u} \in \Sigma_S$, then $\sigma_S(\mathbf{u})_p = 0$ for any p. Both (1.9) and (1.10) are valid for any ℓ_p norm, and thus the optimal approximation is always valid.

1.3 Null Space

In order to distinguish between two different vectors $\mathbf{u}_1$ and $\mathbf{u}_2$, it is clear that the corresponding set of measurements must be different, $\mathbf{y}_1 \neq \mathbf{y}_2$, and thus $\mathbf{A}\mathbf{u}_1 \neq \mathbf{A}\mathbf{u}_2$. The ability of distinguish between two different state vectors depends on the null space of the matrix $\mathbf{A}$:

$$\mathcal{N}(\mathbf{A}) = \{\mathbf{z} : \mathbf{A}\mathbf{z} = 0\} \tag{1.11}$$

In particular, it is possible to observe that $\mathbf{A}$ uniquely represents all state vectors $\mathbf{x} \in \Sigma_S$ if, and only if, $\mathcal{N}(\mathbf{A})$ contains no vectors in Σ_{2S} [4]:

$$\mathcal{N}(\mathbf{A}) \cap \Sigma_{2S} = \emptyset \tag{1.12}$$

where $\emptyset$ denotes the null space. In other words, this necessary and sufficient condition, can be seen as a condition on every 2S-columns submatrix of $\mathbf{A}$ which must form a linearly independent set [5].

Moreover, when dealing with approximately sparse vectors, a more restrictive condition must be considered on the null space of the measurement matrix. Given a set of indices $\Sigma = \{1, 2, ..., n\}$, denoting with $\Theta \subset \Sigma$ a subset of indices, with $\Theta^c \subset \Sigma$ the complementary subset of Θ, and $\mathbf{h}_\Theta$ a vector in which the entries corresponding to the subset of indices Θ^c are sets to zero, it is possible to define the null space property [3].

Definition 1.3.1. A matrix $\mathbf{A}$ satisfies the null space property (NSP) of order S if there exists a constant $C_{NSP} > 0$ such that

$$\|\mathbf{h}_\Theta\|_2 \leq C_{NSP} \frac{\|\mathbf{h}_{\Theta^c}\|_1}{\sqrt{S}} \tag{1.13}$$

holds for all $\mathbf{h} \in \mathcal{N}(\mathbf{A})$ and for all Θ such that $|\Theta| \leq S$.

In [6], the NSP property is directly related to the robustness to non-sparse signals of a generic recovery algorithm, via the following theorem. Moreover, in [7] it is reported that is not necessary requiring (1.13) to hold for all Θ of size S, but it is sufficient that it is satisfied for the Θ corresponding to the largest magnitude entries of $\mathbf{h}$. Consequently, by denoting the new subsets with Θ' and $\Theta^{c'}$, it follows that $\|\mathbf{h}_{\Theta'}\|_2 \leq \|\mathbf{h}_\Theta\|_2$ and $\|\mathbf{h}_{\Theta^c}\|_1 \leq \|\mathbf{h}_{\Theta^{c'}}\|_1$.

Theorem 1.1. *Let* **A** *denote a measurement matrix,* $\Delta : \mathbb{R}^m \to \mathbb{R}^n$ *denote a recovery method, if the pair* (Δ, A) *satisfies*

$$\|\Delta(\mathbf{Au}) - \mathbf{u}\|_2 \leq C_{NSP} \frac{\sigma_S(\mathbf{u})_1}{\sqrt{S}} \tag{1.14}$$

A *satisfies the NSP of order* $2S$.

If verified, eq. (1.14) guarantees the exact recovery of all possible S-sparse signals, and not only for a small subsets of possible vectors, thus it is also referred to with the name "instance-optimal" or "uniform" guarantee. In particular, it has to be noticed the NSP is both necessary and sufficient for establishing guarantees of this form.

The ability of distinguish between two different solutions, originated by two different set of measurements can be also validated via the spark of the measurement matrix.

1.3.1 Spark

Definition 1.3.2. The spark of a matrix **A** is the smallest possible number such that exist a subgroup of σ columns that are linearly dependent [8].

$$\sigma = spark(\mathbf{A}) = \min_{\mathbf{u} \neq 0} \|\mathbf{u}\|_0 \quad s.t. \quad \mathbf{Au} = \mathbf{0} \tag{1.15}$$

Given this definition of spark, it is interesting to observe the differences between spark and rank of a matrix. The evaluation of the rank of a matrix is a sequential process which requires n steps, while the evaluation of the spark requires a combinatorial process of complexity 2^n steps [8].

If **A** has no zero columns, the corresponding spark is equal to two if, and only if, two columns of **A** are linearly dependent, otherwise σ will be greater than 2. More in general, the spark of a matrix is bounded in the range: $\sigma \in [2, m+1]$, where the upper bound is often referred to as the "Singleton Bound" [9]. In this regard, it is important to underline that:

$$\sigma = m + 1 \implies rank(\mathbf{A}) = m \tag{1.16}$$

but, in general, the vice-versa does not hold. For example, let consider the following measurement matrices:

$$\mathbf{A_{ex1}} = \begin{bmatrix} 1 & 1 & 0 & 0 \\ 1 & 0 & 1 & 0 \\ 1 & 0 & 0 & 1 \end{bmatrix} \quad \mathbf{A_{ex2}} = \begin{bmatrix} 1 & 1 & 1 & 0 & 0 \\ 1 & 1 & 0 & 1 & 0 \\ 1 & 1 & 0 & 0 & 1 \end{bmatrix} \tag{1.17}$$

where even if $rank(\mathbf{A_{ex1}}) = rank(\mathbf{A_{ex2}}) = 3$, based on Definition 1.3.2, it is

possible to affirm that:

$$\begin{aligned} \sigma_{\mathbf{A_{ex1}}} &= 4 \\ \sigma_{\mathbf{A_{ex2}}} &= 2 \end{aligned} \tag{1.18}$$

Theorem 1.2. *If a vector* $\mathbf{y}$ *has two different representations* $\mathbf{y} = \mathbf{Au}_1 = \mathbf{Au}_2$, *the two representations must have no less than* $spark(\mathbf{A})$ *non-zero entries combined [8].*

Consequently, the solution $\mathbf{u}$ of a system of linear equations $\mathbf{y} = \mathbf{Au}$ is necessarily the sparsest possible if:

$$\|\mathbf{u}\|_0 < \frac{spark(\mathbf{A})}{2} \tag{1.19}$$

Under this sufficient and necessary condition, the uniqueness of the sparse solution is guaranteed otherwise, there will be two different solutions for the same observation [9].

It is obvious that, in order to be able to recover the S-sparse component of a vector, the number of measurements, m, must be equal or larger than the sparsity level of the system. But, through the combination of (1.19) with the upper bound of the spark, it is possible to obtain a more strict, requirement:

$$m \geq 2S \tag{1.20}$$

It has to be noticed that the condition $m \geq 2S$ does not necessarily enforce $\sigma > 2S$, since there could exists an $m \times 2S$ matrix whose spark is smaller than $2S$ [9].

1.3.2 Mutual Coherence

Since computing the spark of a matrix is NP-hard, it is necessary to find easier methods to guarantee the uniqueness of the solution such as the mutual-coherence [3], which characterize the columns dependency of a matrix.

Definition 1.3.3. Given a matrix $\mathbf{A}$, the mutual-coherence is the largest absolute inner product between any two columns of $\mathbf{A} = [\mathbf{a}_1, \mathbf{a}_2, ..., \mathbf{a}_i, ..., \mathbf{a}_n]$ [4]:

$$\mu(\mathbf{A}) = \max_{\substack{i,j \in \{1,...,n\} \\ i \neq j}} \frac{|\langle \mathbf{a}_i, \mathbf{a}_j \rangle|}{\|\mathbf{a}_i\|_2 \|\mathbf{a}_j\|_2} \tag{1.21}$$

It has to be notice that the coherence is limited, in fact $\mu \in \left[\sqrt{\frac{n-m}{m(n-1)}}, 1\right]$, where the lower bound is often called "Welch bound". Moreover, when the matrix $\mathbf{A}$ has very few rows with respect to the number of columns, $n \gg m$, the lower bound is approximately $\mu(\mathbf{A}) \geq 1/\sqrt{m}$ [4].

In [4] the coherence of a matrix $\mathbf{A}$ is related to its spark by applying the Geršgorin circle theorem [10] to the Gram matrix $\mathbf{G} = \mathbf{A}_\Lambda^T \mathbf{A}_\Lambda$, where $\mathbf{A}_\Lambda$ denotes the matrix $\mathbf{A}$ in which each column has been normalized, in order to have unit ℓ_2 norm. The corresponding relation allows to easily determine the lower bound of $spark(\mathbf{A})$:

$$spark(\mathbf{A}) \geq 1 + \frac{1}{\mu(\mathbf{A})} \tag{1.22}$$

Moreover, by combining (1.22) and (1.19) it is possible to define a new condition which relates the sparsity of the system to the coherence of the measurement matrix.

Theorem 1.3. *The solution of the linear system* $\mathbf{y} = \mathbf{A}\mathbf{u}$ *is necessarily the sparsest possible if it obeys:*

$$S < \frac{1}{2}\left(1 + \frac{1}{\mu(\mathbf{A})}\right) \tag{1.23}$$

It has to be notice that the condition given by Theorem 1.3 is weaker than (1.19), due to its definition based on the coherence. In fact, while the upper limit of the spark is $m + 1$, the coherence cannot be lower than $\frac{1}{\sqrt{m}}$, thus the upper bound is fixed to $\frac{m+1}{2}$ for (1.19), and $\frac{1+\sqrt{m}}{2}$ for (1.23) [11].

1.4 Restricted Isometry Property

Till now, only the trivial scenario in which the measurements are not affected by errors has been considered. In a realistic scenario, when dealing with measurements affected by errors, more strong conditions must be considered such as the Restricted Isometry Property (RIP) [4], firstly introduced in [12].

Definition 1.4.1. A matrix $\mathbf{A}$ satisfies the RIP property of order S if there exist a constant, $\delta_S \in (0,1)$, such that:

$$(1 - \delta_S)\|\mathbf{x}\|_2^2 \leq \|\mathbf{A}\mathbf{x}\|_2^2 \leq (1 + \delta_S)\|\mathbf{x}\|_2^2 \tag{1.24}$$

for any $\mathbf{x}$ such that $\|\mathbf{x}\|_0 \leq S$ [13].

Even if in this formulation, the bounds are limited to 1, the same definition can be easily extended to arbitrary bounds until there is a scale of $\mathbf{A}$ which satisfies the RIP [4].

By considering eq.(1.24), it is possible to affirm that the RIP property ensure a certain robustness to the measurement noise. For example, when the measurement matrix $\mathbf{A}$ satisfies the RIP of order 2S, it is possible to affirm that

it preserves the distance between any pair of S-sparse vectors [4], and it ensure the correct reconstruction of the S non-zero components.

With a different prospective, the RIP also states that all sets of S-columns taken from $\mathbf{A}$ are nearly orthogonal, which implies that S sparse vectors cannot be in the null space of $\mathbf{A}$ [13].

Theorem 1.4. *Given a matrix $\mathbf{A}$ which satisfies the RIP of order S, with constant δ_S, for any $S' < S$ the same matrix satisfies the RIP of order S', with $\delta_{S'} \leq \delta_S$.*

Moreover, in [5] it has been reported that, given a positive integer γ, if $\mathbf{A}$ satisfies the RIP with constant δ_S, $\mathbf{A}$ also satisfies the RIP of order $S' = \gamma \lfloor \frac{S}{2} \rfloor$ with constant $\delta_{S'} < \gamma \delta_S$. This result, which might be trivial for $\gamma = 1, 2$, allows the extension of the RIP to orders higher than S, if $\gamma \geq 3$, $S \geq 4$, and δ_S sufficiently small [4]. For example: given a matrix $\mathbf{A}$ which satisfies the RIP of order $k = 4$, by setting $\gamma = 3$, the same matrix satisfies the RIP of order $S' = 3 \lfloor \frac{4}{2} \rfloor = 6$, with constant $\delta_{S'} < 3\delta_S$.

Theorem 1.5. *If a sensing matrix $\mathbf{A}$ satisfies the RIP of order $2S$ with $\delta_{2S} < \sqrt{2} - 1$, then $\mathbf{A}$ satisfies the NSP of order $2S$ with constant*

$$C_{NSP} = \frac{\sqrt{2}\delta_{2S}}{1 - (1 + \sqrt{2})\delta_{2S}} \tag{1.25}$$

Which leads to the conclusion that the RIP property is stronger than the NSP, since when the first is satisfied, also the second is satisfied [3].

The relation between the RIP and the measurements errors, together with the necessity of the RIP itself, can be also explained by considering the C-stability as reported in [14].

Definition 1.4.2. Let $\mathbf{A} : \mathbb{R}^n \to \mathbb{R}^m$ denote a measurement matrix and $\Delta : \mathbb{R}^m \to \mathbb{R}^n$ denote a recovery algorithm. The pair $(\mathbf{A}, \Delta)$ is C-stable if, for any $\mathbf{x} \in \Sigma_S$ and any measurement error vector $e \in \mathbb{R}^m$:t

$$\|\Delta(\mathbf{A}\mathbf{x} + \mathbf{e}) - \mathbf{x}\|_2 \leq C \|\mathbf{e}\|_2 \tag{1.26}$$

Definition 1.4.2 underlines that a small measurement noise does not largely impact the recovered signal. Thus, in order for the recovery algorithm to stably recover $\mathbf{x}$ from noisy measurements, the sensing matrix $\mathbf{A}$ must satisfy the lower bound of the RIP, with a constant determined by C [14].

Theorem 1.6. *If the pair $(\mathbf{A}, \Delta)$ is C-stable, then*

$$\frac{1}{C} \|\mathbf{x}\|_2 \leq \|\mathbf{A}\mathbf{x}\|_2 \tag{1.27}$$

for all $\mathbf{x} \in \Sigma_{2S}$.

When $C \to 1$, the measurement matrix must satisfy the lower bound of (1.24) with RIP constant $\delta_S = 1 - \frac{1}{C^2} \to 0$. Consequently, in order to reduce the impact of the measurement noise on the recovered signal, $\mathbf{A}$ must satisfy the same bound, with a tighter constant [14].

1.4.1 Measurement Bounds

Given any $m \times n$ measurement matrix, a general and sufficient condition on the minimum number of measurements for obtain a stable recovery, when the measurements are altered by errors, is

$$m \geq Slog^2 n \tag{1.28}$$

While more detailed results, for specific measurement matrices, are presented in [15] now, the minimum number of measurements m will be related to the RIP property.

Theorem 1.7. *Let $\mathbf{A}$ be a $m * n$ matrix that satisfied the RIP of order $S \leq \frac{n}{2}$ with constant $\delta_S \in (0, 1)$. Then*

$$m \geq C_\delta S \log\left(\frac{n}{S}\right) \tag{1.29}$$

where $C_\delta \approx \frac{0.18}{log\left(\sqrt{\frac{1+\delta_S}{1-\delta_S}}+1\right)} < 1$ is a constant depending only on δ_S [14].

Similar results can be obtained by considering the Gelfand width of the ℓ_1 ball [16], or through the Johnson-Lindenstrauss lemma [17,18]. Consequently, it is possible to affirm that, the recovery of an S-sparse vector requires a number of measurements in the order of $Slog\left(\frac{n}{S}\right)$.

1.4.2 Mutual Coherence

The evaluation of δ_S, and thus verifying the RIP property, is as complex as the evaluation of the spark, since it requires the sweep through all the $\binom{m}{S}$ supports [11]. As already proposed for the evaluation of the spark, also the RIP property can be related to the coherence of the measurement matrix $\mathbf{A}$ defined in sec. 1.3.2, through the application of the Geršgorin circle theorem [10].

Theorem 1.8. *A measurement matrix $\mathbf{A}$ with unit-norm columns, and coherence $\mu = \mu(\mathbf{A})$, satisfies the RIP of order S with [19]*

$$\delta_S \leq (S-1)\mu \tag{1.30}$$

1.5 Recovery of a sparse vector

Given a sparse system in the form

$$\mathbf{y} = \mathbf{Au} + \mathbf{e} \tag{1.31}$$

where $\mathbf{e} \in \mathbb{R}^m$ is a vector representing the band-limited measurement error, $\|\mathbf{e}\|_2 \leq \epsilon$, the sparse solution can be estimated by solving the following optimization problem

$$\widehat{\mathbf{u}} = arg \min_{\mathbf{u}} \|\mathbf{u}\|_0 \quad s.t. \quad \|\mathbf{y} - \mathbf{Au}\|_2 \leq \epsilon \tag{1.32}$$

Based on what has been reported in section 1.1, the problem (1.32) is non-convex, and thus is NP-hard to solve.

In [20], the RIP property has been used to show that both ℓ_0 and ℓ_1 norms are equivalent for the signal recovery.

$$\widehat{\mathbf{u}} = arg \min_{\mathbf{u}} \|\mathbf{u}\|_1 \quad s.t. \quad \|\mathbf{y} - \mathbf{Au}\|_2 \leq \epsilon \tag{1.33}$$

The use of the ℓ_1-norm makes problem (1.33) convex, reducing it into a linear program, whose polynomial complexity depends on the solver. This problem is also known as basis pursuit with denoise (BPDN), and it selects the entries of $\mathbf{u}$ with residual norm below the tollerance ϵ.

In [21], eq. (1.33) has been shown to recover a sparse signal with an error proportional to the noise level.

Theorem 1.9. *Let* $\mathbf{A}$ *satisfy the RIP of order* $4S$, *such that* $\delta_{3S} + 3\delta_{4S} < 2$. *Then, for any signal* $\mathbf{u}$ *with* $\|\mathbf{u}\|_0 \leq S$ *and any perturbation* $\epsilon \leq \|\mathbf{e}\|$, *the solution of* (1.33), $\hat{\mathbf{u}}$, *obeys*

$$\|\hat{\mathbf{u}} - \mathbf{u}\|_2 \leq \epsilon C_S \tag{1.34}$$

where C_S *is a constant, depending only on* δ_{4S}. *In particular,* C_S *is well behaved for reasonable values of* δ_{4S} ($C_S \approx 8,82$ *for* $\delta_{4S} = \frac{1}{5}$ *and* $C_S \approx 10,47$ *for* $\delta_{4S} = \frac{1}{4}$).

It has to be noticed that, if $\mathbf{A}$ verifies the condition in Theorem 1.9, the reconstruction from a noiseless measurement vector is exact, thus $\mathbf{A}\hat{\mathbf{u}} = \mathbf{y}$.

A more general condition for the stable recovery on approximately sparse vector, by minimizing the ℓ_1-norm only for the largest magnitude entries, is given by the following Theorem [22]:

Theorem 1.10. *Let* $\mathbf{A}$ *satisfy the RIP of order* $2S$ *with* $\delta_{2S} < \sqrt{2} - 1$. *The solution of 1.33 obeys*

$$\|\hat{\mathbf{u}} - \mathbf{u}\|_2 \leq \epsilon C_{1,S} + C_{0,S} \frac{\|\hat{\mathbf{u}} - \mathbf{u}\|_1}{\sqrt{S}} \tag{1.35}$$

where

$$C_{0,S} = 2 \frac{1 - \left(1 - \sqrt{2}\right) \delta_{2S}}{1 - \left(1 + \sqrt{2}\right) \delta_{2S}}, \quad C_{1,S} = 4 \frac{\sqrt{1 + \delta_{2S}}}{1 - \left(1 + \sqrt{2}\right) \delta_{2S}} \tag{1.36}$$

It has to be notice that Theorem 1.10 holds also for the case in which the vector to be reconstruct is properly sparse.

1.6 Sparse representation algorithms

The compressive sensing problem can be solved with different algorithms, each one with different characteristics and properties, which affects the speed, the ease of implementation and, in some cases, also the minimum number of measurements. According with [23] the sparse recovery approaches can be divided in three main categories: convex optimization problems, combinatorial algorithms, and greedy algorithms.

1.6.1 Convex optimization algorithms

The convex optimization problem in (1.33) can be also expressed as unconstrained problem, based on the Lagrange multiplier theorem.

$$\hat{\mathbf{u}} = arg \min_{\mathbf{u}} \frac{1}{2} \|\mathbf{y} - \mathbf{A}\mathbf{u}\|_2 + \lambda \|\mathbf{u}\|_1 \tag{1.37}$$

where λ refers to the Lagrange multiplier.

Typical solvers for these problems are interior-point methods [24], project gradient methods [25], iterative thresholding [26], and the basis pursuit [27]. These solvers are computationally more complex than other solutions, but they requires fewer measurements.

1.6.2 Combinatorial algorithms

Characterized by very high solving speed, they often require many measurements with a specific pattern, which are difficult to obtain. These techniques are based on the application of the group testing on many samples derived from the original signal. These algorithms are often characterized by binary and sparse measurement matrices, in order to be able to apply specific properties

for the sparse reconstruction [28, 29]. Heavy Hitters on Steroids (HHS) pursuit [30], and sub-linear Fourier transform [31] are typical examples of these algorithms.

1.6.3 Greedy algorithms - OMP and BOMP

Greedy algorithms are characterized by procedures that use, during each step, locally optimization criterion to solve the problem. With respect to the solutions presented above, they are a good compromise in terms of required number of measurements and computational burden. For this reason, in this thesis, this family of algorithms will be applied to the analysis of electrical distribution networks. In the CS case, greedy solvers allow to obtain approximate sparse representation, without directly solving the optimization problem.

For example, considering the problem (1.33), the greedy algorithm starts from an empty vector and builds the solution, $\hat{\mathbf{u}}$, by estimating a new non-zero entry during each step. The selection of the new entry is based on tests performed on each column of the sensing matrix $\mathbf{A}$, which aims to reduce the residual error in approximating the sparse vector $\mathbf{u}$. Between two consecutive iterations, the procedure also estimates the values of the chosen entries, by optimizing their values. Characterized by high solving speed, their performance guarantees are typically weaker than those of other methods [4].

The Orthogonal Matching Pursuit (OMP) algorithm is one of the most used algorithms to solve CS problems, due to its implementation simplicity and speed.

The algorithm, briefly summarized in Algorithm 1, after the initialization of the residuals to the measurement vector, and the definition of the sparsity level one wants to reach, proceed iteratively, estimating a new non-zero component during each iteration. While the number of iteration does not exceed the sparsity level, the algorithm looks for the column of the sensing matrix which is most correlated with the residuals, by considering the maximum energy inner product among them (step 1):

$$j^*(it) = arg \max_{j=1,..,n} |\langle \mathbf{a}_j, \mathbf{r}_{it-1} \rangle| \tag{1.38}$$

In fact, the inner product is commonly used as similarity measure [32]. The selected column is then attached to a temporary matrix, $\mathbf{A}^*$, which also stores the columns selected during the previous iterations (step 2). The selected columns, together with the measurements, are then used to evaluate the sparse solution, via a Least Square method (step 3). The estimated solution during this step will be characterized by a number of entries equal to the number of performed iterations, and the entries estimated during the previous iterations will be updated. During step 4, the residuals are updated and the iteration counter is

increased. Last, the estimated solution of (1.33) will be obtained by replacing the entries corresponding to the indices of the selected columns, $\mathbf{j}^*$, with the components estimated during the iterative process.

Algorithm 1 Orthogonal Matching Pursuit (OMP)

Input: $\mathbf{r}_0 = \mathbf{y}$, $\mathbf{A}^* = [\ \ ]$, $\mathbf{u}^* = [\ \ ]$, S, $it = 1$ **while** $it \leq S$ **do**

    1: $j^*(it) = arg \max\limits_{j=1,..,n} |\langle \mathbf{a}_j, \mathbf{r}_{it-1} \rangle|$

       $\mathbf{j}^* = [\mathbf{j}^*, j^*(it)]$

    2: $\mathbf{A}^* = [\mathbf{A}^*, \mathbf{a}_{j*(it)}]$

    3: $\widehat{\mathbf{u}}^* = arg \min \|\mathbf{y} - \mathbf{A}^* \mathbf{u}^*\|_2^2$

    4: $\mathbf{r}_{it} = \mathbf{y} - \mathbf{A}^* \widehat{\mathbf{u}}^*$

       $it = it + 1$

end

Output: $\widehat{\mathbf{u}}(\mathbf{j}^*) = \widehat{\mathbf{u}}^*$

Another implementation of this algorithm replaces the stopping criteria with a threshold on the residuals. In this case, the number of estimated non-zero entries is not fixed and it can be different than the expected one. Nevertheless, a threshold based on the residuals can be more suitable in cases in which the number of the expected non-zero entries is unknown. It has to be notice that, due to the continuous update of the estimations, the wrongly selected entries will be characterized by a low magnitude.

The key point of the OMP algorithm is that, contrarily to the "simplest" matching pursuit, it never re-select an entry which was chosen during a previous iteration, and the estimated residual is always orthogonal to all the selected items [4].

When considering noise-free measurements, the OMP was proved to recover the S-sparse unknown vector in exactly S iterations, for sensing matrices satisfying the RIP [33], and with bounded coherence only when the Exact Recovery Condition (ERC) is satisfied ($S < \frac{1}{2}\left(\frac{1}{\mu} + 1\right)$) [34]. Due to the required small constants to satisfy these conditions, this results apply when $m = O(S^2 log(n))$. In [35], was shown that having $m \approx (S log(n))$ for certain random matrices leads the OMP to selects the wrong elements, which results in a wrong estimation.

In [36], it was shown that the recovery of the sparse vector in presence of noise is possible. In particular, for the case of ℓ_2 bounded noise, it has been shown that the OMP can firstly select the significant components of the sparse vector, whereas while applying modified stopping criteria to Algorithm 1, such as a threshold based on the residuals, the OMP will recover all the non-zero components [37, 38].

Theorem 1.11. *Given a bounded noise vector, $\|e\|_2 < \epsilon$, and mutual coherence $\mu < \frac{1}{2S-1}$, the OMP algorithm with the stopping rule $\|\mathbf{r}_{it}\|_2 \leq \epsilon$ recovers exactly*

the true subset of correct variables, if

$$|u_{min}| \geq \frac{2\epsilon}{1 - (2S - 1)\mu} \tag{1.39}$$

where $|u_{min}|$ denotes the magnitude of the smallest non-zero coefficient of $\mathbf{u}$.

The main computational cost of OMP is given by the sensing matrix-vector inner products, which can became a problem when dealing with high dimension systems. Another problem when dealing with high dimension systems is given by the sparsity level, higher S requires high number of iterations and thus an increasing estimation time. To reduce the dependency on these factors, some variations of the OMP based on different coefficient updates (mainly Gradient Pursuit and Conjugate gradients) [39–42], and variations in the element selection [43–45], are proposed in literature but will not be considered in this thesis.

The only OMP variation considered in this thesis consists in the Block-OMP (BOMP), which is a modification of the algorithm presented above. The BOMP algorithm is of particular interest when dealing with block-sparse systems in the form:

$$\mathbf{y} = \mathbf{A}_b \mathbf{u}_b + \mathbf{e} \tag{1.40}$$

where the subscript b indicates the block representation of matrices and vectors, and

$$\mathbf{u}_b = [\underbrace{u_1, u_2, ..., u_d}_{\mathbf{u_{b1}}}, \underbrace{u_{d+1}, ..., u_{2 \times d}}_{\mathbf{u_{b2}}}, ..., \underbrace{u_{n-d+1}, ..., u_n}_{\mathbf{u_{b(n_b)}}}]^T \tag{1.41}$$

$$\mathbf{A}_b = [\overbrace{\mathbf{a}_1, \mathbf{a}_2, ..., \mathbf{a}_d}^{\mathbf{A_{b1}}}, \overbrace{\mathbf{a}_{d+1}, ..., \mathbf{a}_{2 \times d}}^{\mathbf{A_{b2}}}, ..., \overbrace{\mathbf{a}_{n-d+1}, ..., \mathbf{a}_n}^{\mathbf{A_{b(n_b)}}}] \tag{1.42}$$

Where $n_b = (n/d)$ is the number of blocks, and $\mathbf{u_{bi}}$ and $\mathbf{A_{bi}}$ denotes, respectively, the i-th d-size block-vector and block-matrix of $\mathbf{u}_b$ and $\mathbf{A}_b$. Consequently, it is possible to define the block sparsity S_b as the number of blocks in the state vector, $\mathbf{u}_b$, with entries different than zero.

Given the a system in the form (1.40), it is possible to define the block-coherence as [46]:

$$\mu_b = \max_{l, r \neq l} \frac{1}{d} \rho(\mathbf{M}[l, r]) = \max_{l, r \neq l} \frac{1}{d} \sqrt{\lambda_{max}(\mathbf{M}^H[l, r]\mathbf{M}[l, r])} \tag{1.43}$$

where $\mathbf{M}[l, r]$ is the (l, r)-th $d \times d$ block of the $n_b \times n$ matrix $\mathbf{M} = \mathbf{A}_b^H \mathbf{A}_b$ with $\mathbf{A}_b^H$ the conjugate transpose of $\mathbf{A}_b$. In general we have $0 \leq \mu_b \leq \mu$, but it is obvious that when considering $d = 1$ size blocks the block-coherence (1.43) and the coherence (1.21) are the same ($\mu_b = \mu$). Moreover, if the columns of the l-th block $\mathbf{A}_{bl}$ are orthonormal, for each l, the block-coherence is upper bounded by $\mu_b < 1/d$.

The steps of the BOMP algorithm, described in Algorithm 2, are almost

identical to the ones of the OMP, the main difference is in the columns selection. In fact, during each iteration, in step 1, the algorithm picks the d columns of the block $\mathbf{A}_{bj}$ corresponding to the higher ℓ_2-norm product between each block of the sensing matrix and the residual vector:

$$j^*(it) = arg \max_{j=1,n} \left\| \mathbf{r}_{it-1}^T \mathbf{A}_{bj} \right\|_2^2 \tag{1.44}$$

which is the natural extension of (1.38) for the evaluation of the similarities of matrix blocks. Consequently, during each iteration, the BOMP estimates d new non-zero entries.

Algorithm 2 Block Orthogonal Matching Pursuit (BOMP)

Input: $\mathbf{r}_0 = \mathbf{y}$, $\mathbf{A}_b^* = [\quad]$, $\mathbf{u}_b^* = [\quad]$, S_b, $it = 1$
while $it \leq S_b$ **do**

> 1: $j^*(it) = arg \max_{j=1,\ldots,n_b} \left\| \mathbf{r}_{it-1}^T \mathbf{A}_{bj} \right\|_2^2$
> $\mathbf{j}^* = [\mathbf{j}^*, j^*(it)]$
> 2: $\mathbf{A}_b^* = [\mathbf{A}_b^*, \mathbf{A}_{bj^*(it)}]$
> 3: $\widehat{\mathbf{u}}_b^* = arg \min \left\| \mathbf{y} - \mathbf{A}_b^* \mathbf{u}_b^* \right\|_2^2$
> 4: $\mathbf{r}_{it} = \mathbf{y} - \mathbf{A}_b^* \widehat{\mathbf{u}}_b^*$
> $it = it + 1$

end
Output: $\widehat{\mathbf{u}}_b(\mathbf{j}^*) = \widehat{\mathbf{u}}_b^*$

A sufficient condition for the perfect recovery in a noise-free scenario, applying the BOMP algorithm to a sensing matrix with orthonormal columns for each block, is that the block-coherence must satisfy [46] :

$$S_b d < \frac{1}{2} \left(d + \frac{1}{\mu_b} \right) \tag{1.45}$$

By comparing (1.45) with the sufficient conditions for $d = 1$, given in (1.23), it is possible to see that, since $\mu_b \leq \mu$, the use of block sparse vectors and matrices allows to guarantee recovery for potentially higher sparsity levels. This holds only for blocks with orthonormal columns, otherwise highly correlated dictionary blocks may cause noise amplifications, and the OMP solution can be preferable [47]. In [47] the condition for the guaranteed recovery is given for BOMP algorithm applied to cases in which the noise is bounded $\|e\|_2 < \epsilon$.

Theorem 1.12. *Given a bounded noise vector, $\|e\|_2 < \epsilon$, and mutual coherence $\mu < \frac{1}{2S-1}$, the BOMP algorithm identify all the non-zero entries of $\mathbf{u}_b$, if*

$$|u_{b,min}| > \frac{2\epsilon}{1 - (2S - 1)d\mu_b} \tag{1.46}$$

where $|u_{b,min}|$ denotes the magnitude of the smallest non-zero coefficient of $\mathbf{u}_b$. Then, the BOMP algorithm identifies all elements of $\mathbf{u}_b$, and its error is bounded

by

$$\|\widehat{\mathbf{u}}_b - \mathbf{u}_b\|_2^2 \leq \frac{\epsilon^2}{1 - (S_b - 1)d\mu_b} \tag{1.47}$$

which leads to the results presented in Theorem 1.11, for $d = 1$.

In the following chapters, the Compressive Sensing theory is applied on the analysis of different problems of real distribution systems. Depending on the operating conditions, the measurements available from the network are characterized by different uncertainty performance. These different uncertainty scenarios will be suitably taken into account by means of numerous Monte Carlo simulations, in the analysis of the performance of the proposed CS-based algorithms.

Chapter 2

Harmonic Source Estimation

2.1 State of the Art

Nowadays, the increasing diffusion of nonlinear loads in distribution networks is leading to an increasing harmonic pollution [48]. Harmonics are one of the main Power Quality (PQ) related phenomena, which involve serious consequences in the system. The higher usage of the power cables, the reduction of the lifetime of electric-supply devices, the increasing losses, and the higher costs of the electrical energy are only few of the harmonic consequences.

In order to limits these phenomena, and thus the related consequences, harmonic planning levels have been proposed, as in the technical report IEC/TR 61000-3-6 [49]. In particular, this report deals with distorting sources (loads and generators) connected to medium and higher voltage networks. Table 2.1 reports the compatibility levels indicated in [49], only with reference to low and medium voltage networks, expressed in percentage with reference to the fundamental component. These are reference values aimed at coordinating emission, and immunity, of the devices connected to the same system, in order to limit the impact on the operations of any component.

Table 2.1: Compatibility levels for individual harmonic voltages in low e medium voltage networks, from [49]

Odd harmonics non-multiple of 3		Odd harmonics multiple of 3		Even harmonics	
Harmonic order h	*Harmonic voltage [%]*	*Harmonic order h*	*Harmonic voltage [%]*	*Harmonic order h*	*Harmonic voltage [%]*
5	6	3	5	2	2
7	5	9	1.5	4	1
11	3.5	15	0.4	6	0.5
13	3	21	0.3	8	0.5
$17 \leq h \leq 49$	$2.27\frac{17}{h} - 0.27$	$21 \leq h \leq 45$	0.2	$10 \leq h \leq 50$	$0.25\frac{10}{h} + 0.25$

Since it is not feasible to control all the devices of the system, these limits are meant for a system-wide based analysis, and not for a detailed evaluation. Compatibility levels in table 2.1 are differentiated for each harmonic order, but the report also sets the level for the total harmonic distortion (THD), in particular THD = 8%.

Planning levels, as reported in table 2 of [49], are instead meant to be used as emission limits. These levels should be, for obvious reasons, equal o lower than the compatibility levels reported in table 2.1. The corresponding values, always differentiated for each harmonic order in percentage of the fundamental component, are reported here in table 2.2, while the indicative planning level for the total harmonic distortion is sets to 6.5%.

Table 2.2: Planning levels for individual harmonic voltages in medium voltage networks, from [49].

Odd harmonics non-multiple of 3		Odd harmonics multiple of 3		Even harmonics	
Harmonic order h	*Harmonic voltage [%]*	*Harmonic order h*	*Harmonic voltage [%]*	*Harmonic order h*	*Harmonic voltage [%]*
5	5	3	4	2	1.8
7	4	9	1.2	4	1
11	3	15	0.3	6	0.5
13	2.5	21	0.2	8	0.5
$17 \leq h \leq 49$	$1.9\frac{17}{h} - 0.2$	$0.2 \leq h \leq 45$	0.2	$10 \leq h \leq 50$	$0.25\frac{10}{h}+0.22$

Since the actual planning levels should be accurately chosen depending on the specific case study (type of the system, working scenario, and so on), the limits in table 2.2 can be used as an indication for determining emission limits.

Nevertheless, limits are not always respected, and specific analysis must be performed to inspect the causes of the overcome, the harmonic sources, in order to reduce their effects and, maybe, allocate the costs arising from the disturbances [50].

The detection of the harmonic sources in a system is not trivial, due to the spreading nature of the harmonics. In this regard, in literature, many solutions have been proposed [51–54], most of them based on the harmonic state estimation. These techniques, originally meant for transmission networks, are based on the more classic state estimation, and their goal, as it can be evinced by the name, consists in estimating the harmonic pollution level in every point of the system. It is worth underlining that the estimation of the harmonic state, as well as the state estimation, requires a lot of information, such as numerous measurements (these approaches are usually based on weighted least square solutions), and network topology and parameters.

In particular, harmonic measurements are collected with dedicated PQ-

meters, which can be characterized by high costs. Due to the high number of nodes in distribution networks, only few real PQ measurements are typically available, usually collected in the primary substations. Thus, it is not possible to directly monitor the harmonic state of the systems and alternative solutions must be taken into account.

The use of pseudo-measurements, such as historical and statistical information, is sometimes proposed, in addition to the real measurement, as an alternative solution to overcome this problem. Nevertheless, due to the high uncertainty related to this kind of information, the corresponding estimation is characterized by low accuracies, and is not always reliable.

A different approach can be based on the identification of the main harmonic sources, rather than estimating the entire state of the network. Such technique, proposed in [55] and [56], is known as Harmonic Source Estimation (HSE), and it is aimed at the identification of the sources (loads and/or generators), in order to act at the origin of the problem. The number of sources is clearly lower than the number of nodes of the network, and thus only fewer measurements are required with respect to the harmonic state estimation. Moreover, it is worth noting that a further distinction can be made, between highly polluting sources and poorly/not polluting sources. The first group is generally less populated than the second one, and this leads to the approximation of considering the system as sparse.

Based on these assumptions, a compressive sensing harmonics detector (CSHD) has been proposed in [57] and [58]. These solutions, by investigating respectively single and multiple harmonic orders simultaneously, allow to identify the harmonic sources in the system, and estimate the value of the polluting component (also defined forcing) using a realistic measurement system.

In the following sections, the modellization of the harmonic analysis is presented. Then, the compressive sensing-based approaches are explained and tested on a test distribution system.

2.2 Modellization

The measurement model related to the harmonic sources identification and estimation problem can be defined in the frequency domain. Starting from the approach for harmonic measurements proposed in the international standards [49, 59], and considering a steady-state phenomena, with measurements collected with a common time-tag, a general linear model of this problem can be defined with reference to the generic harmonic order h. The following linear system represents such model, where the over-bar denotes complex quantities,

which change depending on the harmonic order h:

$$\overline{\mathbf{y}}_h = \overline{\mathbf{A}}_h \overline{\mathbf{u}}_h + \overline{\mathbf{e}}_h \tag{2.1}$$

In (2.1), $\overline{\mathbf{y}}_h \in \mathbb{C}^m$ is the measurement vector, which includes m phasor measurements (voltage or current measured phasors at harmonic h), $\overline{\mathbf{u}}_h \in \mathbb{C}^n$ is a vector whose entries are the n unknown forcing terms (harmonic sources) of the hth harmonic (usually currents injected by nonlinear loads or generators), and $\overline{\mathbf{e}}_h \in \mathbb{C}^m$ represents the phasor measurement errors vector. The measurement matrix $\overline{\mathbf{A}}_h \in \mathbb{C}^{m \times n}$ links the measured harmonic phasors to the harmonic sources produced by the possible polluting loads or generators. This matrix represents the matrix frequency response of the network computed at frequency $h f_0$, where f_0 denotes the fundamental frequency of the system. Since the effects of the polluting sources can be recorded by the PQ instrumentation, and thus affects the measurements, the entries of $\overline{\mathbf{A}}_h$ can be computed starting from the impedances of lines and loads in the considered network, defining the measurement relationship.

The model in (2.1) can be also expressed in rectangular coordinates, and thus representing each phasor in terms of real and imaginary components. In particular, by considering the system in such form, it is possible to take into account the accuracies of the measurements. Thus, by denoting the real part of the phasors with the superscript r, and the corresponding imaginary component with x, the model of the system in rectangular coordinates can be written as follows:

$$\begin{bmatrix} \mathbf{y}_h^r \\ \mathbf{y}_h^x \end{bmatrix} = \begin{bmatrix} \mathbf{A}_h^r & -\mathbf{A}_h^x \\ \mathbf{A}_h^x & \mathbf{A}_h^r \end{bmatrix} \begin{bmatrix} \mathbf{u}_h^r \\ \mathbf{u}_h^x \end{bmatrix} + \begin{bmatrix} \mathbf{e}_h^r \\ \mathbf{e}_h^x \end{bmatrix} \tag{2.2}$$

$$\mathbf{y}_h^{rx} = \mathbf{A}_h^{rx} \mathbf{u}_h^{rx} + \mathbf{e}_h^{rx}$$

where, denoting the transpose operation with the superscript T, the vectors $\mathbf{y}_h^r = [\mathbf{y}_{h,1}^r, \ldots, \mathbf{y}_{h,m}^r]^T$ and $\mathbf{y}_h^x = [\mathbf{y}_{h,1}^x, \ldots, \mathbf{y}_{h,m}^x]^T$ represent, respectively, the real and the imaginary components of the phasors measurements in $\overline{\mathbf{y}}_h$. The same holds for vectors $\mathbf{u}_h^r$, $\mathbf{u}_h^x$, $\mathbf{e}_h^r$, and $\mathbf{e}_h^x$, and for the measurement matrix $\mathbf{A}_h^{rx}$.

Each phasor of $\overline{\mathbf{y}}_h$ is measured with a certain accuracy, and specific uncertainties can be defined for both magnitude and phase angle. This information can be reported in terms of standard uncertainty of the measurement, by considering the standard deviation associated to a certain level of confidence and a probabilistic distribution. In general, in absence of specific information, uniform distributions should be considered. In the following, both measurements and uncertainties are considered available in magnitude and phase angle. Given the i-th phasor, measured at the h-th harmonic, expressed in rectangular coordinates, $\bar{y}_{h,i} = y_{h,i}^r + j y_{h,i}^x$, the corresponding 2×2 covariance matrix is obtained

by uncertainty propagation law [60]. The following expression is used:

$$\mathbf{\Sigma}_{h,i}^{rx} = \begin{bmatrix} \cos\phi_{h,i} & -y_{h,i}\sin\phi_{h,i} \\ \sin\phi_{h,i} & y_{h,i}\cos\phi_{h,i} \end{bmatrix} \begin{bmatrix} \sigma_{y_{h,i}}^2 & 0 \\ 0 & \sigma_{\phi_{h,i}}^2 \end{bmatrix} \begin{bmatrix} \cos\phi_{h,i} & \sin\phi_{h,i} \\ -y_{h,i}\sin\phi_{h,i} & y_{h,i}\cos\phi_{h,i} \end{bmatrix}$$

(2.3)

where $y_{h,i} = |\bar{y}_{h,i}|$ and $\phi_{h,i}$ are the magnitude and phase angle of the i-th measured phasor.

In this thesis, all the measured phasors are considered independent (or, at least, uncorrelated), thus:

$$\mathbf{\Sigma}_{\mathbf{y}^{rx}} = \begin{bmatrix} \mathbf{\Sigma}_{h,1}^{rx} & & 0 \\ & \ddots & \\ 0 & & \mathbf{\Sigma}_{h,m}^{rx} \end{bmatrix}$$

(2.4)

Measurement processes of different measurements are assumed thus as independent. Correlation between measurements could arise due to several factors such as common synchronization sources, the temperature of the devices and so on. The analysis of these aspects is beyond the scope of this thesis, but they can be conceptually set into the same framework in a simple way.

Consequently, the model in eq.(2.2) can be modified, in order to take into account the measurement uncertainties, by weighting the measurements according to their uncertainties:

$$\mathbf{y}^{rx'} \triangleq \mathbf{U}^{-T}\mathbf{y}^{rx} = \mathbf{U}^{-T}\mathbf{A}_h^{rx}\mathbf{u}^{rx} + \mathbf{e}_w^{rx} = \mathbf{A}_h^{rx'}\mathbf{u}^{rx} + \mathbf{e}_w^{rx'}$$

(2.5)

where $\mathbf{e}_w^{rx'}$ is the result of the measurement errors whitening, and $\mathbf{U}$ is the upper triangular matrix obtained from the Cholesky factorization of $\mathbf{\Sigma}_{\mathbf{y}^{rx}}$, thus $\mathbf{\Sigma}_{\mathbf{y}^{rx}} = \mathbf{U}^T\mathbf{U}$.

2.2.1 Single harmonic based detector

In order to identify and estimate the harmonic sources, vector $\bar{\mathbf{u}}_h^{rx}$ must be recovered. This kind of estimation problem could be easily solved by applying classic solving techniques for linear systems, such as the Weighted Least Square (WLS). But, it has to be considered that the WLS can be applied only to determined or overdetermined systems ($m \geq n$), whereas estimation of the harmonic sources problem is typically an underdetermined problem, due to the lack of real measurements from the field. A possible solution to overcome this problem could be the inclusion of additional information into the model of the system under study. Pseudo-measurements, for example, could be considered, but the high uncertainties of such information could significantly decrease the performance of the estimation. Moreover, not all the harmonic sources in a distribution system pollute simultaneously, and thus the vector of the forcing terms, $\mathbf{u}_h^{rx}$, is sparse. According to these assumptions, the unknown non-zero

entries in vector $\mathbf{u}_h^{rx}$ of (2.2) can be recovered with a compressive sensing-based algorithm, such as the BOMP illustrated in Section 1.6.3. In fact, the BOMP algorithm allows to keep the correlation between magnitude and phase angle of each quantity, through the representation in rectangular coordinates, and the analysis of blocks with size $d = 2$.

As a first step, the block-sparsity level of the system must be defined, according to the number of harmonic sources to be investigated in the network. Then, after initializing the residual vector to the measurements, the measurement matrix $\mathbf{A}_h^{rx}$, or $\mathbf{A}_h^{rx'}$ when considering the whitening of the measurements, should be reorganized in blocks associated to the real and imaginary components of each load.

$$\mathbf{A}_h^{rx} \mathbf{G}^T \mathbf{G} \mathbf{u}_h^{rx} = \mathbf{A}_b^{rx} \mathbf{u}_b^{rx} \tag{2.6}$$

In the right-hand side of eq. (2.6), for sake of simplicity, the subscript h denoting the harmonic order under analysis has been omitted, and just the subscript b denoting the block-reordered matrices and vectors is reported. Matrix $\mathbf{G}$ in (2.6) is a orthonormal matrix, which allows reordering vector $\mathbf{u}_h^{rx}$ in order to have elements of the same block (real and imaginary components of the same source) contiguous.

Then, as known from the CS theory, the block-columns of matrix $\mathbf{A}_b^{rx}$ should be orthogonalized, for example with the Gram-Schmidt method, and then every column must be normalized with respect to the ℓ_2-norm. This step allows to avoid the amplifications/attenuations caused by the different scaling of voltage and current measurements. Consequently, the system (2.2) becomes:

$$\mathbf{y}_h^{rx} = \mathbf{A}_{bN}^{rx} \mathbf{u}_{bN}^{rx} + \mathbf{e}_h^{rx} \tag{2.7}$$

where the subscript N denotes the orthonormalized vectors and matrices.

Now, the iterative procedure of the BOMP can proceed as described in Algorithm 2. During each iteration, the algorithm looks for the 2-size columns block which is more related to the residuals, based on the analysis of the maximum energy inner products between the residuals and each columns block.

The columns block corresponding to the selected index is then concatenated with the temporary matrix, $\mathbf{A}_b^*$, containing the blocks selected during the previous iterations, if any. This matrix is then used to solve the following overdetermined problem:

$$\mathbf{y} = \mathbf{A}_b^* \widehat{\mathbf{u}}_{bN}^{rx} \tag{2.8}$$

where the estimated vector $\hat{\mathbf{u}}_{bN}^{rx}$ will have as many entries as the number of performed iterations. It is important to mention that the indices of the selected column blocks denote the location of each recovered entry in vector $\mathbf{u}_h^{rx}$. Then, the residuals are updated, and a new iteration can begin.

When the stopping criteria is verified, the iterative process ends, and the non-zero entries of the unknown vector $\mathbf{u}_h^{rx}$ are recovered from $\hat{\mathbf{u}}_{bN}^{rx}$, by inverting the orthonormalization and grouping procedures.

2.2.2 Multiple harmonics based detector

The procedure described above well applies to the analysis of a single harmonic order, but not all the harmonic sources are always polluting for the same harmonics. Each source is characterized by specific pollution levels for each harmonic order, which can also be zero in some cases. Moreover, a passive load with capacitors could act as harmonic "amplifier", making the identification of the actual sources even harder. Consequently, the problem is complex, and the approach has to be global. Based on the approach proposed in the previous section, not all the polluting sources could be detected, depending on the considered harmonic order. This approach can be suitable for specific analysis, but in a real application scenario, it is not feasible to know a priori which harmonic order should be investigated.

In this section, a global harmonic detector, based on the contemporary analysis of multiple harmonic orders as proposed in [58], for the identification of the most polluting sources in a system is presented.

Starting from the model in (2.2), since each source can be seen as a multiple harmonics polluter, the more general model of the system can be written in the form:

$$
\begin{bmatrix} \mathbf{y}_{h_1}^r \\ \mathbf{y}_{h_1}^x \\ \vdots \\ \mathbf{y}_{h_Q}^r \\ \mathbf{y}_{h_Q}^x \end{bmatrix} = \begin{bmatrix} \mathbf{A}_{h_1}^{rx} & & \\ & \ddots & \\ & & \mathbf{A}_{h_Q}^{rx} \end{bmatrix} \begin{bmatrix} \mathbf{u}_{h_1}^r \\ \mathbf{u}_{h_1}^x \\ \vdots \\ \mathbf{u}_{h_Q}^r \\ \mathbf{u}_{h_Q}^x \end{bmatrix} + \begin{bmatrix} \mathbf{e}_{h_1}^r \\ \mathbf{e}_{h_1}^x \\ \vdots \\ \mathbf{e}_{h_Q}^r \\ \mathbf{e}_{h_Q}^x \end{bmatrix}
$$
$$
\mathbf{y}^{rx} = \mathbf{A}^{rx}\mathbf{u}^{rx} + \mathbf{e}^{rx}
$$

(2.9)

where Q denotes the total number of harmonics considered. The model in (2.9) is obtained by applying the superposition principle to different harmonic orders. Consequently, due to the orthogonality of the harmonics, the global measurement matrix, $\mathbf{A}^{rx}$, is block diagonal, and the other vectors are obtained by simply concatenating, for each considered harmonic order, the vectors corresponding to single model analysis.

Thanks to this representation, each source can be inspected, contemporary, in a wide range of harmonics. The overall forcing vector, $\mathbf{u}^{rx}$, will have only few non-zero entries with respect to its size, allowing to better detect the main pol-

luting sources. In order to underline this, the forcing vector should be reordered, by grouping the harmonic forcing terms related to the same source.

$$
\begin{bmatrix} \mathbf{y}_{h_1}^{rx} \\ \vdots \\ \mathbf{y}_{h_Q}^{rx} \end{bmatrix} = \begin{bmatrix} \mathbf{A}_{h_1,1}^{rx} & & \\ & \ddots & \\ & & \mathbf{A}_{h_Q,1}^{rx} \end{bmatrix} \cdots \begin{bmatrix} \mathbf{A}_{h_1,n}^{rx} & & \\ & \ddots & \\ & & \mathbf{A}_{h_Q,n}^{rx} \end{bmatrix} \begin{bmatrix} u_{h_1,1}^{r} \\ u_{h_1,1}^{x} \\ \vdots \\ u_{h_Q,1}^{r} \\ u_{h_Q,1}^{x} \\ \vdots \\ \hline u_{h_1,n}^{r} \\ u_{h_1,n}^{x} \\ \vdots \\ u_{h_Q,n}^{r} \\ u_{h_Q,n}^{x} \end{bmatrix} + \mathbf{e}_b^{rx}
$$
(2.10)

$$
\mathbf{y}^{rx} = \mathbf{A}_b^{rx} \mathbf{u}_b^{rx} + \mathbf{e}_b^{rx}
$$

where $u_{h_k,l}^{r}$ and $u_{h_k,l}^{x}$, with $k = 1,\ldots,Q$ and $l = 1,\ldots,n$, respectively denote the real and imaginary components of the forcing quantity injected by the l-th source for the k-th harmonic. Each sub-matrix $\mathbf{A}_{h_k,l}^{rx} = [\mathbf{A}_{h_k,l}^{r} \mathbf{A}_{h_k,l}^{x}] \in \mathbb{R}^{2m \times 2m}$ is related to the measurement matrix of the l-th source, with reference to the k-th harmonic. In (2.10), each block represents a specific source: $\mathbf{u}_l^{rx} = [u_{h_1,l}^{r}, u_{h_1,l}^{x}, \ldots, u_{h_Q,l}^{r}, u_{h_Q,l}^{x}]^T$. Consequently, having a block sparsity $S_b = 2$ corresponds to a forcing vector with only two blocks $\mathbf{u}_l^{rx}$ with ℓ_0-norm different than zero. For example, having $S_b = 2$ in a system with 4 loads (n), and considering 3 harmonics (Q), could corresponds to a state vector in the form:

$$
\mathbf{u}_b^{rx} = \begin{bmatrix} \mathbf{u}_{l_1}^{rx} \\ \mathbf{u}_{l_2}^{rx} \\ \mathbf{u}_{l_3}^{rx} \\ \mathbf{u}_{l_4}^{rx} \end{bmatrix} = \begin{bmatrix} \mathbf{u}_{l_1}^{rx} \\ \mathbf{0} \\ \mathbf{u}_{l_3}^{rx} \\ \mathbf{0} \end{bmatrix} = \begin{bmatrix} \mathbf{u}_{h_1,l_1}^{rx} \\ \mathbf{u}_{h_2,l_1}^{rx} \\ \mathbf{u}_{h_3,l_1}^{rx} \\ \hline \mathbf{0} \\ \mathbf{0} \\ \mathbf{0} \\ \hline \mathbf{u}_{h_1,l_3}^{rx} \\ \mathbf{u}_{h_2,l_3}^{rx} \\ \mathbf{u}_{h_3,l_3}^{rx} \\ \hline \mathbf{0} \\ \mathbf{0} \\ \mathbf{0} \end{bmatrix} = \begin{bmatrix} \mathbf{0} \\ \mathbf{u}_{h_2,l_1}^{rx} \\ \mathbf{0} \\ \hline \mathbf{0} \\ \mathbf{0} \\ \mathbf{0} \\ \hline \mathbf{u}_{h_1,l_3}^{rx} \\ \mathbf{u}_{h_2,l_3}^{rx} \\ \mathbf{u}_{h_3,l_3}^{rx} \\ \hline \mathbf{0} \\ \mathbf{0} \\ \mathbf{0} \end{bmatrix}
$$
(2.11)

where the load l_1 has a forcing component only in correspondence of the h_2

harmonic, while the load l_3 has forcing components in correspondence of all the harmonics under analysis (h_1, h_2, and h_3).

With reference to the measurement uncertainties, same consideration of Sec. 2.2.1 holds, the relation in eq.(2.3) is still valid for each measured phasor and eq.(2.4) can be extended to a more generic representation, in order to consider multiple measurements with reference to different harmonics, then:

$$
\boldsymbol{\Sigma}_{\mathbf{y}^{rx}} =
\begin{bmatrix}
\boldsymbol{\Sigma}_{h_1,1}^{rx} & & & & & & 0 \\
& \ddots & & & & & \\
& & \boldsymbol{\Sigma}_{h_1,m}^{rx} & & & & \\
& & & \ddots & & & \\
& & & & \boldsymbol{\Sigma}_{h_Q,1}^{rx} & & \\
& & & & & \ddots & \\
0 & & & & & & \boldsymbol{\Sigma}_{h_Q,m}^{rx}
\end{bmatrix}
\tag{2.12}
$$

where $\boldsymbol{\Sigma}_{h_k,v}^{rx}$ denotes the covariance matrix related to the v-th measured phasor ($v = 1,\ldots,m$) referred to the k-th harmonic. The matrix in (2.12) can be than used to weight the different measurements as seen in the previous section.

Also in this case, the BOMP algorithm is suitable to recover the sparse vector $\mathbf{u}_b^{rx}$, by considering blocks of size $d = 2Q$. The procedure is an extension of the one described in the previous section, and is composed by the following stages:

1. Orthonormalization of the measurement matrix, inside each columns block, through the right-moltiplication by the ortonormalization matrix $\mathbf{D}$:

$$
\mathbf{y}_h^{rx} = \mathbf{A}_b^{rx} \mathbf{D} \mathbf{D}^{-1} \mathbf{u}_b^{rx} + \mathbf{e}^{rx} = \mathbf{A}_N^{rx} \mathbf{u}_N^{rx} + \mathbf{e}^{rx}
\tag{2.13}
$$

where $\mathbf{D}$ is the block-diagonal matrix including the orthogonalization basis for all the blocks in $\mathbf{A}_b^{rx}$. With reference to the generic load l, and its corresponding sub-matrix $\mathbf{A}_{b,l}^{rx} = [\mathbf{a}_{b\,h_1,l}^r, \mathbf{a}_{b\,h_1,l}^x, \ldots, \mathbf{a}_{b\,h_Q,l}^r, \mathbf{a}_{b\,h_Q,l}^x]$, the l-th block of matrix $\mathbf{D}$ is block-diagonal, due to the orthogonality of the harmonics, and it can be written as:

$$
\mathbf{D}_l =
\begin{bmatrix}
\begin{bmatrix}
\frac{1}{\left\|\mathbf{a}_{b\,h_1,l}^r\right\|_2} & -\frac{\mathbf{a}_{b\,h_1,l}^r \cdot \mathbf{a}_{b\,h_1,l}^x}{\left\|\mathbf{a}_{b\,h_1,l}^r\right\|_2^2 \left\|\mathbf{b}_{h_1,l}\right\|_2} \\
0 & \frac{1}{\left\|\mathbf{b}_{h_1,l}\right\|_2}
\end{bmatrix} & & 0 \\
& \ddots & \\
0 & & \begin{bmatrix}
\frac{1}{\left\|\mathbf{a}_{b\,h_Q,l}^r\right\|_2} & -\frac{\mathbf{a}_{b\,h_Q,l}^r \cdot \mathbf{a}_{b\,h_Q,l}^x}{\left\|\mathbf{a}_{b\,h_Q,l}^r\right\|_2^2 \left\|\mathbf{b}_{h_Q,l}\right\|_2} \\
0 & \frac{1}{\left\|\mathbf{b}_{h_Q,l}\right\|_2}
\end{bmatrix}
\end{bmatrix}
\tag{2.14}
$$

where $\|\mathbf{b}_{h_k,l}\|_2 = \sqrt{\left\|\mathbf{a}^x_{b\,h_k,l}\right\|_2^2 - \frac{\langle\mathbf{a}^r_{b\,h_k,l},\mathbf{a}^x_{b\,h_k,l}\rangle^2}{\left\|\mathbf{a}^r_{b\,h_k,l}\right\|_2^2}}$ with reference to the generic h_k-th harmonic order.

2. BOMP algorithm, which begins with the initialization of the residuals $(\mathbf{r}_0 = \mathbf{y}^{rx}_h)$ and the definition of the block-sparsity, to iteratively search for the columns-block most correlated to the residuals. During each iteration, $2Q$ columns are selected from the measurement matrix $\mathbf{A}^{rx}_N$, by considering:

$$j(it) = arg \max_{l=1,\ldots,n} \left\|\mathbf{r}^T_{it-1}\mathbf{A}^{rx}_{N\,l}\right\|_2^2 \qquad (2.15)$$

where the subscript it denotes the number of iteration, and $\mathbf{A}^{rx}_{N\,l} = [\mathbf{a}^r_{N\,h_1,l},$ $,\mathbf{a}^x_{N\,h_1,l},\ldots,\mathbf{a}^r_{N\,h_Q,l},\mathbf{a}^x_{N\,h_Q,l}]$. The index $j(it)$ denotes the source corresponding to the higher energy product and the corresponding columns are attached to the temporary matrix which stores the columns of the selected sources:

$$\mathbf{A}^*_N = [\mathbf{A}^*_N,\ \mathbf{A}^{rx}_{N\,j(it)}] \qquad (2.16)$$

This matrix has size $(m \times Q)$-by-$(2Q \times it)$ and it represents the measurement matrix of the overdetermined system $\mathbf{y}^{rx} = \mathbf{A}^*_N\mathbf{u}^{rx\,*}_N$:

$$\widehat{\mathbf{u}}^{rx\,*}_N = (\mathbf{A}^{*T}_N\mathbf{A}^*_N)^{-1}\mathbf{A}^{*T}_N\mathbf{y}^{rx} = \mathbf{A}^{*\dagger}_N\mathbf{y}^{rx} \qquad (2.17)$$

where the use of the pseudo-inverse $(\mathbf{A}^{*\dagger}_N = (\mathbf{A}^{*T}_N\mathbf{A}^*_N)^{-1}\mathbf{A}^{*T}_N)$ is required for the LS estimation of the sources at each iteration. During this step, not only Q new entries are estimated, but the ones estimated in the previous iterations, if any, are updated. Then, the residuals are updated, and a new iteration can begins, if the number of performed iterations does not overcomes the block-sparsity limit.

3. After quitting the iterative process, the number of entries in the recovered vector $\widehat{\mathbf{u}}^{rx\,*}_N$, and thus its size, depends on the number of iterations and it is equal to $2Q \times it = 2Q \times S_b$. Its entries must be placed in the unknown forcing vector according to the block indices selected during the iterative procedure, and thus

$$\widehat{\mathbf{u}}^{rx}_{N,j} = \widehat{\mathbf{u}}^{rx\,*}_N \qquad (2.18)$$

while the other entries are zeros. Then, in order to obtain the effective recovery of the forcing terms, it is necessary to de-orthonormalize $\widehat{\mathbf{u}}^{rx}_{N,j}$, by simply pre-multiplying it by the orthonormalization matrix:

$$\widehat{\mathbf{u}}^{rx} = \mathbf{D}\widehat{\mathbf{u}}^{rx}_{N,j} \qquad (2.19)$$

In the following, we will refer to this algorithm as Load BOMP (LBOMP), due to its peculiarity of considering each load as a block, consisting by a forcing

for each considered harmonic. It is worth mentioning that, when considering only a single harmonic order ($k = h$), the procedure described above reduces to the one described in Section 2.2.1.

2.2.3 Measurement uncertainties

The standard IEC 61000-4-7 [59] defines the measurement accuracy requirements with reference to two class of instruments: Class I and Class II. Class I instruments are recommended for applications in which a high accuracy is required, such as standard compliance and emission measurements, whereas Class II instruments are more suitable for general purpose. According to this definitions, Class I instruments are more appropriate for the aim of this Section, the detection of harmonic polluting sources, and thus Class I instrument will be considered.

In [59], the uncertainties for Class I instruments, here reported in table 2.3, are expressed with reference to the ratio between the measured magnitudes of voltage and current, respectively U_m and I_m, and the nominal voltage and current, U_n and I_n, of the measurement device.

Table 2.3: Accuracy Requirements for Voltage and Current Measurements [59]

Class	Measurements	Conditions	Max Error
I	Voltage	$U_m \geq 1\%U_n$	$\pm 5\%U_m$
		$U_m < 1\%U_n$	$\pm 0.05\%U_n$
	Current	$I_m \geq 3\%I_n$	$\pm 5\%I_m$
		$I_m < 3\%I_n$	$\pm 0.15\%I_n$

As it can be seen from table 2.3, the standard [59] does not take into account the phase angle uncertainties. In this thesis, the measurement accuracy of the phase angles is considered, for all the tests and without loss of generality, equal to 1 crad with reference to the fundamental, and it is assumed to increase proportionally with the harmonic level for the harmonic phase angle measurements. Moreover, based on previous research activities on the accuracy of the measurement provided by instrument transformers under distorted conditions [61], the measurement uncertainty on the magnitudes of the harmonics is considered ten times larger than the one at the fundamental frequency.

2.3 Test and Results

The proposed methodologies are here tested and compared, in order to underline their differences. In the following, the single harmonic analysis method, presented in Section 2.2.1, will be named "BOMP", whereas the multiple harmonic

technique, presented in Section 2.2.2, will be labelled as "LBOMP". Moreover, the performance of these two techniques will be compared with the performance of a classic WLS technique. In this regard, it has to be noticed that the WLS technique is based on finding the minimum ℓ_2-norm solution, and thus it does not recover a sparse vector, it estimates a possible value for all the components of the vector which should be recovered.

Tests will be performed on a small distribution network, which is derived from the IEEE 13 bus distribution feeder [62], shown in figure 2.1.
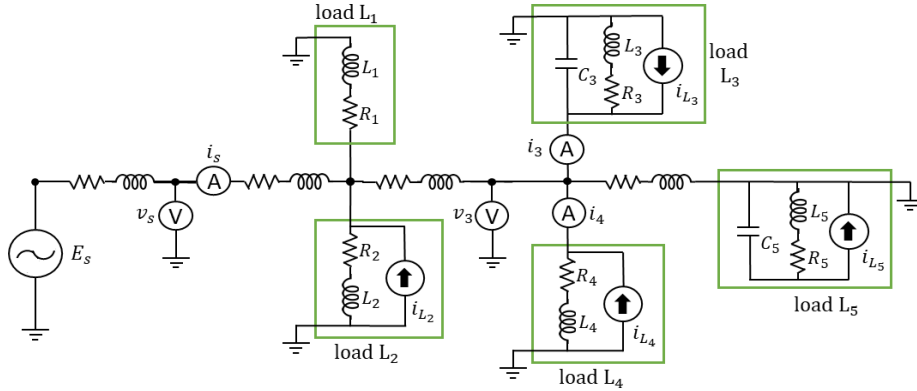
Figure 2.1: Test grid.

The nominal rms value of the voltage source is $E_s = 2.4$ kV, at the rated frequency of $f_n = 60$ Hz, while the nominal active powers and currents of each one of the 5 loads are reported in table 2.4.

Table 2.4: Nominal Loads Configuration

Load	P_n [kW]	I_n [A]
L1	1333.33	55.51
L2	80.15	39.00
L3	73.90	34.46
L4	345.33	180.47
L5	140.72	65.07

Loads L2, L3, L4 and L5 are considered as possible polluting sources, whereas the substation and load L1 are considered linear and not polluting. The non-linearity are represented through an ideal current source, connected in parallel to the ohmic-inductive impedance (representing the linear load). The forcing current of the l-th load is obtained by summing up all the harmonics components

considered in the signal:

$$i_l(t) = \sum_{k=1}^{Q} i_{h_k,l}(t)$$

$$i_{h_k,l}(t) = \sqrt{2}I_{h_k,l}\sin(2\pi h_k f_0 + \phi_{h_k,l})$$

(2.20)

where $I_{h_k,l}$ represents the rms value of the forcing current injected by the l-th load with reference to the h_k-th harmonic order, and $\phi_{h_k,l}$ is the corresponding phase angle. In this thesis, only the first four odd harmonics are considered, thus $h = [3, 5, 7, 9]$ and $Q = 4$. Reference values of magnitude and phase angle, for each load (with exception of load L1, supposed fully linear) and each harmonic order, are reported in table 2.5; where I_{h_k} is expressed in percentage with respect to the current rated at the fundamental frequency (I_n in table 3.4), and ϕ_{h_k} is expressed in radiants.

Table 2.5: Harmonic Load Configuration

Harmonic order h_k	Load L2		Load L3		Load L4		Load L5	
	I_{h_k} [%]	ϕ_{h_k} [rad]	I_{h_k} [%]	ϕ_{h_k} [rad]	I_{h_k} [%]	ϕ_{h_k} [rad]	I_{h_k} [%]	ϕ_{h_k} [rad]
3	10.2	-0.48	19.3	-0.37	7.5	-1.53	21.1	-0.35
5	2.1	0.89	3.8	1.12	3.7	-0.33	4.1	1.16
7	1.6	2.58	3	2.59	0.7	2.40	3.2	2.59
9	1.0	-1.67	1.9	-1.67	0.5	-1.69	2.1	-1.67

During the tests, these values, with reference to each load and each harmonic level, will be enabled/disabled in order to simulated different scenarios. According to this, the results here presented are based on the following test cases:

- Case 1, forcing loads L3 and L4, for all the considered harmonic orders;

- Case 2, forcing loads L4 and L5, for all the considered harmonic orders;

- Case 3, forcing loads L3 and L4, for all the considered harmonic orders, with the exception of L3 non-polluting for the 5-th harmonic;

- Case 4, all loads forcing at 10% of the values in table 2.5, whereas the forcing of loads L3 and L4 are set to 100%, for all the considered harmonic orders.

As shown in figure 2.1, only two multi-channels measurements devices are considered. It should be noticed that no particular placement techniques have been applied, but these locations can be considered as typical: one measurement nearby the substation, and one in a point of common coupling. The accuracy

of the measurements provided by these devices have been taken into account by means of 10000 Monte Carlo (MC) simulations. During each MC trial, the measurement error has been considered by extracting the additive terms from uniform distributions. The limits of the distributions are defined according to the standard [59], as described in Section 2.2.3. These accuracies are here considered as representative of the overall uncertainty of the measurement chain, thus including also the transducers.

As a fair comparison, an algorithm based on a WLS minimization is considered. This algorithm, in the following called WLS for the sake of brevity, computes the minimum Mahalanobis distance solution of the single harmonic model (equation (2.5)), with respect to $\boldsymbol{\Sigma}_{\mathbf{y}^{rx}}$. In the following, the results of the comparison between the proposed methodologies (BOMP, LBOMP) and WLS, are presented in terms of percentage of detection of each polluting source, and in terms of accuracy of the estimation of the pollution injected by the source. In particular, since the main goal is to identify the main polluting sources, the detection criteria is based on the application of a post-detection threshold. The use of the threshold allows to neglect the sources characterized by a small injection, and thus not significantly polluting, and to prevent false detections.

The post-detection threshold will be applied, for each harmonic order h_k and each load l, to the estimated forcing terms in $\widehat{\mathbf{u}}^{rx}$:

$$v_{h_k,l} = \left(\sqrt{\hat{u}_{h_k,l}^{r2} + \hat{u}_{h_k,l}^{x2}} \geq t_{h_k} \right) = \begin{cases} \text{true} \Rightarrow \text{polluting} \\ \text{false} \Rightarrow \text{non-polluting} \end{cases} \qquad (2.21)$$

where $\hat{u}_{h_k,l}^{r}$ and $\hat{u}_{h_k,l}^{x}$ are the real and the imaginary component of the estimated source, while t_{h_k} is the post-detection threshold referred to the h_k harmonic. The threshold, for example, could be adjusted by the operator which is inspecting the network, depending on different criteria such as network characteristics, type of sources and so on. The variable $v_{h_k,l}$, is binary and it can be equal to 1 only when the inequality is verified, thus the corresponding load should be labelled as polluter, whereas is 0 otherwise. It is worth noticing that, since the thresholds are applied to all the considered harmonics, in the global approach, LBOMP, proposed in Section 2.2.2, each load will be considered as polluting if the relation in eq.(2.21) is verified for at least one harmonic order.

In order to set reasonable threshold limits, the information available in the technical report IEC/TR 61000-3-6 [49] is considered, and reported in table 2.6. The limits in table 2.6 are expressed in percentage with reference to the fundamental component. It has to be noticed that, since [49] does not include limits for all the harmonics here considered, based on reasonableness criteria, the limits for the 3-rd and the 9-th harmonic currents are assumed, respectively,

equal to 5% and 3%.

Table 2.6: Harmonic current emission limits from [49], extended with 3rd and 9th harmonics

	Harmonic order h						
	3	*5*	*7*	*9*	*11*	*13*	*>13*
Emission Limits [%]	5	5	5	3	3	3	$500/h^2$

In the following, the identification results will be presented as functions of the thresholds which will vary starting from 0% (which means that no post-detection threshold is applied). The limits proposed in table 2.6 will be labelled with "STD", whereas the reference polluting value of the source, representing the actual current injected by the source, will be labelled as "REF". According to this, the ideal detection function can be represented as a step function, which should be equal to 100% for every threshold value lower than "REF", and which will immediately decrease to 0% after it. It follows that, the detection function corresponding to non-polluting sources should be always constant, and equal to zero.

In figure 2.2, the detection functions are reported for Case 1, with reference to the 3rd harmonic order, for the loads L3, L4 and L5. The proposed solutions are reported with different lines: the single harmonic based technique, BOMP, is represented with a blue line and circled markers, and the global approach, LBOMP, with yellow line and star marker, while the WLS method is represented with red line and diamond markers.
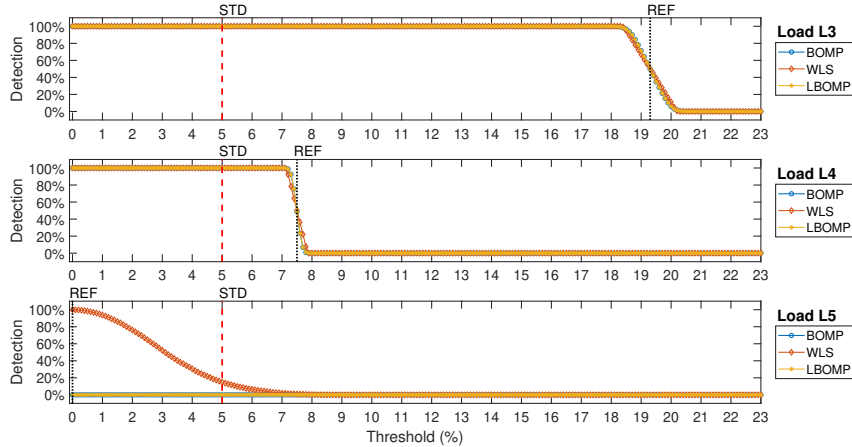

Figure 2.2: Harmonic detection - Case 1: forcing loads L3 and L4, harmonic order under analysis $h = 3$.

Load L3 is correctly detected as polluting (100%) by all the methodologies, until the post-detection threshold is set equal to the reference value of the forc-

ing. Same considerations hold also for load L4, where the detection function is more step-like in correspondence of a threshold level equal to REF, as should be in the ideal scenario. Load L5 instead, is correctly detected as not-polluting by both BOMP and LBOMP, whereas is labelled as polluting for the WLS. The erroneous detection provided by the WLS depends on the methodology itself, since it tries to estimate every possible entry in the state vector, and the detection rate becomes equal to 100% when the threshold is set to 0%, while it decreases with the increment of the post-detection threshold, until 9% of the nominal current, when also the WLS indicating load L5 as not-polluting.

In table 2.7, the absolute mean value and the corresponding standard deviation of the current magnitude errors are reported for loads L3, L4 and L5. With reference to the polluting loads, L3 and L4, the WLS estimations denote a lower mean error, but higher standard deviations. Whereas for load L5, since the WLS is the only algorithm which erroneously detects this load as polluter, both mean errors and standard deviations are much higher than zero. Similar

Table 2.7: Case 1, Absolute Means and Standard Deviations of current magnitude estimation errors for Loads L3, L4 and L5, harmonic under analysis $h = 3$.

	BOMP [A]		LBOMP [A]		WLS [A]	
	mean	*std*	*mean*	*std*	*mean*	*std*
L3	0.0012	0.1565	0.0012	0.1565	0.0007	0.1787
L4	0.0049	0.2432	0.0049	0.2432	0.0029	0.3696
L5	0	0	0	0	2.1232	1.0520

detection results can be found when performing the same analysis on the harmonic orders $h = 5$, $h = 7$, and $h = 9$, always considering loads L3 and L4 as polluting. The corresponding identification results are reported in the following tables (respectively table 2.8, table 2.9 and table 2.10 for the harmonic orders $h = 5$, $h = 7$, and $h = 9$), with reference to three different post-detection threshold levels: 0%, 0.5% and 5%.

Table 2.8: Case 1, Percentage of occurrence of source detection, with reference to three post-detection threshold levels, harmonic order under analysis $h = 5$

	BOMP [%]			LBOMP [%]			WLS [%]		
	0%	*0.5%*	*5%*	*0%*	*0.5%*	*5%*	*0%*	*0.5%*	*5%*
L2	0	0	0	0	0	0	100	98.42	13.97
L3	100	100	0	100	100	0	100	100	0
L4	100	100	0	100	100	0	100	100	0
L5	0	0	0	0	0	0	100	98.34	6.98

The results corresponding to the analysis of the 9-th harmonic order are interesting since the 0.5% post-detection threshold is equal to the value REF of

Table 2.9: Case 1, Percentage of occurrence of source detection, with reference to three post-detection threshold levels, harmonic order under analysis $h = 7$

	BOMP [%]			**LBOMP** [%]			**WLS** [%]		
	0%	*0.5%*	*5%*	*0%*	*0.5%*	*5%*	*0%*	*0.5%*	*5%*
L2	0	0	0	0	0	0	100	91.90	0
L3	100	0	0	100	100	0	100	100	0
L4	99.22	99.22	0	100	100	0	100	100	0
L5	0.78	0.78	0	0	0	0	100	86.04	0

Table 2.10: Case 1, Percentage of occurrence of source detection, with reference to three post-detection threshold levels, harmonic order under analysis $h = 9$

	BOMP [%]			**LBOMP** [%]			**WLS** [%]		
	0%	*0.5%*	*5%*	*0%*	*0.5%*	*5%*	*0%*	*0.5%*	*5%*
L2	0	0	0	0	0	0	100	59.31	0
L3	100	100	0	100	100	0	100	100	0
L4	100	45.36	0	100	45.36	0	100	49.60	0
L5	0	0	0	0	0	0	100	43.50	0

the forcing for load L4. By looking at figure 2.3, it is possible to see that, with reference to load L4, the detection function of all the techniques under study are characterized by the descending step in correspondence of the 0.5% threshold.
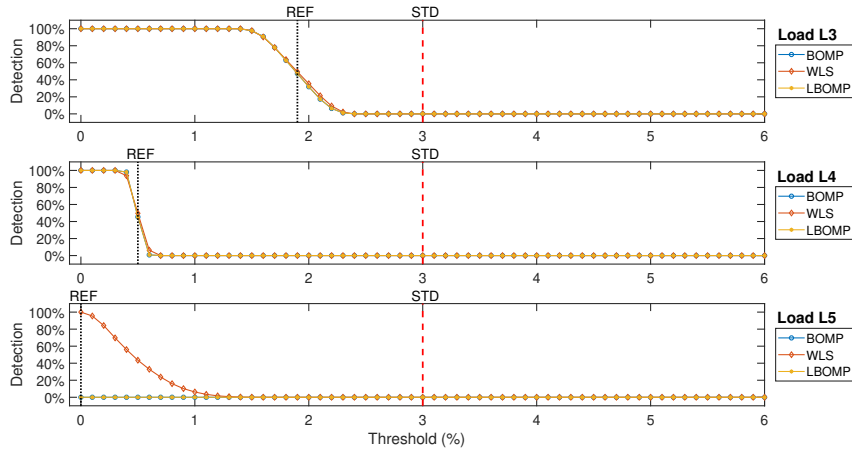
Figure 2.3: Harmonic detection - Case 1: forcing loads L3 and L4, harmonic order under analysis $h = 9$.

Also in this case, the WLS estimations are characterized by lower mean errors and higher standard deviations, as reported in table 2.11. The first analysis of Case 2 considers the harmonic order $h = 3$, and the corresponding detection functions are reported in figure 2.4. As expected, due the fact that the methodology estimates the values of all the entries, the WLS gives an erroneous detection

Table 2.11: Case 1, Absolute Means and Standard Deviations of current magnitude estimation errors for Loads L3, L4 and L5, harmonic under analysis $h = 9$

	BOMP [A]		LBOMP [A]		WLS [A]	
	mean	*std*	*mean*	*std*	*mean*	*std*
L3	0.0057	0.0716	0.0057	0.0716	0.0008	0.0755
L4	0.0114	0.0835	0.0113	0.0835	0.0015	0.1199
L5	0	0	0	0	0.3211	0.1885

of load L3 in the threshold range from 0% to 1%. The identification of load L4 instead, is perfect with all the techniques under analysis, whose detection functions are almost identical to step functions in correspondence of "REF" values. Both BOMP and LBOMP denote good identification performance also with reference to load L5, where the WLS is characterized by higher incorrect detection rates in the threshold range from 14% to 30%. This characteristic of the WLS leads to higher standard deviations, as shown in table 2.12.

Figure 2.4: Harmonic detection - Case 2: forcing loads L4 and L5, harmonic order under analysis $h = 3$.

Table 2.12: Case 2, Absolute Means and Standard Deviations of current magnitude estimation errors for Loads L4 and L5, harmonic under analysis $h = 3$

	BOMP [A]		LBOMP [A]		WLS [A]	
	mean	*std*	*mean*	*std*	*mean*	*std*
L4	0.0006	0.3669	0.0023	0.3653	0.0028	0.3656
L5	0.0081	0.4014	0.0071	0.4011	0.1279	2.2519

In figure 2.5, Case 2, forcing loads are L4 and L5, detection results are reported considering the fifth harmonic. As happened in Case 1 for load L5, also in this case load L3 is erroneously labelled as polluting by the WLS, whereas both

BOMP and LBOMP detection rates are always equal to 0%. Load L4 is perfectly detected (100%) by all the techniques under tests until the post-detection threshold is lower than the actual value of the forcing (REF). The detections of load L5 instead are slightly different for all the considered techniques. WLS gives the worst detection rate, starting from 100%, when a null threshold is applied, then the corresponding detection rate slowly decreases and reaches the 0% only when a 9% post-detection threshold is applied. Such detection function denotes highly incorrect detections also when the threshold is above the REF value. BOMP algorithm correctly detects load L5 as polluting only for 80% of the trials. Despite this, the detection curve is more similar to a step function, thus denoting a better overall detection with respect to the WLS. The LBOMP technique shows the best detection performance, with a perfect identification of load L5, for almost the entire threshold range between 0% and REF.
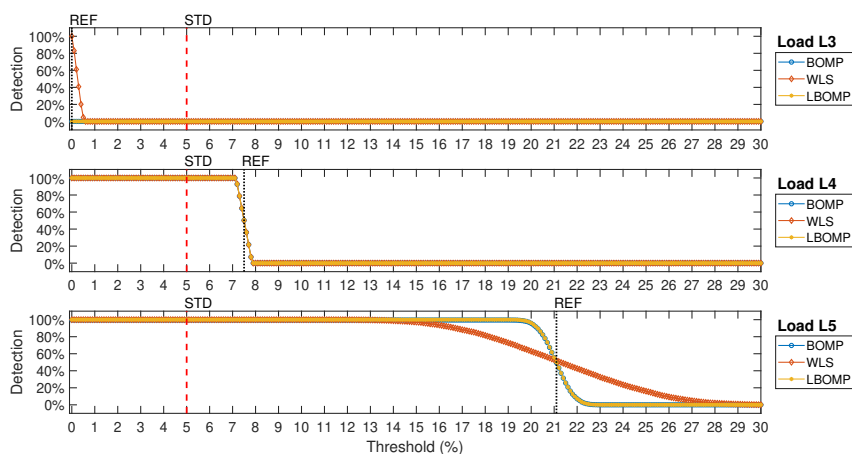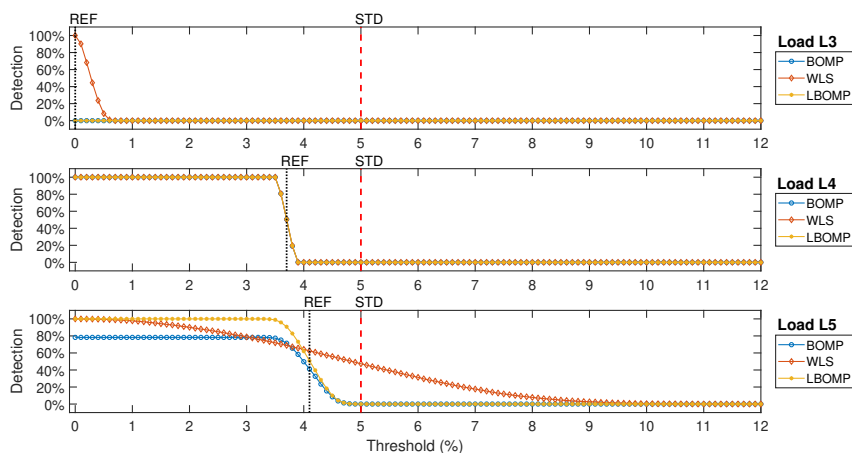

Figure 2.5: Harmonic detection - Case 2: forcing loads L4 and L5, harmonic order under analysis $h = 5$.

In this case, the mean errors and the standard deviations corresponding to the estimation errors of the current magnitudes of the polluting load, L4, obtained with the CS-based techniques, BOMP and LBOMP, are almost identical to the ones obtained with the WLS technique, as shown in table 2.13. It has to be notice that, both CS-based techniques are always characterized by the same values for both mean and standard deviation when they identify the same source as polluter. This is due to the fact that the two proposed algorithms differ only in the selection of the most correlated columns to the residuals (and thus the selection of the entries to be estimated). The estimation of the entries in both BOMP and LBOMP, is based on the least squares problem applied to an overdetermined system. Consequently, if the two techniques select the

columns referred to the same forcing, the estimated values are the same, since both measurements and measurement matrices are the same. In fact, since the LBOMP always identify load L5 as polluter (100%), contrarily to the BOMP (80%), the corresponding values of mean and standard deviation of the error differ.

Table 2.13: Case 2, Absolute Means and Standard Deviations of current magnitude estimation errors for Loads L4 and L5, harmonic under analysis $h = 5$

	BOMP [A]		**LBOMP [A]**		**WLS [A]**	
	mean	*std*	*mean*	*std*	*mean*	*std*
L4	0.0005	0.1713	0.0004	0.1713	0.0007	0.1722
L5	0.0124	0.1949	0.0043	0.1934	0.5055	1.3891

In order to test the robustness of the proposed global methodology, LBOMP, Case 3 is here considered. From the corresponding detection functions, which are shown in figure 2.6, it can be seen that all the methodologies correctly detect load L4 as polluter, until the post-detection threshold reaches the REF value. As seen in Case 1, load L5 is erroneously detected as polluting only by WLS method, with a percentage of cases which decreases with the increasing threshold. Still referring to the detection of load L5, it can be seen that also the single harmonic CS-based technique, BOMP, detects load L5 as polluter, for a small percentage of cases. This is again due to the implementation of the algorithm that, when looking for the two main polluting loads, detects load L5 instead of load L3.
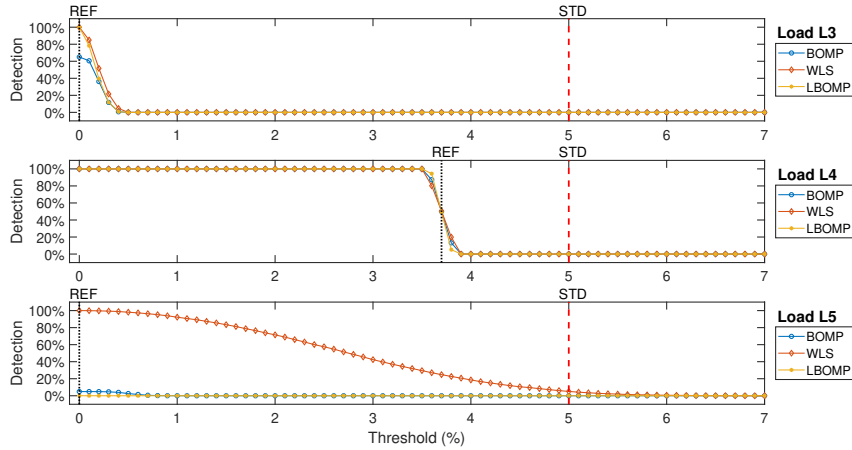

Figure 2.6: Harmonic detection - Case 3: forcing loads L3, not for the harmonic order under analysis, and L4, harmonic order under analysis $h = 5$.

The most interesting result of this test case is that related to the identification of load L3, which has been set as polluting for all the harmonic orders,

with exception to the one under analysis. The detection functions of all the methodologies underline how load L3 is detected as polluter when no threshold is considered but then, when the threshold increases, all the techniques label load L3 as non-polluting. This result is very important because, even when the threshold is applied, the LBOMP technique will still label load L3 as global harmonic polluter because of the other harmonic orders, with also the additional information that it does not pollute at the 5-th harmonic. Contrarily, when considering the techniques based on the analysis of a single harmonic order, BOMP and WLS, this load will be erroneously recognized as non-polluting.

In table 2.14, the percentage of identification, of all the possible polluting loads, are reported for the three methodologies considering three post-detection threshold levels: 0%, 0.5% (which is ten times lower than the STD value), and the limit of 5%, taken from the standard [49]. Here it is more evident that a threshold of 0.5% is sufficient to consider load L3 as non-polluting. Moreover, when considering a threshold equal to 5%, both CS-based techniques label all the loads as non-polluting, since the actual values of the forcing (REF) are lower than this limit. It is worth mentioning that, contrarily to the CS-based techniques, the WLS identifies loads L2 and L5 as polluters, also for threshold values higher than 5%, whereas load L4 is not recognized as polluter. This is of particular interest, since it denotes the poor reliability of the method, which gives a complete incorrect detection.

Table 2.14: Case 3, Percentage of occurrence of source detection for Loads L2, L3, L4, and L5, harmonic under analysis $h = 5$

	BOMP [%]			**LBOMP** [%]			**WLS** [%]		
	0%	*0.5%*	*5%*	*0%*	*0.5%*	*5%*	*0%*	*0.5%*	*5%*
L2	0	0	0	0	0	0	100	98.30	11.53
L3	65.02	0	0	100	0	0	100	0.01	0
L4	100	100	0	100	100	0	100	100	0
L5	4.9	2.58	0	0	0	0	100	98.12	5.08

The minimum value of mean errors for the estimations of load L3 forcing current, as shown in table 2.15, is obtained with the LBOMP technique, but the corresponding standard deviation is higher than that obtained with the BOMP. Contrarily, the BOMP gives the minimum mean estimation error for load L4, but with a standard deviation higher than that obtained with the LBOMP.

Moreover, it has to be noticed that the detection performance for the other harmonics are not affected by the fact that the 5-th harmonic forcing for load L3 has been set to zero.

As an example, the detection functions for harmonic orders $h = 3$ and $h = 7$ are shown, respectively, in figure 2.7 and figure 2.8.

Table 2.15: Case 3, Absolute Means and Standard Deviations of current magnitude estimation errors for Loads L3, and L4, harmonic under analysis $h = 5$

	BOMP [A]		LBOMP [A]		WLS [A]	
	mean	*std*	*mean*	*std*	*mean*	*std*
L3	0.0751	0.0283	0.0622	0.0314	0.0732	0.0356
L4	0.0006	0.1509	0.0030	0.1121	0.0007	0.1739
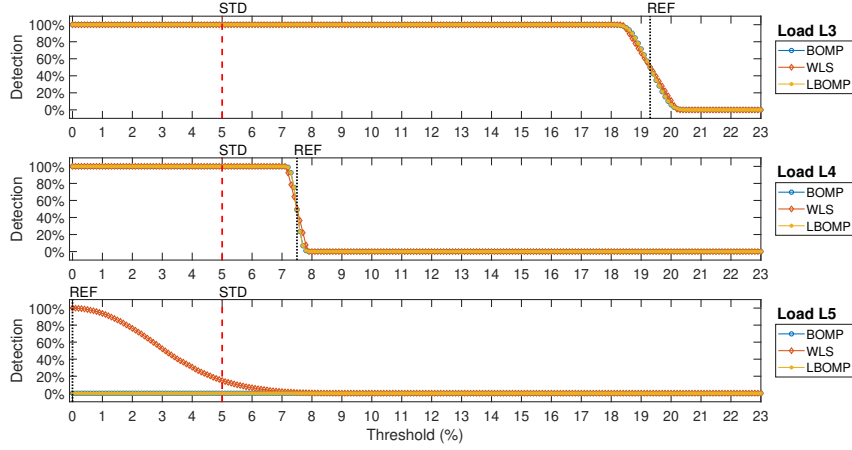
Figure 2.7: Harmonic detection - Case 3: forcing loads L3, not for the 5-th harmonic order, and L4, harmonic order under analysis $h = 3$.
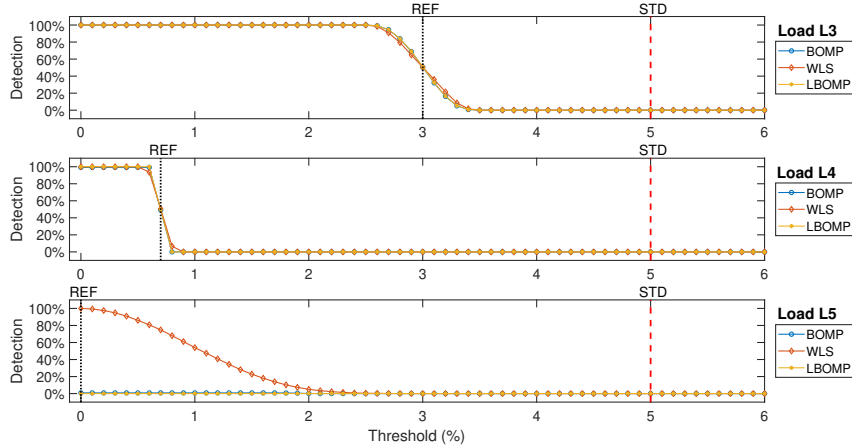
Figure 2.8: Harmonic detection - Case 3: forcing loads L3, not for the 5-th harmonic order, and L4, harmonic order under analysis $h = 7$.

To further test the robustness of the proposed methodologies, in Case 4 all loads are considered as polluters. In particular L2 and L5 are considered as poorly polluters, with a forcing current magnitude equal to 10% of the nominal values reported in table 2.5, whereas loads L3 and L4 are the main polluting loads with forcings equals to the nominal values.

The detection functions and the errors for Case 4, with reference to the 3-rd harmonic are reported respectively in figure 2.9 and table 2.16. The detection functions highlight how both CS-based methodologies correctly label loads L2 and L5 as non-polluters, contrarily to WLS. Despite this, by observing the detection of load L3, it can be seen that both BOMP and LBOMP overestimate its forcing value, which leads to erroneous detections for thresholds higher than the nominal value "REF". These results are also confirmed in table 2.16, where the WLS is characterized by lower mean errors for loads L3 and L4, but with higher standard deviations.

Table 2.16: Case 4, Absolute Means and Standard Deviations of current magnitude estimation errors for Loads L2, L3, L4, and L5; harmonic under analysis $h = 3$

	BOMP [A]		LBOMP [A]		WLS [A]	
	mean	*std*	*mean*	*std*	*mean*	*std*
L2	0	0	0	0	0.8669	0.6371
L3	0.4021	0.1567	0.4021	0.1567	0.0007	0.1782
L4	0.2570	0.2574	0.2570	0.2574	0.0028	0.3693
L5	0	0	0	0	1.1612	1.2015
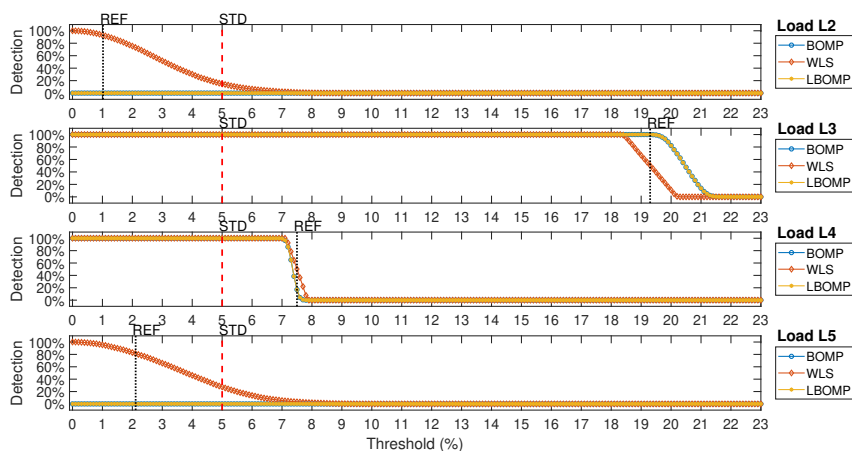
Figure 2.9: Harmonic detection - Case 4: forcing loads L3 and L4, with L2 and L5 forcing at 10% harmonic order under analysis $h = 3$.

When considering the harmonic order $h = 7$, the performances of BOMP and LBOMP differs, especially regarding the identifications of loads L4 and L5. As shown in figure 2.10, when a 0% threshold is considered, the BOMP, instead of selecting always the main polluting sources L3 and L4, chooses load L4 with a maximum occurrence of 80%. Moreover, load L5 is detected as polluter, with a 20% occurrence, even for threshold values higher than its actual forcing value. The LBOMP technique instead, always detects the main polluters loads, L3 and L4, even if its detection function starts to decrease for threshold values higher

than the REF value, denoting an overestimation of the corresponding forcing value.

Table 2.17: Case 4, Absolute Means and Standard Deviations of current magnitude estimation errors for Loads L2, L3, L4, and L5; harmonic under analysis $h = 7$

|	BOMP [A]		LBOMP [A]		WLS [A]	
	mean	*std*	*mean*	*std*	*mean*	*std*
L2	0	0	0	0	0.4539	0.2475
L3	0.0695	0.0621	0.0786	0.0587	0.0005	0.0710
L4	0.1067	0.0538	0.1061	0.0523	0.0012	0.1195
L5	0.8550	0.0473	0	0	0.4843	0.3351
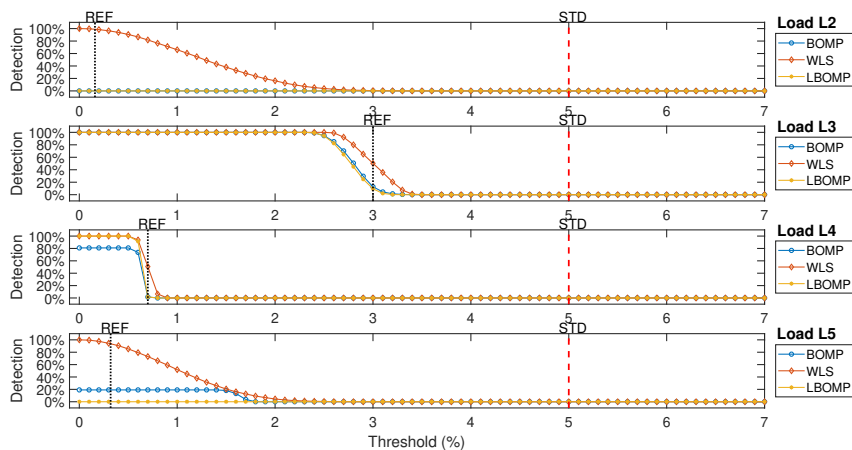
Figure 2.10: Harmonic detection - Case 4: forcing loads L3 and L4, with L2 and L5 forcing at 10% harmonic order under analysis $h = 7$.

It is worth mentioning that the same techniques can be directly applied to distribution networks with different nominal frequency, such as 50 Hz typically used in Europe. The different rated frequency of the system does not affect the methodological approach of the proposed algorithms, neither their performance. Despite this, it has to be noticed that a different fundamental frequency would affect the value of the reactances/susceptances, leading to a different model of the network. These differences must be taken into account when defining the measurement matrix which relates the measurements to the state of the system under study.

2.4 Conclusions

The limited resources in terms of monitoring devices, make unfeasible to apply classic analysis techniques, and alternative solutions are needed for the identi-

fication of the main harmonic sources. The Compressive Sensing seems to be a perfect solution for such problem, since it requires only a few information, and thus measurements, in order to identify and estimate the prevailing polluting sources connected to the grid. In this thesis, two Compressive Sensing based approaches have been proposed: the Block Orthogonal Matching Pursuit (BOMP), more specific, based on the analysis of the loads with reference to a single harmonic order, and the more general Load BOMP (LBOMP), in which the investigation is performed by considering, for each load, multiple harmonic order simultaneously. The BOMP can be successfully used when the operator has already the knowledge of the harmonic order which should be investigated, whereas the use of the LBOMP is instead more convenient for starting the analysis when no knowledge is available. Thanks to the modellization of each load/generator as the union of many different harmonic orders, the LBOMP allows labelling an element as polluter when it is generating a distortion for at least one of the considered harmonics. The tests here presented have shown, under realistic uncertainty scenarios, how the LBOMP is capable to correctly identify the main harmonic sources, and estimate their forcing values, not only in presence of few polluting sources with all the other loads non-polluting, but also when all the loads are somehow polluting with a forcing value lower than the prevailing one.

Chapter 3

Fault Location

Faults are one of the challenges in modern electric systems because their occurrence leads to critical operating conditions characterized by high currents flowing into the network. In order to reduce the damages associated to such conditions, the fault should be extinguished as soon as possible, and dedicated protection systems have been developed. The protections typically interrupt the power supply, with consequent effects also on the customers connected to the network. In particular, almost 80% of the customer interruptions occur due to distribution faults [63]. In general, they can be caused by bad weather events (storms, lightning, snow and freezing), insulation losses, and contact with external objects (typically branches) or animals (such as birds), and they can lead to physical damages of the line, which must be repaired in order to be able to re-establish the power supply to all the customers. Thus, a quick response from the Distribution System Operator (DSO) is needed, to locate and circumscribe the fault.

In particular, faults can be divided in different categories, depending on the phases involved in the fault or on the permanence of the failure. With regard to the involved phases, it is possible to distinguish between:

- *symmetrical faults*, which involves three phases (three-phase and three phase-to-ground faults). This kind of faults is the less common, around 5% of occurrence [64], but also the most serious one, due to the high fault currents;

- *asymmetrical faults*:

  - single line-to-ground faults, which are the most common with almost 70% of occurrence [64], and are usually due to lines coming in contact with the ground or the neutral cable because of wind or external objects;

– line-to-line and double line-to-ground faults, with 15% and 10% of oc-
currence respectively [64], are usually due to external objects landing
on the lines and can evolve in three-phase faults.

Temporary faults are typical of overhead lines, they represent about 75% -
90% [65], and usually are caused by multiple lines touching due to wind or birds,
but they can be also caused by tree branches touching the lines. This kind of
fault is cleared by disconnecting the faulty line, and thus restoring the dielectric
strength in the fault point. The procedure which allows to clear these faults is
carried out by an automated operation of the breakers, which open and reclose
the circuit with specific time sequence, called *Auto-Reclosure.* It is evident that,
even if the temporary faults affect the power supply for just a short time, they
must be investigated anyway, in order to verify that the grid has not be injured.

In case of permanent faults, the breakers are opened permanently to de-
energize the fault, with the consequent outage of the customers connected to
the involved sections. It is also possible that due to a cascade tripping, also
other parts of the network can be involved in the outage and, in some very
unlucky cases, a large blackout can occur.

Fault location techniques are thus important to provide accurate information
regarding the position of the fault to the maintenance crew. In fact, the high
costs of dedicated inspection devices for each line make this solution impractical.
Moreover, it is not feasible to visually inspect the entire fault section of the grid,
not only for the length of the section itself, but also for limitations due to rough
terrains (by ground), and trees covering the lines (by air).

Fault detection is the first step of the FLISR process: Fault Location, Iso-
lation and Supply Restoration. The order in the acronym reflects the sequence
of the procedure, and it is evident that the accurate location of the fault plays
a key role and could help to reduce costs and maintenance time.

3.1 State of the Art

Traditionally, short-circuit analysis of unbalanced faults in three-phase balanced
systems have been conducted by means of the symmetrical components. This
solution was suitable for transmission systems, but it cannot be applied to distri-
bution systems, which are typically unbalanced. The unequal mutual coupling
between phases, leads to mutual coupling between sequence network, and thus
there are no advantages in using symmetrical components [66].

Automatic fault location techniques can be divided in different categories,
based on:

- voltages and currents at the fundamental frequency, also known as impedance-based methods [67, 68]. These methods are the most frequently implemented in power systems, also because they are the cheapest and simplest to implement. Further classified in one-end methods or two-end methods, if the measurements are collected, respectively, only in the substation or in both substation and terminal node, they usually require the magnitudes of voltage and current; but also the phase angle can be used. The measure of the distance to the fault is given by the impedance of the faulted-line segment. The accuracy of these methods depends on many factors, especially on the fault resistance and the accuracy of both the model of the network and the measurements.

- travelling-waves methods [69, 70], which consider both voltage and current waves travelling at the speed of light from the fault towards the line terminals. The fault location is evaluated in terms of distance from the terminal, by considering the difference between the time required by the wave to be transmitted to the fault point and the time taken from the reflected wave to reach the measurement point. These methods are very accurate (e.g. the accuracy of the estimation does not vary depending on the load variance), but they are complex and costly, due to the required high sampling frequency.

- high-frequency components of voltages and currents generated by the fault [71], which are not largely used due to the complexity and the related costs. In fact, special tuned filters, and dedicated measurement devices, are required to measure the high-frequency components generated by the sudden change in the system. Depending on the application, the fault location can be determined by considering the entity of the high-frequency components or their travelling time.

- intelligence, such as neural network and machine learning [72, 73]. These algorithms are getting very popular, due to the possibility of solving complex problems. The ease of implementation is mainly given by the fact that it is not necessary to know the model of the system under study, but only measurements related to it. The performance of these approaches strictly depends on the training of the application and thus, the accuracy in the detection cannot be guaranteed. Limited available information, together with the low quality of the available data, make difficult to produce a well-trained algorithm. Moreover, every time that the network under study changes, a new training is required.

Nowadays, there is an increasing interest in Compressive Sensing-based tech-

niques [74–77], due to their ability in recovering sparse signals when few information are available. In fact, based on the assumption that the number of faults simultaneously occurring in the network is lower than the size of the network, the model of the system can be considered sparse. This approach is model-based, and thus allows to evaluate the performance of the algorithm in relation to the considered model of both network and measurements. In particular, measurements aspects that are usually avoided, such as the impact of the measurement uncertainties together with the inclusion of the branch current measurements, will be taken into account. In this thesis, CS methods are presented, and the fault analysis is modelled through the application of the superposition principle between two scenarios: pre-fault and during fault. In the following, the quantities related to the two scenarios will be respectively labelled with the subscripts *pre* and *dur* (for example, V_{pre} will denotes a pre-fault voltage, while I_{dur} denotes a during fault current).

3.2 Fault Model

In order to explain this approach, let us consider a generic distribution system as reported in figure 3.1a. The voltage in the generic point of the network, F, can be represented by a voltage, characterized by magnitude ($V_{F\,pre}$) and phase angle ($\phi_{F\,pre}$) so that $\overline{V}_{F\,pre} = V_{F\,pre}e^{j\phi_{F\,pre}}$.

The effect of a fault in node F can be represented by shorting out all the voltage sources, and adding a series element including a voltage source and a fault impedance, Z_F, as shown in figure 3.1b. This new source, the only one in the system, will be characterized by the same magnitude of the pre-fault one, but the phase angle will be shifted by $180°(\overline{V}_f^* = V_{F\,pre}e^{j(\phi_{F\,pre}+180°)})$ [78]. More specifically, this grid is also defined as *Thévenin*'s network and the corresponding voltages and currents represent the variations of both quantities due to the fault. According with figure 3.1d, the corresponding fault current, I_F, can be then determined as follow:

$$\overline{I}_F = \frac{\overline{V}_F^*}{\overline{z}_{th} + \overline{z}_F} \tag{3.1}$$

where $\overline{z}_{th}$ represents the Thévenin equivalent impedance of the network, seen from node F, and $\overline{z}_F$ is the fault impedance.

Due to the application of the superposition principle, is it possible to affirm that the during fault voltages and currents in the network are given by the sum of the pre-fault conditions with the changes given by the fault. Thus, by combining figure 3.1a and figure 3.1b the during fault network is the one represented in figure 3.1c.

(a) Pre-fault.

(b) Fault voltage variation.

(c) During-fault.

(d) Fault voltage variation, Thévenin's equivalent.

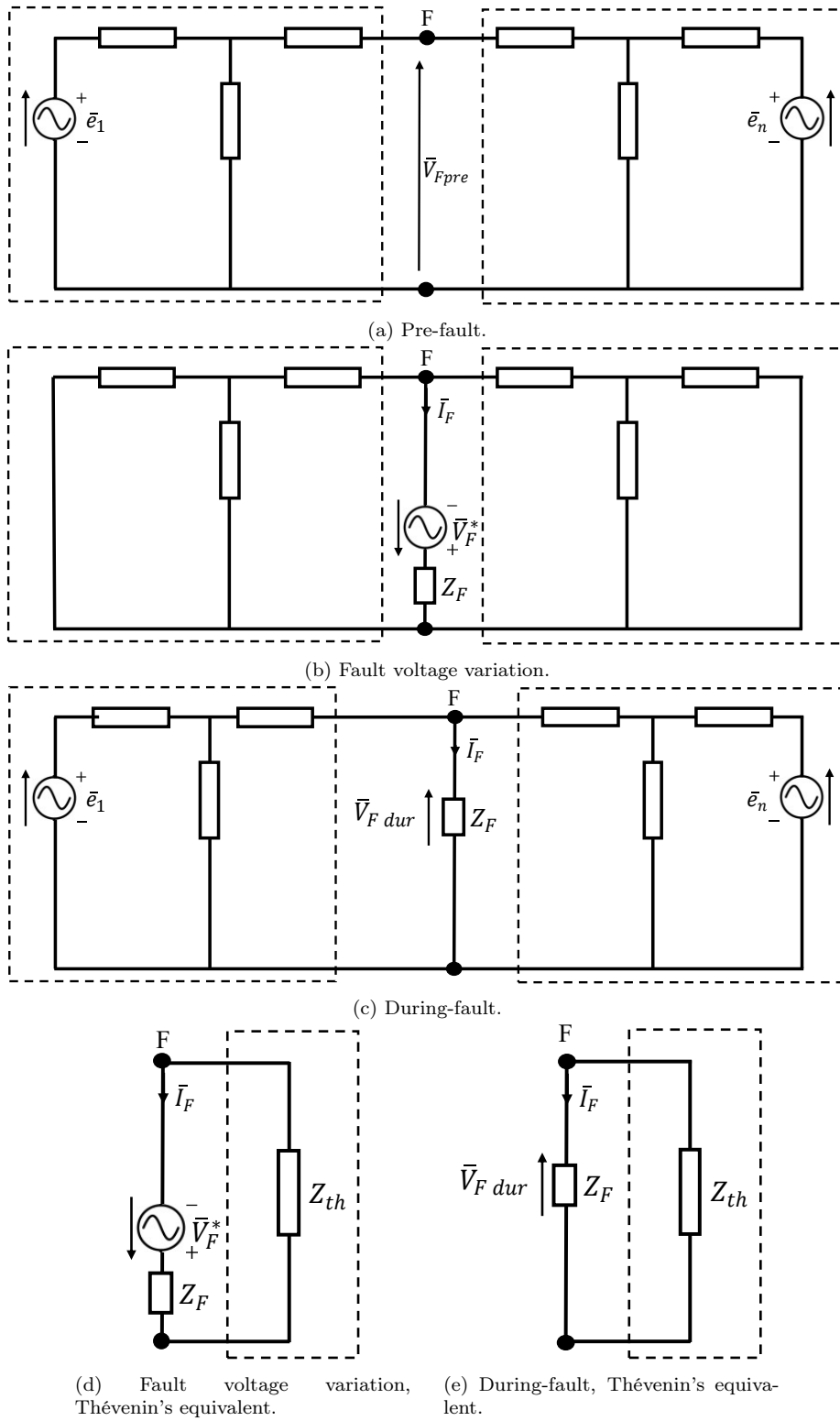(e) During-fault, Thévenin's equivalent.

Figure 3.1: Grid examples.

Consequently, during the fault, as it can be easily seen from the Thévenin's equivalent in figure 3.1e, the voltage in the node F will drops to the one across the fault impedance.

$$\overline{V}_{F\,dur} = \overline{z}_F \overline{I}_F \tag{3.2}$$

With this idea in mind, it is possible to express the mathematical model of the fault. Given a generic 3-phase N-bus distribution system, the pre-fault complex voltages, in magnitude and phase, in all the busses ($m = 3N$), can be related to the currents injected in each node:

$$\overline{\mathbf{V}}_{pre} = \overline{\mathbf{Z}}_{net} \cdot \overline{\mathbf{J}}_{pre} \tag{3.3}$$

where $\overline{\mathbf{V}} \in \mathbb{C}^m$ is a complex vector representing the voltages measured in the three phases of all the buses; $\overline{\mathbf{J}} \in \mathbb{C}^{3N}$ is the vector representing the complex currents injected into each phase of the N nodes of the considered network; $\overline{\mathbf{Z}}_{net} \in \mathbb{C}^{m \times n}$ is the overall impedance matrix of the network.

With reference to the impedance matrix of the network, $\overline{\mathbf{Z}}_{net}$, it has to be noticed that it should take into account all the components of the network, the parameters of lines, transformers and loads, and can be computed following the procedure described in [79]. In particular, every network component can be represented by using a 3-by-3 matrix where the diagonal elements describe the self-parameters for each phase, while the mutual parameters are reported as off-diagonal entries. It is interesting to note that the considered network representation, given by $\overline{\mathbf{Z}}_{net}$ and the corresponding admittance matrix $(\overline{\mathbf{Z}}_{net})^{-1} = \overline{\mathbf{Y}}_{net}$, can be adopted for any distribution system (medium or low voltage, balanced or unbalanced, etc.), since it allows considering:

- for the lines, both three-phase and single-phase lines as well as different characteristics of the conductors, and the π model is adopted for each branch. Typically, in distribution system power flow analysis, shunt admittances can be neglected due to their low value. However, for line-to-ground fault analysis, shunt susceptances play a key role in the path of the fault currents and therefore they must be considered. The corresponding shunt elements must be included in $\overline{\mathbf{Y}}_{net}$ by adding them to the associated node;

- for the substation, any transformer which can be represented by using a two-port scheme;

- for the loads, both balanced and unbalanced loads, since each one is represented in terms of phase coordinates. Starting from the nominal values of active and reactive powers and voltage of the ph-th phase (respectively

P_{ph},Q_{ph}, and V_{ph}), the admittance of the corresponding element is given by: $y_{ph} = [\frac{P_{ph}-Q_{ph}}{|V_{ph}|^2}]$;

In the following, for sake of simplicity, unless differently specified, we will refer to single-phase systems; it is evident that the same considerations can be extended considering three-phase systems.

When considering the impedance matrix, it is important to consider the meaning of each element. Given the impedance matrix of a N-bus system, it is possible to define two kind of elements:

- diagonal elements $\overline{z}_{i,i}$, which are usually termed as *driving point impedance* or *Thévenin's impedance* from the node i, whose value corresponds to the ratio between the voltage and the injected current at the i-th node (considering all the current sources connected to the other nodes equal to zero);

- off-diagonal elements $\overline{z}_{i,j}$, *transfer impedance*, between nodes i and j, since they are given by the ratio between the voltage at node i and the current injected at bus j when the current sources connected to the other nodes are neglected.

When a fault occurs in the system, the impedance matrix of the system should be modified, accordingly to the type of fault. For faults on nodes, the impedance of the fault, z_F, should be added to the driving point impedance of the affected node, while the rest of the impedance matrix remains the same. For example, considering a fault occurring on node i it follows:

$$\overline{z}_{i,i\,new} = \overline{z}_{i,i} + \overline{z}_F \tag{3.4}$$

and, consequently, the fault current is given by: $\overline{I}_F = \overline{V}_F^* / \overline{z}_{i,i\,new}$. It is worth mentioning that, depending on the fault, the matrix can be also considered constant (e.g. for faults with $\overline{z}_F = 0$).

Instead, the fault occurring on a branch can be modelled as a new node which must be introduced in the impedance matrix. Consequently, the cardinally of Z_{bus} becomes (N+1)-by-(N+1), (N+3)-by-(N+3) in case of a three-phase matrix. This lead to the necessity of recalculate the impedance matrix: the fault impedance must be added in correspondence of the new node, and the entries in correspondence of the nodes delimiting the faulted branch must be updated, since the topology of the system has changed. This procedure is not trivial, and it can be also carried out by firstly modifying the admittance matrix, and then calculating the impedance matrix.

As seen in figure 3.1b, the voltage variation on all the nodes, $\overline{\Delta \mathbf{V}}$, corresponding to one fault occurring in the F-th node, can be directly related to the

fault current, (3.1), injected in the fault node.

$$\overline{\Delta \mathbf{V}} = \overline{\mathbf{Z}}_{bus} \cdot \overline{\Delta \mathbf{J}}$$

$$
\begin{bmatrix} \overline{\Delta \mathbf{V}}_1 \\ \vdots \\ \overline{\Delta \mathbf{V}}_F \\ \vdots \\ \overline{\Delta \mathbf{V}}_N \end{bmatrix}
=
\begin{bmatrix}
\overline{z}_{1,1} & \cdots & \overline{z}_{1,f} & \cdots & \overline{z}_{1,N} \\
\vdots & \cdots & \vdots & \cdots & \vdots \\
\overline{z}_{f,1} & \cdots & \overline{z}_{f,f} & \cdots & z_{f,N} \\
\vdots & \cdots & \vdots & \cdots & \vdots \\
\overline{z}_{N,1} & \cdots & \overline{z}_{f,f} & \cdots & \overline{z}_{N,N}
\end{bmatrix}
\cdot
\begin{bmatrix} 0 \\ \vdots \\ -\overline{I}_F \\ \vdots \\ 0 \end{bmatrix}
\tag{3.5}
$$

In particular, since the only non-zero entry of $\overline{\Delta \mathbf{J}}$ is the one corresponding to the node affected by the fault:

$$
\begin{bmatrix} \overline{\Delta V}_1 \\ \vdots \\ \overline{\Delta V}_F \\ \vdots \\ \overline{\Delta V}_N \end{bmatrix}
=
\begin{bmatrix} -\overline{z}_{1,f}\overline{I}_F \\ \vdots \\ -\overline{z}_{f,f}\overline{I}_F \\ \vdots \\ -\overline{z}_{N,f}\overline{I}_F \end{bmatrix}
\tag{3.6}
$$

From a practical point of view, the voltage variation can be also determined by the difference between the during-fault and the pre-fault voltage profiles in the nodes, which merged with equation (3.5) leads to:

$$\overline{\Delta \mathbf{V}} = \overline{\mathbf{V}}_{dur} - \overline{\mathbf{V}}_{pre} = \overline{\mathbf{Z}}_{bus} \cdot \overline{\Delta \mathbf{J}}$$

$$
\begin{bmatrix} \overline{\Delta V}_1 \\ \vdots \\ \overline{\Delta V}_F \\ \vdots \\ \overline{\Delta V}_N \end{bmatrix}
=
\begin{bmatrix} \overline{\mathbf{V}}_{1\,dur} - \overline{\mathbf{V}}_{1\,pre} \\ \vdots \\ \overline{\mathbf{V}}_{F\,dur} - \overline{\mathbf{V}}_{F\,pre} \\ \vdots \\ \overline{\mathbf{V}}_{N\,dur} - \overline{\mathbf{V}}_{N\,pre} \end{bmatrix}
=
\begin{bmatrix}
\overline{z}_{1,1} & \cdots & \overline{z}_{1,f} & \cdots & \overline{z}_{1,N} \\
\vdots & \cdots & \vdots & \cdots & \vdots \\
\overline{z}_{f,1} & \cdots & \overline{z}_{f,f} & \cdots & z_{f,N} \\
\vdots & \cdots & \vdots & \cdots & \vdots \\
\overline{z}_{N,1} & \cdots & \overline{z}_{f,f} & \cdots & \overline{z}_{N,N}
\end{bmatrix}
\cdot
\begin{bmatrix} 0 \\ \vdots \\ -\overline{I}_F \\ \vdots \\ 0 \end{bmatrix}
$$

$$\tag{3.7}$$

The relation in eq. (3.7) is very important when practical analysis must be carried out, since it allows to avoid the calculations of the updated impedance matrix. In the reality, both pre- and during-fault voltage measurements might be available, and thus the following relation can be used to estimate the fault location:

$$\overline{\mathbf{V}}_{dur} - \overline{\mathbf{V}}_{pre} = \overline{\mathbf{Z}}_{bus} \cdot \overline{\Delta \mathbf{J}} + \overline{\mathbf{e}} \tag{3.8}$$

in which the entries of the vector $\overline{\mathbf{e}} \in \mathbb{C}^m$ are the complex measurement errors. The system in eq.(3.8) can be also expressed in terms of real and imagi-

nary components, in the following respectively denoted by the superscript r and x, as follows:

$$\begin{bmatrix} V_{1\,dur}^r - V_{1\,pre}^r \\ V_{1\,dur}^x - V_{1\,pre}^x \\ \vdots \\ V_{N\,dur}^r - V_{N\,pre}^r \\ V_{N\,dur}^x - V_{N\,pre}^x \end{bmatrix} = \begin{bmatrix} R_{11} & -X_{11} & \cdots & R_{1N} & -X_{1N} \\ X_{11} & R_{11} & & X_{1N} & R_{1N} \\ \vdots & & \ddots & & \vdots \\ R_{N1} & -X_{N1} & & R_{NN} & -X_{NN} \\ X_{N1} & R_{N1} & \cdots & X_{NN} & R_{NN} \end{bmatrix} \begin{bmatrix} J_{1\,dur}^r - J_{1\,pre}^r \\ J_{1\,dur}^x - J_{1\,pre}^x \\ \vdots \\ J_{N\,dur}^r - J_{N\,pre}^r \\ J_{N\,dur}^x - J_{N\,pre}^x \end{bmatrix} + \begin{bmatrix} e_1^r \\ e_1^x \\ \vdots \\ e_N^r \\ e_N^x \end{bmatrix}$$

$$\Delta\mathbf{V}^{rx} = \mathbf{Z}_{bus}^{rx}\,\Delta\mathbf{J}^{rx} + \mathbf{e}^{rx} \tag{3.9}$$

where $\mathbf{Z}_{bus}^{rx}$ is the impedance matrix in terms of real and imaginary components with $Z_{bus,hk} = R_{hk} + jX_{hk}$ the (h,k) entry of $\overline{\mathbf{Z}}_{bus}$.

It is worth to underline that, when considering the system in the form (3.9), each fault will lead to two non-zero components in the vector of the injected currents $\Delta\mathbf{J}^{rx}$, corresponding to the real and the imaginary component of the injected current.

Considering what has been presented above, the state vector of the system is sparse, with a sparsity level equal to the number of faults affecting the grid at the same time. Moreover, considering the limited number of available measurements, which characterize a realistic scenario, the resulting model is underdetermined. These two characteristics make this problem a perfect candidate for the Compressive Sensing approach.

The proposed CS-based algorithm for the fault detection is the BOMP, based on the Algorithm 2 presented in Section 1.6.3, which will be applied to the fault model expressed in real and imaginary components, as in (3.9). According to the formulation of the problem, each i-th block of the state vector $\Delta\mathbf{J}^{rx}$ will be considered with cardinality 2, and it will be composed of the real and the imaginary parts of $\overline{\Delta J}_i$.

3.3 Impact of Measurement Accuracy

Real measurements are characterized by their uncertainties, which can have an important impact on the performance of the implemented algorithm. In general, when the measurement errors are high, the corresponding measurements are not correctly representing the measurand, and the use of such information for the analysis of any system leads to unreliable results. In this regard, the decrease of the performance of a CS-based fault location algorithm due to the low measurement accuracy has been presented in [76]. In this section, the impact of real measurements will be underlined, by comparing the identification provided by a fault location compressive sensing-based algorithm, whose inputs

are measurements provided by devices with different accuracies.

The pre-fault and the during-fault scenarios are characterized by different dynamics, the first can be associated to a steady-state condition, with static signals, while the second one presents strongly dynamics signals. In this regard, it is worth mentioning the different performance of voltage transformers (VTs) in the two scenarios. With reference to steady-state conditions, pre-fault, the performance of the VTs are well defined in the standard [80]. Reference standard for voltage transformers (VTs), [80], provides different accuracy classes for measurements and protection purposes, characterized by different accuracy limits for both magnitude and phase angle. The corresponding limits, for both measurement and protection purpose are reported in table 3.1, labelled, respectively, with M or P in the first column.

Table 3.1: Accuracy requirements for voltage transformers [80]

Transformer purpose	Accuracy Class	Ratio error [%]	Phase displacement [± crad]
M	0.1	0.1	0.15
M	0.2	0.2	0.3
M	0.5	0.5	0.6
M	1	1.0	1.2
M	3	3.0	not specified
P	3P	3.0	3.5
P	6P	6.0	7.0

Traditional VTs were meant for just one purpose, measurement or protection. The possibility of choosing only one between the two options, M or P, was a huge limitation, since it was not possible using only one VT to properly monitor the same signal under different dynamic conditions. In a Smart Grid scenario, it is not reasonable to deal with devices characterized by such limitations. The management policies of the network will be based on the results deriving from the algorithms which, in turn, take the measurements collected from the system as input. The measurement chain is thus required to have an accuracy always limited in a certain range, despite the variability of the dynamics of the signal. Nowadays, new generation multipurpose low power voltage transformers (LPVT), which are suitable for both measuring and protection applications, are available. One of the main aspects of these new sensors is the no-saturation characteristic, since ferromagnetic cores are avoided, together with the linearity in the whole measurement range. These devices are also characterized by reduced size, compared to the conventional instrument transformers, and allow implementing more functions in combination with electronic relays. Moreover, due to the absence of the iron core, these sensors have a low energy consumption,

which also lead to a more stable temperature of the device. In the following analysis, the output of these new sensors will be considered to supply the data to the measurement devices, which are assumed to be PMUs.

In literature it is possible to find solutions that consider measurement provided by Smart Meters instead of PMUs [74,75,81,82], due to their lower costs in the range of $ 200. Nevertheless, it is worth mentioning that there is a massive ongoing research for developing low cost PMUs [83–85], with a forecasted price similar to the current price of a Smart Meter (which in turn is expected to decrease). Moreover, contrarily to PMUs, Smart Meters do not typically provide phase angle measurements, since the required synchronization system would increase the costs of the measurement devices, and thus the linear formulation of the problem in terms of phasors would be compromised. Even considering the availability of synchronization, Smart Meters are characterized by lower reporting rates, and measurement uncertainties higher than those of the PMUs, thus the implementation of such measurements in a fault location algorithm provides less accurate results [74,75].

The PMU performance is usually expressed in terms of Total Vector Error (TVE), a measure of the phasor difference between the synchrophasor estimated from a PMU and the reference one, as reported in the related standards on synchrophasor measurements (e.g. IEEE and IEC standards [86], [87] and [88]). Since the limits reported in the standards refer to the measured phasor, the limits on the magnitude and phase angle errors are determined based on this information. Given a generic phasor $\bar{P}$ and its measurement $\bar{P}_{measured}$, as shown in figure 3.2, the maximum TVE can be represented as a circumference centred in correspondence of the terminal point of $\bar{P}$, with radius equal to the maximum TVE (1% in figure 3.2).
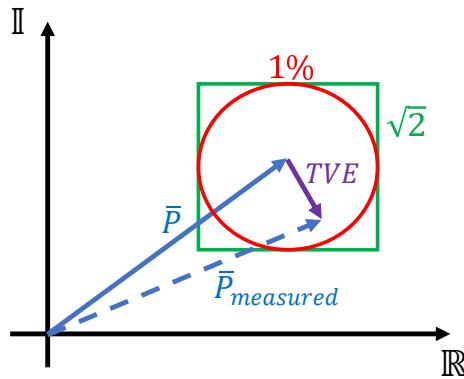
Figure 3.2: TVE approximation.

Consequently, in order to respect the limit on the maximum TVE, the terminal point of the measured phasor, $\bar{P}_{measured}$, should result inside/on the

circumference. It is evident that is not possible to define a unique limit on the maximum error for both magnitude and phase angle, here represented in rectangular coordinates. In fact, depending on the position on the circumference, the maximum error on the real component is obtained in correspondence of a null error of the imaginary component, and vice versa. In literature, it is common to consider the error equally split on both real and imaginary components, and the corresponding value is then obtained by dividing the TVE by $\sqrt{2}$.

As a consequence, the considered TVE limits of the standards and the corresponding limits defined as above are reported in table 3.2. Since these devices are meant to track the dynamic phenomena occurring in power systems, the standards clearly specify the different accuracy limits for both steady-state and dynamic scenarios.

Table 3.2: PMUs Maximum Accuracy Limits

Condition	TVE [%]	Magnitude [%]	Phase [crad]
Steady-state	1	0.7	0.7
Dynamic	3	2.1	2.1

Other works in literature rarely consider the impact of measurement accuracy on fault location algorithms. When considered, the measurement accuracy is modelled as a generic random noise added to the measurement, neglecting the requirements reported in the standards and the impact of different dynamics of the involved signals [75, 89, 90]. Consequently, the proposed algorithms are tested under non-realistic conditions, in which the measurements are considered more accurate than those available in the field, arising doubts on the efficacy of the proposed solutions. In this thesis, two different uncertainty scenarios will be considered:

- "static", denoted with $\mathbb{S}$ and characterized by the same uncertainty (steady-state) for both pre-fault and during-fault scenario;

- "static and dynamic", the most realistic one, denoted with $\mathbb{S}+\mathbb{D}$, in which the proper uncertainties are taken into account (steady-state conditions for pre-fault and dynamic conditions for during-fault).

In particular, since different VTs accuracy classes are available, this analysis will consider the two classes that are most common in distribution systems: 0.5 and $3P$ for measuring and protection purpose, respectively. The accuracy classes and the TVE limits for each uncertainty scenario are briefly summarized in table 3.3.

Table 3.3: Accuracy classes and maximum TVE for the uncertainty scenarios

	$\mathbb{S}$		$\mathbb{S} + \mathbb{D}$	
	pre fault	**fault**	**pre fault**	**fault**
VT class	0.5	0.5	0.5	3P
PMU TVE$_{max}$	1%	1%	1%	3%

The analysis will be carried out by means of 10000 Monte Carlo (MC) simulations, in which the uncertainty related to each measurement will be taken into account by adding a measurement uncertainty to the reference measurements. The errors will be extracted from uniform distributions, with limits based on the scenarios in table 3.3, defined in compliance with the standards of both VTs and PMUs.

The VT and PMU uncertainty contributions have been assumed to be independent and the same assumption has been done for magnitude and phase angle errors. Since each entry of the measurement vector $\overline{\mathbf{\Delta V}}$ is computed as the real or imaginary component of the difference of two voltage phasors measured at two different time instants, the corresponding uncertainty is given by the combination of the uncertainties of the pre and during fault phasors. Measurements corresponding to different time-tags are considered as independent.

3.3.1 Tests and Results

In order to properly test the proposed algorithm, the reference measurements have been obtained by simulating a distribution network on a Real Time Digital Simulator (RTDS), in combination with its software tool RSCAD. This powerful simulator allows to simulate power system dynamics, from DC up to 3 kHz, and thus to provide the detailed view of the network operating conditions during both normal and fault conditions. RTDS is also capable to provide phasors of both voltages and currents, which have been taken as reference values for the following analysis. In the following, in order to evaluate the performance of the proposed algorithm, and study the impact of different measurement accuracies on the results, simulations are conducted by considering only one single line-to-ground fault occurring at a given time. The block-sparsity of the CS model has been chosen accordingly as $S_b = 1$. Single-phase-to-ground faults are considered since these are the most common among the different types of fault [91].

Also in this case, to better study the performance of the proposed technique in a fully controlled environment, the chosen test grid is a small three-phase radial distribution system ($V_n = 20$ kV), composed by 7 nodes and 5 loads, as shown in figure 3.3. Nevertheless, the same technique can be easily applied on the analysis of bigger networks.

Table 3.4: Nominal Loads Configuration.

Load	P_n [kW]	Q_n [$kVAR$]
L1	50.00	20.00
L2	130.00	75.00
L3	90.00	40.00
L4	70.00	35.00
L5	80.00	40.00

Table 3.5: Pi-Model Configuration.

	$d - sequence$	$0 - sequence$
Z [Ω]	0.320+j0.170	1.050+j0.530
X_c [$M\Omega$]	0.0104	0.0107

The single-phase values of nominal active and reactive powers for each load are reported in table 3.4. Distribution lines have been modelled with a pi-model whose values, referred to both direct ($d-$) and zero ($0-$) sequences, are reported in table 3.5. The upstream network feeding the test grid has been modelled considering a short-circuit power equal to 500 MVA.

Firstly, the proposed BOMP-based solution, described in Section 3.2, has been tested in an ideal scenario, considering measurements without uncertainties and voltage phasor measurements available in every node. This solution, which actually does not correspond to any realistic scenario, can be considered as a calibration test, to prove the efficacy of the proposed algorithm. Moreover, since the gravity of the fault depends on the Phase of Waveform (POW), the phase angle in correspondence of the occurrence of the fault, different POWs have been considered: POW = 0°, 30°, 60°, and 90°. In table 3.6, the percentage of detection is reported considering POW = 0°. In this table, each row represents a possible fault node, while the percentages of detection are reported in column,
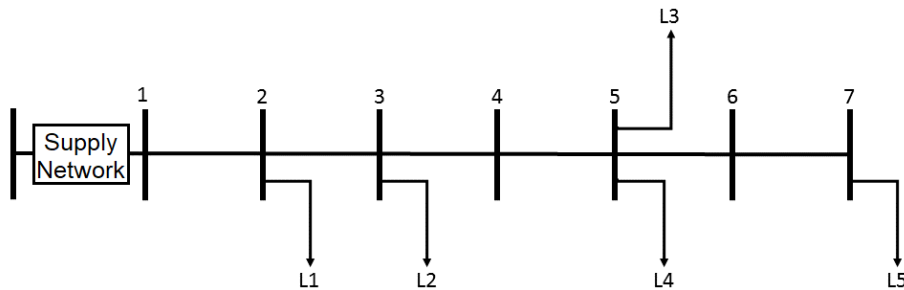
Figure 3.3: Test grid.

expressed as percentage computed in 10000 MC simulations.

Table 3.6: Percentages of fault detection, without uncertainties, all nodes monitored and POW = 0°

Bus number	Faulted bus					
	2 [%]	3 [%]	4 [%]	5 [%]	6 [%]	7 [%]
1	0	0	0	0	0	0
2	100	0	0	0	0	0
3	0	100	0	0	0	0
4	0	0	100	0	0	0
5	0	0	0	100	0	0
6	0	0	0	0	100	0
7	0	0	0	0	0	100

The results underline how the algorithm perfectly detects the faulty node, if no uncertainties are taken into account. Moreover, the same results are obtained also when different POWs (30°, 60°, and 90°) are considered. According to this, it is possible to affirm that the theoretical efficiency of the algorithm is proved, and the same methodology can be tested under more realistic conditions, in presence of measurement uncertainty.

Once the effectiveness of the proposed BOMP-based fault location algorithm have been established in a scenario without uncertainties, the performance can be evaluated by considering the uncertainty scenarios of table 3.3, and different cases reported in table 3.7, which correspond to four different meter placement configurations.

Table 3.7: Measurement placement in the different Test Cases

Test case	Voltage meas.
Case 1	$V_1, V_2, V_3, V_4, V_5, V_6, V_7$
Case 2	V_1, V_3, V_5, V_7
Case 3	V_1, V_4, V_7
Case 4	V_1, V_7

The different cases reported in table 3.7 are characterized by a decreasing number of voltage measurements because, as already discussed, distribution networks are not fully monitored, and it is fundamental to study the performance of the proposed solution in realistic scenarios. Otherwise, based on the results provided by a not properly tested algorithm, erroneous decision could be made, leading to an incorrect management of the network. The same configurations have been also tested without uncertainties, and the proposed identification algorithm has always correctly identified the node affected by the fault.

In tables 3.8 to 3.11, the detection of the faulty node are reported for the measurement scenario in Case 1, with reference to different POWs (respectively POW = 0°, POW = 30°, POW = 60°and POW = 90°). In the following tables, the performance of the algorithm are reported for both uncertainty scenarios $\mathbb{S}$ and $\mathbb{S} + \mathbb{D}$. By comparing these results with those presented above, when the measurement uncertainty was not taken into account, it is evident how, even if the voltages in all nodes are monitored and the system is completely observed, the uncertainties play a key role in the identification. The performance of the methodology, when the uncertainty scenario characterized by lower uncertainties, $\mathbb{S}$, is considered, slightly decrease with respect to the ideal scenario. The correct detection remains above 96% for all the nodes, and there are cases in which it remains equal to 100%. The more realistic uncertainty scenario instead, $\mathbb{S} + \mathbb{D}$, denotes performance strongly affected by measurement uncertainty. In particular, the percentage of correct detection decreases to 60%, which results in a not reliable detection. By comparing the results for both uncertainty scenarios, it is also evident how the more realistic scenario is also characterized by a higher spread of the incorrect identifications which involve, sometimes, also nodes which are far from the actual faulty one.

Table 3.8: Case 1, POW = 0°- Percentages of fault detection

Bus number	Faulted bus											
	2 [%]		3 [%]		4 [%]		5 [%]		6 [%]		7 [%]	
	$\mathbb{S}$	$\mathbb{S}+\mathbb{D}$	$\mathbb{S}$	$\mathbb{S}+\mathbb{D}$	$\mathbb{S}$	$\mathbb{S}+\mathbb{D}$	$\mathbb{S}$	$\mathbb{S}+\mathbb{D}$	$\mathbb{S}$	$\mathbb{S}+\mathbb{D}$	$\mathbb{S}$	$\mathbb{S}+\mathbb{D}$
1	0	0,57	0	0	0	0	0	0	0	0	0	0
2	100	98,80	0	2,72	0	0,01	0	0	0	0	0	0
3	0	0,63	100	93,69	0	6,44	0	0,11	0	0	0	0,01
4	0	0	0	3,59	100	85,47	0	11,19	0	1,10	0	0,51
5	0	0	0	0	0	7,99	99,89	74,40	0,42	16,77	0	4,74
6	0	0	0	0	0	0,09	0,11	13,29	97,99	60,08	3,26	22,54
7	0	0	0	0	0	0	0	1,01	1,59	22,05	96,74	72,20

Table 3.9: Case 1, POW = 30°- Percentages of fault detection

Bus number	Faulted bus											
	2 [%]		3 [%]		4 [%]		5 [%]		6 [%]		7 [%]	
	$\mathbb{S}$	$\mathbb{S}+\mathbb{D}$	$\mathbb{S}$	$\mathbb{S}+\mathbb{D}$	$\mathbb{S}$	$\mathbb{S}+\mathbb{D}$	$\mathbb{S}$	$\mathbb{S}+\mathbb{D}$	$\mathbb{S}$	$\mathbb{S}+\mathbb{D}$	$\mathbb{S}$	$\mathbb{S}+\mathbb{D}$
1	0	0,71	0	0	0	0	0	0	0	0	0	0
2	100	98,73	0	2,67	0	0,01	0	0	0	0	0	0
3	0	0,56	100	93,69	0	6,69	0	0,12	0	0	0	0,01
4	0	0	0	3,64	100	85,44	0	11,26	0	1,08	0	0,51
5	0	0	0	0	0	7,78	99,91	74,47	0,41	16,69	0	4,78
6	0	0	0	0	0	0,08	0,09	13,12	97,88	59,85	3,29	22,63
7	0	0	0	0	0	0	0	1,03	1,71	22,38	96,71	72,07

Table 3.10: Case 1, POW = 60°- Percentages of fault detection

Bus number	Faulted bus											
	2 [%]		3 [%]		4 [%]		5 [%]		6 [%]		7 [%]	
	$\mathbb{S}$	$\mathbb{S}+\mathbb{D}$	$\mathbb{S}$	$\mathbb{S}+\mathbb{D}$	$\mathbb{S}$	$\mathbb{S}+\mathbb{D}$	$\mathbb{S}$	$\mathbb{S}+\mathbb{D}$	$\mathbb{S}$	$\mathbb{S}+\mathbb{D}$	$\mathbb{S}$	$\mathbb{S}+\mathbb{D}$
1	0	0,76	0	0	0	0	0	0	0	0	0	0
2	100	98,69	0	2,56	0	0,01	0	0	0	0	0	0
3	0	0,55	100	93,75	0	6,34	0	0,11	0	0	0	0,01
4	0	0	0	3,69	100	85,44	0	11,21	0	1,24	0	0,51
5	0	0	0	0	0	8,10	99,88	74,36	0,56	17,52	0	4,81
6	0	0	0	0	0	0,11	0,12	13,31	98,43	60,93	3,23	22,46
7	0	0	0	0	0	0	0	1,01	1,01	20,31	96,77	72,21

Table 3.11: Case 1, POW = 90°- Percentages of fault detection

Bus number	Faulted bus											
	2 [%]		3 [%]		4 [%]		5 [%]		6 [%]		7 [%]	
	$\mathbb{S}$	$\mathbb{S}+\mathbb{D}$	$\mathbb{S}$	$\mathbb{S}+\mathbb{D}$	$\mathbb{S}$	$\mathbb{S}+\mathbb{D}$	$\mathbb{S}$	$\mathbb{S}+\mathbb{D}$	$\mathbb{S}$	$\mathbb{S}+\mathbb{D}$	$\mathbb{S}$	$\mathbb{S}+\mathbb{D}$
1	0	0,52	0	0	0	0	0	0	0	0	0	0
2	100	98,86	0	2,85	0	0,01	0	0	0	0	0	0
3	0	0,62	100	93,63	0	6,70	0	0,09	0	0,00	0	0,01
4	0	0	0	3,52	100	85,38	0	10,71	0	1,24	0	0,51
5	0	0	0	0	0	7,84	99,81	74,03	0,65	18,00	0	4,73
6	0	0	0	0	0	0,07	0,19	14,02	98,45	60,93	3,31	22,71
7	0	0	0	0	0	0	0	1,15	0,90	19,83	96,69	72,04

Table 3.12 reports the percentages of identification with reference to the measurement configuration of Case 2, when POW = 0°. As for Case 1, the correct identification strongly depends on the uncertainty level. By comparing these results to those of Case 1, it is also possible to see a small reduction in the performance related to both uncertainty scenarios, due to the lack of measurements. Moreover, the POW does not seem to affect the identification of the faulty nodes as shown in table 3.13, table 3.14 and table 3.15, for POW = 30°, 60°, and 90°, respectively.

Table 3.12: Case 2, POW = 0°- Percentages of fault detection

Bus number	Faulted bus											
	2 [%]		3 [%]		4 [%]		5 [%]		6 [%]		7 [%]	
	$\mathbb{S}$	$\mathbb{S}+\mathbb{D}$	$\mathbb{S}$	$\mathbb{S}+\mathbb{D}$	$\mathbb{S}$	$\mathbb{S}+\mathbb{D}$	$\mathbb{S}$	$\mathbb{S}+\mathbb{D}$	$\mathbb{S}$	$\mathbb{S}+\mathbb{D}$	$\mathbb{S}$	$\mathbb{S}+\mathbb{D}$
1	0	1,18	0	0	0	0	0	0	0	0	0	0
2	100	91,30	0	13,74	0	1,58	0	0,01	0	0,01	0	0
3	0	7,49	99,99	78,76	0,01	10,86	0	0,23	0	0,12	0	0,04
4	0	0,03	0,01	7,50	99,54	68,06	0,91	21,00	0	7,47	0	1,75
5	0	0	0	0	0,45	16,88	97,85	58,05	2,30	19,55	0	3,09
6	0	0	0	0	0	2,62	1,24	19,79	93,31	45,99	5,81	25,13
7	0	0	0	0	0	0	0,00	0,92	4,39	26,86	94,19	69,99

Table 3.13: Case 2, POW = 30°- Percentages of fault detection

Bus number	Faulted bus											
	2 [%]		3 [%]		4 [%]		5 [%]		6 [%]		7 [%]	
	$\mathbb{S}$	$\mathbb{S}+\mathbb{D}$	$\mathbb{S}$	$\mathbb{S}+\mathbb{D}$	$\mathbb{S}$	$\mathbb{S}+\mathbb{D}$	$\mathbb{S}$	$\mathbb{S}+\mathbb{D}$	$\mathbb{S}$	$\mathbb{S}+\mathbb{D}$	$\mathbb{S}$	$\mathbb{S}+\mathbb{D}$
1	0	1,32	0	0	0	0	0	0	0	0	0	0
2	100	92,04	0	13,69	0	1,47	0	0,01	0	0,01	0	0
3	0	6,62	99,99	78,71	0,02	11,26	0	0,23	0	0,09	0	0,04
4	0	0,02	0,01	7,60	99,59	68,30	0,92	21,19	0	7,18	0	1,70
5	0	0	0	0	0,39	16,50	97,82	57,78	2,26	19,66	0	3,16
6	0	0	0	0	0	2,47	1,26	19,87	93,25	46,13	5,97	25,32
7	0	0	0	0	0	0	0	0,92	4,49	26,93	94,03	69,78

Table 3.14: Case 2, POW = 60°- Percentages of fault detection

Bus number	Faulted bus											
	2 [%]		3 [%]		4 [%]		5 [%]		6 [%]		7 [%]	
	$\mathbb{S}$	$\mathbb{S}+\mathbb{D}$	$\mathbb{S}$	$\mathbb{S}+\mathbb{D}$	$\mathbb{S}$	$\mathbb{S}+\mathbb{D}$	$\mathbb{S}$	$\mathbb{S}+\mathbb{D}$	$\mathbb{S}$	$\mathbb{S}+\mathbb{D}$	$\mathbb{S}$	$\mathbb{S}+\mathbb{D}$
1	0	1,47	0	0	0	0	0	0	0	0	0	0
2	100	91,87	0	13,03	0	1,54	0	0,02	0	0,01	0	0
3	0	6,64	99,99	79,17	0,01	10,64	0	0,23	0	0,12	0	0,04
4	0	0,02	0,01	7,80	99,51	67,94	0,87	20,82	0	8,32	0	1,73
5	0	0	0	0	0,48	17,11	97,85	58,05	3,29	20,53	0	3,14
6	0	0	0	0	0	2,77	1,28	19,96	93,47	45,55	5,95	25,32
7	0	0	0	0	0	0	0	0,92	3,24	25,47	94,05	69,77

Table 3.15: Case 2, POW = 90°- Percentages of fault detection

Bus number	Faulted bus											
	2 [%]		3 [%]		4 [%]		5 [%]		6 [%]		7 [%]	
	$\mathbb{S}$	$\mathbb{S}+\mathbb{D}$	$\mathbb{S}$	$\mathbb{S}+\mathbb{D}$	$\mathbb{S}$	$\mathbb{S}+\mathbb{D}$	$\mathbb{S}$	$\mathbb{S}+\mathbb{D}$	$\mathbb{S}$	$\mathbb{S}+\mathbb{D}$	$\mathbb{S}$	$\mathbb{S}+\mathbb{D}$
1	0	1,03	0	0	0	0	0	0	0	0	0	0
2	100	91,72	0	14,94	0	1,62	0	0,01	0	0,01	0	0
3	0	7,22	99,99	77,83	0,02	11,24	0,00	0,21	0	0,12	0	0,04
4	0	0,03	0,01	7,23	99,59	68,28	0,70	20,07	0	8,20	0	1,70
5	0	0	0	0	0,39	16,47	97,44	57,70	3,87	21,19	0	3,14
6	0	0	0	0	0	2,39	1,86	21,02	93,30	45,61	5,98	25,31
7	0	0	0	0	0	0	0	0,99	2,83	24,87	94,02	69,81

The identification corresponding to the uncertainty scenario of Case 3 are reported in tables 3.16, 3.17, 3.18, and 3.19. Same considerations of the previous cases hold. The static scenario is still characterized by identification rates higher than 85%, while the more realistic scenario, $\mathbb{S}+\mathbb{D}$, reach the lower limit of 39%.

Table 3.16: Case 3, POW = 0°- Percentages of fault detection

Bus number	2 [%]		3 [%]		4 [%]		5 [%]		6 [%]		7 [%]	
	$\mathbb{S}$	$\mathbb{S}+\mathbb{D}$	$\mathbb{S}$	$\mathbb{S}+\mathbb{D}$	$\mathbb{S}$	$\mathbb{S}+\mathbb{D}$	$\mathbb{S}$	$\mathbb{S}+\mathbb{D}$	$\mathbb{S}$	$\mathbb{S}+\mathbb{D}$	$\mathbb{S}$	$\mathbb{S}+\mathbb{D}$
1	0	1,48	0	0	0	0	0	0	0	0	0	0
2	100	90,79	0,03	14,32	0	0,77	0	0,56	0	0,28	0	0,08
3	0	7,73	98,77	60,90	2,67	25,34	0,00	9,56	0	1,91	0	0,31
4	0	0	1,20	20,99	97,00	57,51	1,17	15,62	0	1,75	0	0,16
5	0	0	0	3,79	0,33	16,18	96,00	48,95	4,73	25,45	0	7,22
6	0	0	0	0	0	0,20	2,83	22,54	87,38	39,36	9,99	26,26
7	0	0	0	0	0	0	0	2,77	7,89	31,25	90,01	65,97

Table 3.17: Case 3, POW = 30°- Percentages of fault detection

Bus number	2 [%]		3 [%]		4 [%]		5 [%]		6 [%]		7 [%]	
	$\mathbb{S}$	$\mathbb{S}+\mathbb{D}$	$\mathbb{S}$	$\mathbb{S}+\mathbb{D}$	$\mathbb{S}$	$\mathbb{S}+\mathbb{D}$	$\mathbb{S}$	$\mathbb{S}+\mathbb{D}$	$\mathbb{S}$	$\mathbb{S}+\mathbb{D}$	$\mathbb{S}$	$\mathbb{S}+\mathbb{D}$
1	0	1,68	0	0	0	0	0	0	0	0	0	0
2	100	91,54	0,03	13,92	0	0,71	0	0,53	0	0,27	0	0,08
3	0	6,78	98,61	60,67	2,23	24,73	0	9,18	0	1,86	0	0,31
4	0	0	1,36	21,45	97,45	58,18	0,98	15,42	0	1,66	0	0,16
5	0	0	0	3,96	0,32	16,18	95,62	48,79	4,43	25,31	0	7,29
6	0	0	0	0	0	0,20	3,40	23,13	87,37	39,43	10,14	26,24
7	0	0	0	0	0	0	0	2,95	8,20	31,47	89,86	65,92

Table 3.18: Case 3, POW = 60°- Percentages of fault detection

Bus number	2 [%]		3 [%]		4 [%]		5 [%]		6 [%]		7 [%]	
	$\mathbb{S}$	$\mathbb{S}+\mathbb{D}$	$\mathbb{S}$	$\mathbb{S}+\mathbb{D}$	$\mathbb{S}$	$\mathbb{S}+\mathbb{D}$	$\mathbb{S}$	$\mathbb{S}+\mathbb{D}$	$\mathbb{S}$	$\mathbb{S}+\mathbb{D}$	$\mathbb{S}$	$\mathbb{S}+\mathbb{D}$
1	0	1,85	0	0	0	0	0	0	0	0	0	0
2	100	91,42	0,01	13,14	0	0,73	0	0,61	0	0,29	0	0,08
3	0	6,73	98,25	60,44	2,27	24,75	0,01	9,94	0	1,97	0	0,26
4	0	0	1,74	22,16	97,35	57,54	1,49	16,07	0	2,09	0	0,16
5	0	0	0	4,26	0,38	16,77	96,32	49,15	5,88	26,27	0	7,16
6	0	0	0	0	0	0,21	2,18	21,67	87,44	39,14	9,54	25,94
7	0	0	0	0	0	0	0	2,56	6,68	30,24	90,46	66,40

Table 3.19: Case 3, POW = 90°- Percentages of fault detection

Bus number	2 [%]		3 [%]		4 [%]		5 [%]		6 [%]		7 [%]	
	$\mathbb{S}$	$\mathbb{S}+\mathbb{D}$	$\mathbb{S}$	$\mathbb{S}+\mathbb{D}$	$\mathbb{S}$	$\mathbb{S}+\mathbb{D}$	$\mathbb{S}$	$\mathbb{S}+\mathbb{D}$	$\mathbb{S}$	$\mathbb{S}+\mathbb{D}$	$\mathbb{S}$	$\mathbb{S}+\mathbb{D}$
1	0	1,37	0	0	0	0	0	0	0	0	0	0
2	100	91,08	0,03	15,13	0	0,80	0	0,61	0	0,27	0	0,08
3	0	7,55	99,08	61,22	3,03	26,01	0,00	9,72	0	1,98	0	0,32
4	0	0	0,89	20,22	96,71	57,43	1,03	15,23	0	2,16	0	0,16
5	0	0	0	3,43	0,26	15,56	95,86	48,77	6,22	26,54	0	7,38
6	0	0	0	0	0	0,20	3,11	22,85	87,55	39,13	10,50	26,40
7	0	0	0	0	0	0	0	2,82	6,23	29,92	89,50	65,66

Finally, the identification results corresponding to the measurement config-
uration of Case 4 are reported in tables 3.20, 3.21, 3.22, and 3.23. This case

study is characterized by very low percentages of correct detection, for some nodes even lower than 20%, e.g. the identification of fault on node 6 with the realistic uncertainty scenario. It is evident how, under realistic measurement conditions, the fault location algorithm is no longer capable to provide accurate detections for all the fault conditions.

Table 3.20: Case 4, POW = 0°- Percentages of fault detection

| Bus number | Faulted bus | | | | | | | | | | | |
| | 2 [%] | | 3 [%] | | 4 [%] | | 5 [%] | | 6 [%] | | 7 [%] | |
	$\mathbb{S}$	$\mathbb{S}+\mathbb{D}$	$\mathbb{S}$	$\mathbb{S}+\mathbb{D}$	$\mathbb{S}$	$\mathbb{S}+\mathbb{D}$	$\mathbb{S}$	$\mathbb{S}+\mathbb{D}$	$\mathbb{S}$	$\mathbb{S}+\mathbb{D}$	$\mathbb{S}$	$\mathbb{S}+\mathbb{D}$
1	0	2,96	0	0	0	0	0	0	0	0	0	0
2	100	87,93	0,08	16,72	0	1,41	0	0,14	0	0	0	0
3	0	9,11	98,49	59,35	3,73	26,80	0	8,88	0	2,91	0	1,07
4	0	0	1,43	21,27	86,63	38,32	12,31	26,50	0,08	15,59	0	8,86
5	0	0	0	2,56	9,64	21,10	69,39	26,00	20,24	21,35	1,82	15,98
6	0	0	0	0,10	0	7,97	17,71	17,19	53,31	18,40	25,61	16,71
7	0	0	0	0	0	4,40	0,59	21,29	26,37	41,75	72,57	57,38

Table 3.21: Case 4, POW = 30°- Percentages of fault detection

| Bus number | Faulted bus | | | | | | | | | | | |
| | 2 [%] | | 3 [%] | | 4 [%] | | 5 [%] | | 6 [%] | | 7 [%] | |
	$\mathbb{S}$	$\mathbb{S}+\mathbb{D}$	$\mathbb{S}$	$\mathbb{S}+\mathbb{D}$	$\mathbb{S}$	$\mathbb{S}+\mathbb{D}$	$\mathbb{S}$	$\mathbb{S}+\mathbb{D}$	$\mathbb{S}$	$\mathbb{S}+\mathbb{D}$	$\mathbb{S}$	$\mathbb{S}+\mathbb{D}$
1	0	3,18	0	0	0	0	0	0	0	0	0	0
2	100	88,64	0,06	16,41	0	1,31	0	0,14	0	0	0	0
3	0	8,18	98,32	58,73	3,22	26,30	0	8,53	0	2,86	0	1,07
4	0	0	1,62	22,03	86,32	38,20	10,97	26,16	0,08	15,58	0	8,87
5	0	0	0	2,71	10,45	21,41	68,47	25,67	20,38	21,43	1,79	15,95
6	0	0	0	0,11	0,01	8,20	19,82	17,46	53,48	18,64	25,45	16,66
7	0	0	0	0,01	0	4,58	0,74	22,04	26,06	41,49	72,76	57,45

Table 3.22: Case 4, POW = 60°- Percentages of fault detection

| Bus number | Faulted bus | | | | | | | | | | | |
| | 2 [%] | | 3 [%] | | 4 [%] | | 5 [%] | | 6 [%] | | 7 [%] | |
	$\mathbb{S}$	$\mathbb{S}+\mathbb{D}$	$\mathbb{S}$	$\mathbb{S}+\mathbb{D}$	$\mathbb{S}$	$\mathbb{S}+\mathbb{D}$	$\mathbb{S}$	$\mathbb{S}+\mathbb{D}$	$\mathbb{S}$	$\mathbb{S}+\mathbb{D}$	$\mathbb{S}$	$\mathbb{S}+\mathbb{D}$
1	0	3,51	0	0	0	0	0	0	0	0	0	0
2	100	88,55	0,01	15,38	0	1,31	0	0,17	0	0,01	0	0
3	0	7,94	97,73	58,53	3,13	26,21	0	9,23	0	2,95	0	1,01
4	0	0	2,26	23,03	85,88	38,04	13,73	27,08	0,09	15,57	0	8,60
5	0	0	0	2,87	10,98	21,52	69,86	25,97	20,03	21,15	1,56	15,83
6	0	0	0	0,18	0,01	8,23	15,94	17,00	52,83	18,31	24,11	16,51
7	0	0	0	0,01	0	4,69	0,47	20,55	27,05	42,01	74,33	58,05

Table 3.23: Case 4, POW = 90°- Percentages of fault detection

Bus number	Faulted bus											
	2 [%]		3 [%]		4 [%]		5 [%]		6 [%]		7 [%]	
	$\mathbb{S}$	$\mathbb{S}+\mathbb{D}$	$\mathbb{S}$	$\mathbb{S}+\mathbb{D}$	$\mathbb{S}$	$\mathbb{S}+\mathbb{D}$	$\mathbb{S}$	$\mathbb{S}+\mathbb{D}$	$\mathbb{S}$	$\mathbb{S}+\mathbb{D}$	$\mathbb{S}$	$\mathbb{S}+\mathbb{D}$
1	0	2,57	0	0	0	0	0	0	0	0	0	0
2	100	88,26	0,12	17,92	0	1,47	0	0,15	0	0	0	0
3	0	9,17	98,85	59,48	4,34	27,58	0	9,08	0	2,95	0	1,10
4	0	0	1,03	20,29	87,53	38,60	13,13	26,93	0,08	15,45	0	9,19
5	0	0	0	2,21	8,13	20,67	69,81	25,82	19,62	21,15	2,10	16,31
6	0	0	0	0,10	0	7,62	16,55	17,18	53,00	18,34	27,45	16,72
7	0	0	0	0	0	4,06	0,51	20,84	27,30	42,11	70,45	56,68

The algorithm here proposed, similarly to other proposals in the literature, was perfectly capable of identifying the node affected by the fault, when no uncertainties or moderate ones are considered. But the results reported above underline how, it is extremely important to correctly assess fault location algorithm performance in the presence of realistic measurement uncertainties.

3.4   Fault on branch

Once the impact of the measurement uncertainties has been established, a second consideration regarding the fault location must be done. The model presented above, (3.9), can be easily applied for analysis involving faults occurring at the nodes. However, it has to be noticed that faults occur also along the branches of the network. These kinds of faults can be detected by considering a modified version of the modellization presented above.

In these cases, the impedance matrix, and thus the model of the system itself, changes, as if a virtual node has been created. Since it is not possible to know a priori the exact location of the fault, the corresponding model cannot be built properly. As proposed in [92], starting from the model of eq.(3.9), the fault occurring on a branch can be modelled by means of two current injection contributions, coming from the nodes delimiting the branch, as shown in figure 3.4.
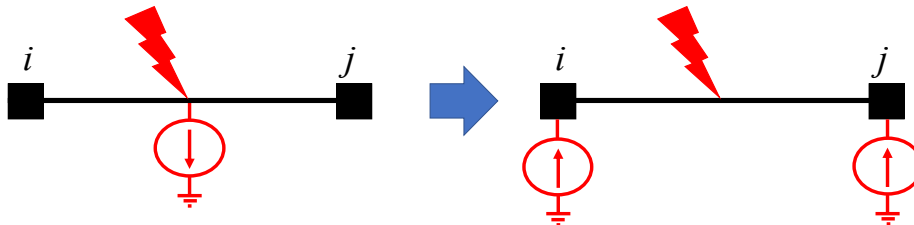
Figure 3.4: Fault on branches, source model.

The proposed fault location algorithm, based on the identification of the

nodes delimiting the branch involved in the fault is reported in the following Algorithm 3 box.

Algorithm 3 Block Orthogonal Matching Pursuit (BOMP) for fault location in branches

---

Input: $\mathbf{r}_0 = \mathbf{V}_{dur}^{rx}$, $\mathbf{A}_b^* = [\quad]$, S_b, $it = 1$

1: find, and select, one of the two nodes contributing to the fault, by applying the BOMP algorithm to the system in the form (3.9), considering a block-sparsity level $S_b = 1$;

2: identify all the branches converging to the selected node, i, and the corresponding terminal nodes;

3: for each pair of nodes (i, j) delimiting the branches identified in the previous step, build the sub-matrix $\mathbf{Z}_{bus,ij}^{rx}$ composed of the related column blocks i and j;

4: for each pair of nodes (i, j), estimate their resulting current injections by solving $\overline{\Delta \mathbf{J}_{ij}^{rx}} = \mathbf{Z}_{bus,ij}^{rx+} \cdot \Delta \mathbf{V}^{rx}$, where $\mathbf{Z}_{bus,ij}^{rx+}$ is the pseudo-inverse of $\mathbf{Z}_{bus,ij}^{rx}$;

5: identify the branch associated to the pair of nodes (i, j) with the largest overall current injection (calculated as the magnitude of the sum of the contributions at the two nodes) and label it as the faulty branch.

Output: $\Delta \mathbf{J}^{rx}$

To better understand the presented algorithm, a small example is reported in the following. Starting from the system in figure 3.5, a single line-to-ground fault is considered on the branch included between node 2 and node 3.
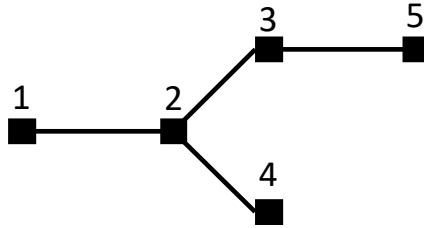
Figure 3.5: Example grid.

Through the application of the BOMP algorithm, step 1, the proposed technique identifies one node among node 2 and node 3, as one of the two contributing to the fault current. Let us suppose that the identified node is node 2. Consequently, all the branches converging to this node are selected and their terminal nodes are eligible to be selected as second contributors to the fault. In this step, the incidence matrix of the system can be used to identify the pairs of nodes delimiting each branch. In fact, as shown in (3.10) for the example grid in figure 3.5, this matrix contains as many rows as the number of branches of the network, and as many columns as the number of nodes. The entries of each row are set to 1 in correspondence of the columns which represent the terminal

nodes of the considered branch, otherwise are zeros.

$$\mathbf{A}_{inc} = \begin{array}{c} \\ branch~1 \\ branch~2 \\ branch~3 \\ branch~4 \end{array} \overset{\displaystyle \begin{array}{ccccc} bus~1 & bus~2 & bus~3 & bus~4 & bus5 \end{array}}{\left[\begin{array}{ccccc} 1 & 1 & 0 & 0 & 0 \\ 0 & 1 & 1 & 0 & 0 \\ 0 & 1 & 0 & 1 & 0 \\ 0 & 0 & 1 & 0 & 1 \end{array}\right]} \qquad (3.10)$$

The use of the incidence matrix makes the identification of the branches converging to the node, i, selected during the first step, immediate. This branches correspond to the rows of $\mathbf{A}_{inc}$ whose entries are 1 in correspondence of the column associated to bus i. Then, by inspecting these rows, the delimiting nodes of the branches are automatically determined. In the considered example, node 2 corresponds to the second column of $\mathbf{A}_{inc}$, and thus the possible pair of nodes which should be investigated, and considered during the following steps, are: (1,2), (3,2) and (4,2). The estimation of the contributions provided by each pair of nodes, as reported in step 4, is then carried out by solving the following equations:

$$\Delta \mathbf{J}_{12}^{rx} = \mathbf{Z}_{bus,12}^{rx+} \cdot \Delta \mathbf{V}^{rx} \qquad (3.11a)$$

$$\Delta \mathbf{J}_{32}^{rx} = \mathbf{Z}_{bus,32}^{rx+} \cdot \Delta \mathbf{V}^{rx} \qquad (3.11b)$$

$$\Delta \mathbf{J}_{42}^{rx} = \mathbf{Z}_{bus,42}^{rx+} \cdot \Delta \mathbf{V}^{rx} \qquad (3.11c)$$

where $\Delta \mathbf{J}_{ij}^{rx}$ is the subset of the state vector $\Delta \mathbf{J}^{rx}$ that includes only the current injections at nodes i and j, while $\mathbf{Z}_{bus,ij}^{rx+}$ is the already mentioned pseudo-inverse of the matrix obtained extracting from $\mathbf{Z}_{bus}^{rx}$ only the column blocks related to nodes i and j. Finally, in step 5, the estimated current injections are compared with each other to detect the faulty branch. In the example here considered, the pair of nodes (3,2) should give the largest overall injection to allow the correct identification of the fault location.

3.4.1 Tests and Results

The proposed algorithm is now tested on the same test grid proposed in Section 3.3.1. Obviously, in this case, the faults will be simulated along the branches. In particular, three different fault positions are considered for each branch: 25%, 50%, and 75% of the length of the considered branch. Only one fault at the time will be considered.

Also in these tests, different measurement scenarios are considered, according to those reported in table 3.7, thus:

- Case 1, the ideal and less realistic one, in which the voltages in all nodes are considered monitored;

- Case 2, where the number of measurements is reduced to one every two nodes;

- Case 3, the voltages are measured every three nodes;

- Case 4, which considers a measurement placement with only two nodes monitored, the substation (node 1) and the last node of the network (node 7).

For sake of simplicity, the first results presented refer to the ideal scenario when no uncertainties are considered. Even if this scenario is not realistic, it allows to better understand the performance of the proposed algorithm, with reference to the contributions of the delimiting nodes to the fault current.

For all measurement scenarios, the proposed algorithm provides a perfect identification of the faulted branch. In table 3.24 and table 3.25 the identification of the fault branch is reported for Case 1 and Case 4 respectively. For each possible fault, rows, the detected branches, columns, are reported. These results validate the algorithm under ideal conditions, since a perfect detection is obtained for every possible fault.

Table 3.24: Case 1 without uncertainties - branch fault detection

Faulty	Detected branch [%]					
section	1	2	3	4	5	6
1 25%	**100**	0	0	0	0	0
1 50%	**100**	0	0	0	0	0
1 75%	**100**	0	0	0	0	0
2 25%	0	**100**	0	0	0	0
2 50%	0	**100**	0	0	0	0
2 75%	0	**100**	0	0	0	0
3 25%	0	0	**100**	0	0	0
3 50%	0	0	**100**	0	0	0
3 75%	0	0	**100**	0	0	0
4 25%	0	0	0	**100**	0	0
4 50%	0	0	0	**100**	0	0
4 75%	0	0	0	**100**	0	0
5 25%	0	0	0	0	**100**	0
5 50%	0	0	0	0	**100**	0
5 75%	0	0	0	0	**100**	0
6 25%	0	0	0	0	0	**100**
6 50%	0	0	0	0	0	**100**
6 75%	0	0	0	0	0	**100**

Table 3.25: Case 4 without uncertainties - branch fault detection

Faulty section	Detected branch [%]					
	1	2	3	4	5	6
1 25%	**100**	0	0	0	0	0
1 50%	**100**	0	0	0	0	0
1 75%	**100**	0	0	0	0	0
2 25%	0	**100**	0	0	0	0
2 50%	0	**100**	0	0	0	0
2 75%	0	**100**	0	0	0	0
3 25%	0	0	**100**	0	0	0
3 50%	0	0	**100**	0	0	0
3 75%	0	0	**100**	0	0	0
4 25%	0	0	0	**100**	0	0
4 50%	0	0	0	**100**	0	0
4 75%	0	0	0	**100**	0	0
5 25%	0	0	0	0	**100**	0
5 50%	0	0	0	0	**100**	0
5 75%	0	0	0	0	**100**	0
6 25%	0	0	0	0	0	**100**
6 50%	0	0	0	0	0	**100**
6 75%	0	0	0	0	0	**100**

An interesting information of these tests is also the relation between the contribution of the delimiting nodes to the fault current and the position of the fault. In fact, according to the results presented in [92], through the comparison of the contributions of the current injections estimated with Algorithm 3, it is possible to estimate, indicatively, the section of the branch in which the fault occurred. Since the overall fault current is given by the sum of the two contributions ($I_F = \left\|\Delta\mathbf{J}_i^{rx} + \Delta\mathbf{J}_j^{rx}\right\|_2$), the percentage of the contribution given by each node is:

$$J_i = \frac{\left\|\Delta\mathbf{J}_i^{rx}\right\|_2}{I_F} \times 100 \qquad J_j = \frac{\left\|\Delta\mathbf{J}_j^{rx}\right\|_2}{I_F} \times 100 \qquad (3.12)$$

Consequently, with reference to the example proposed above, if node 2 will result in a contribution of $J_2 = 20\%$ the fault will probably be more close to node 3 (which will have a contribution of $J_3 = 80\%$), most likely nearby the last 20% of the branch.

Table 3.26 reports the results of this analysis, for Case 1. Here, for each considered fault, the contributions of the nodes delimiting the branch identified as fault are reported. The values are reported in percentage with respect to the overall estimated fault current. For example, let us consider the result corresponding to the fault on branch 4. From table 3.26 it is possible to see that when the fault occurs at 25% of the branch, the higher contribution to the fault comes from node 4 (88%), while node 5 contributes for just the 12%.

Table 3.26: Case 1 without uncertainties - node current injection contributions

Faulty	Injecting bus [%]						
section	1	2	3	4	5	6	7
1 25%	84,38	15,62	0	0	0	0	0
1 50%	37,90	62,10	0	0	0	0	0
1 75%	6,24	93,76	0	0	0	0	0
2 25%	0	85,67	14,33	0	0	0	0
2 50%	0	39,89	60,11	0	0	0	0
2 75%	0	6,77	93,23	0	0	0	0
3 25%	0	0	87,01	12,99	0	0	0
3 50%	0	0	42,85	57,15	0	0	0
3 75%	0	0	7,61	92,39	0	0	0
4 25%	0	0	0	88,08	11,92	0	0
4 50%	0	0	0	44,88	55,12	0	0
4 75%	0	0	0	8,38	91,62	0	0
5 25%	0	0	0	0	88,66	11,34	0
5 50%	0	0	0	0	46,49	53,51	0
5 75%	0	0	0	0	9,05	90,95	0
6 25%	0	0	0	0	0	89,55	10,45
6 50%	0	0	0	0	0	48,64	51,36
6 75%	0	0	0	0	0	9,85	90,15

When the fault occurs at 50% of the branch, the contributions are more balanced: 45% from node 4 and 55% from node 5. Whereas, for a fault occurring at 75% of the branch, the higher contribution (92%) comes from bus 5. A similar behaviour can be seen for all the branches, with only few cases in which this relation is less balanced. Same considerations hold also for Case 2, Case 3 and Case 4, as shown, respectively, in tables 3.27 to 3.29.

Table 3.27: Case 2 without uncertainties - node current injection contributions

Faulty	Injecting bus [%]						
section	1	2	3	4	5	6	7
1 25%	85,05	14,95	0	0	0	0	0
1 50%	39,14	60,86	0	0	0	0	0
1 75%	6,54	93,46	0	0	0	0	0
2 25%	0	85,37	14,63	0	0	0	0
2 50%	0	39,06	60,94	0	0	0	0
2 75%	0	6,58	93,42	0	0	0	0
3 25%	0	0	87,28	12,72	0	0	0
3 50%	0	0	43,46	56,54	0	0	0
3 75%	0	0	7,79	92,21	0	0	0
4 25%	0	0	0	87,82	12,18	0	0
4 50%	0	0	0	43,97	56,03	0	0
4 75%	0	0	0	8,06	91,94	0	0
5 25%	0	0	0	0	88,82	11,18	0
5 50%	0	0	0	0	46,76	53,24	0
5 75%	0	0	0	0	9,16	90,84	0
6 25%	0	0	0	0	0	89,15	10,85
6 50%	0	0	0	0	0	47,45	52,55
6 75%	0	0	0	0	0	9,39	90,61

Table 3.28: Case 3 without uncertainties - node current injection contributions

Faulty section	Injecting bus [%]						
	1	2	3	4	5	6	7
1 25%	**85,49**	**14,51**	0	0	0	0	0
1 50%	**40,21**	**59,79**	0	0	0	0	0
1 75%	**6,76**	**93,24**	0	0	0	0	0
2 25%	0	**85,71**	**14,29**	0	0	0	0
2 50%	0	**39,68**	**60,32**	0	0	0	0
2 75%	0	**6,70**	**93,30**	0	0	0	0
3 25%	0	0	**86,27**	**13,73**	0	0	0
3 50%	0	0	**41,12**	**58,88**	0	0	0
3 75%	0	0	**7,40**	**92,60**	0	0	0
4 25%	0	0	0	**88,58**	**11,42**	0	0
4 50%	0	0	0	**45,73**	**54,27**	0	0
4 75%	0	0	0	**8,49**	**91,51**	0	0
5 25%	0	0	0	0	**88,62**	**11,38**	0
5 50%	0	0	0	0	**45,74**	**54,26**	0
5 75%	0	0	0	0	**8,94**	**91,06**	0
6 25%	0	0	0	0	0	**89,09**	**10,91**
6 50%	0	0	0	0	0	**45,53**	**54,47**
6 75%	0	0	0	0	0	**9,48**	**90,52**

Table 3.29: Case 4 without uncertainties - Node current injection contributions

Faulty section	Injecting bus [%]						
	1	2	3	4	5	6	7
1 25%	**86,59**	**13,41**	0	0	0	0	0
1 50%	**42,31**	**57,69**	0	0	0	0	0
1 75%	**7,31**	**92,69**	0	0	0	0	0
2 25%	0	**86,50**	**13,50**	0	0	0	0
2 50%	0	**41,26**	**58,74**	0	0	0	0
2 75%	0	**7,07**	**92,93**	0	0	0	0
3 25%	0	0	**86,73**	**13,27**	0	0	0
3 50%	0	0	**41,81**	**58,19**	0	0	0
3 75%	0	0	**7,59**	**92,41**	0	0	0
4 25%	0	0	0	**87,74**	**12,26**	0	0
4 50%	0	0	0	**44,76**	**55,24**	0	0
4 75%	0	0	0	**8,11**	**91,89**	0	0
5 25%	0	0	0	0	**88,82**	**11,18**	0
5 50%	0	0	0	0	**43,63**	**56,37**	0
5 75%	0	0	0	0	**8,86**	**91,14**	0
6 25%	0	0	0	0	0	**89,74**	**10,26**
6 50%	0	0	0	0	0	**46,67**	**53,33**
6 75%	0	0	0	0	0	**9,87**	**90,13**

Now, the performance of the fault location technique will be evaluated by considering the most realistic uncertainty scenario presented in the previous section: $\mathbb{S}+\mathbb{D}$. The following analysis will be conducted by performing 10000 MC simulations for each considered fault. During each MC trial the measurement

error will be extracted from a uniform distribution, with limits defined according to the accuracy classes in table 3.30.

Table 3.30: Identification of faults on branches, uncertainty scenarios

	$\mathbb{S} + \mathbb{D}$	
	pre-fault	**during-fault**
VT class	0.5	3P
PMU TVE_{max}	1%	3%

Table 3.31 reports the percentage of identification of the faulty branch for Case 1. As expected, due to the uncertainty scenario, the performance of the proposed algorithm, which was perfectly identifying the faulty branch when no uncertainties were considered, strongly decreases. The impact of the measurement error is even more evident when the others measurement placement configurations are considered. Case 2, Case 3 and Case 4 results are reported, respectively in table 3.32, table 3.33 and table 3.34.

Table 3.31: Case 1 with uncertainties - Branch fault detection

Faulty section	Detected branch [%]					
	1	**2**	**3**	**4**	**5**	**6**
1 25%	**100**	0	0	0	0	0
1 50%	**98,60**	1,40	0	0	0	0
1 75%	**81,15**	18,85	0	0	0	0
2 25%	14,62	**85,14**	0,24	0	0	0
2 50%	2,74	**92,52**	4,74	0	0	0
2 75%	0,52	**76,87**	22,60	0	0	0
3 25%	0	22,27	**76,15**	1,57	0	0
3 50%	0	7,54	**83,14**	9,28	0	0
3 75%	0	2,22	**71,04**	26,56	0,18	0
4 25%	0	0,17	27,93	**67,51**	4,33	0
4 50%	0	0,04	13,37	**72,49**	13,73	0,37
4 75%	0	0	5,90	**64,36**	28,54	1,18
5 25%	0	0	1,23	32,84	**56,18**	9,75
5 50%	0	0	0,69	19,92	**59,78**	19,61
5 75%	0	0	0,38	11,26	**56,50**	31,86
6 25%	0	0	0	4,74	36,75	**58,35**
6 50%	0	0	0	3,51	27,02	**69,32**
6 75%	0	0	0	2,67	19,34	**77,88**

Looking at the identification percentages reported in these tables it is possible to see how, when the number of measurement is reduced, the proposed algorithm begin to identify less accurately the faulty branch and erroneously identify not only the branches directly connected to the faulty one, but also branches which are more distant. In such scenario, the measurement uncertainties not only impact on the identification of the faulty branch, but can also affect the estimation of the contribution of the delimiting nodes to the fault current, and thus the estimation of the branch section which is affected by the fault.

Single phase-to-ground faults are characterized by lower fault currents, and higher unbalances in the system, with respect to three phase-to-ground faults.

Table 3.32: Case 2 with uncertainties - branch fault detection

Faulty section	Detected branch [%]					
	1	**2**	**3**	**4**	**5**	**6**
1 25%	**100**	0	0	0	0	0
1 50%	**99,73**	0,27	0	0	0	0
1 75%	**87,05**	12,94	0,01	0	0	0
2 25%	28,01	**63,87**	8,12	0	0	0
2 50%	12,03	**66,18**	21,79	0	0	0
2 75%	4,95	**57,00**	38,05	0	0	0
3 25%	1,29	26,07	**70,93**	1,69	0,02	0
3 50%	0,83	14,22	**75,57**	9,05	0,33	0
3 75%	0,49	6,94	**67,69**	22,57	2,26	0,05
4 25%	0,09	1,28	36,90	**45,72**	15,29	0,72
4 50%	0,05	0,64	23,41	**49,14**	25,40	1,36
4 75%	0,03	0,19	13,92	**47,09**	36,34	2,43
5 25%	0,01	0,04	6,63	31,47	**51,08**	10,77
5 50%	0,01	0,02	5,12	22,79	**51,34**	20,72
5 75%	0,01	0,02	4,20	15,86	**47,94**	31,97
6 25%	0,01	0,01	2,51	7,54	33,47	**56,46**
6 50%	0	0,01	1,78	4,86	26,20	**67,15**
6 75%	0	0,02	1,32	2,92	20,32	**75,42**

Table 3.33: Case 3 with uncertainties - Branch fault detection

Faulty section	Detected branch [%]					
	1	**2**	**3**	**4**	**5**	**6**
1 25%	**100**	0	0	0	0	0
1 50%	**99,44**	0,56	0	0	0	0
1 75%	**86,24**	13,76	0	0	0	0
2 25%	28,22	**69,80**	1,92	0,06	0	0
2 50%	12,43	**77,28**	8,97	1,31	0,01	0
2 75%	5,32	**69,38**	19,50	5,72	0,08	0
3 25%	0,88	42,80	**32,17**	23,77	0,38	0
3 50%	0,50	31,43	**32,82**	34,39	0,86	0
3 75%	0,22	22,33	**31,66**	44,31	1,48	0
4 25%	0,11	13,06	21,21	**58,21**	7,33	0,08
4 50%	0,10	10,89	14,72	**56,99**	16,67	0,63
4 75%	0,10	8,65	9,73	**51,31**	27,60	2,61
5 25%	0,13	4,79	3,86	34,82	**42,55**	13,85
5 50%	0,13	3,13	2,32	27,21	**44,10**	23,11
5 75%	0,12	2,34	1,38	19,78	**43,53**	32,85
6 25%	0,05	1,21	0,49	9,77	35,98	**52,50**
6 50%	0,05	0,69	0,32	6,60	31,09	**61,25**
6 75%	0,03	0,48	0,20	4,74	26,42	**68,13**

According to the compressive sensing theory, the ability to recover sparse signals in presence of measurement errors, depends not only on the bound of the measurement errors, but also on the entity of the non-zero entries which one

wants to recover. In this regard, it is clearly of interest to study the performance of the proposed algorithm, also in presence of a three phase-to-ground fault.

Table 3.34: Case 4 with uncertainties - Branch fault detection

Faulty section	Detected branch [%]					
	1	2	3	4	5	6
1 25%	**100**	0	0	0	0	0
1 50%	**98,91**	1,09	0	0	0	0
1 75%	**84,42**	15,58	0	0	0	0
2 25%	30,01	**67,49**	2,50	0	0	0
2 50%	14,69	**73,82**	11,36	0,13	0	0
2 75%	6,63	**66,96**	24,99	1,42	0	0
3 25%	1,44	43,35	**42,52**	10,91	1,63	0,15
3 50%	0,71	31,77	**45,84**	16,96	3,86	0,86
3 75%	0,43	23,41	**44,63**	22,04	6,99	2,50
4 25%	0,16	12,36	37,64	**28,10**	12,81	8,93
4 50%	0,10	8,89	33,69	**28,58**	15,44	13,30
4 75%	0,08	6,13	29,03	**29,07**	17,46	18,23
5 25%	0,02	3,33	21,19	27,27	**19,61**	28,58
5 50%	0,01	2,29	18,00	25,97	**19,87**	33,86
5 75%	0,01	1,73	15,47	24,31	**19,61**	38,87
6 25%	0	0,95	11,19	20,47	19,43	**47,96**
6 50%	0	0,69	9,62	18,72	18,76	**52,21**
6 75%	0	0,53	8,22	17,35	18,21	**55,69**

In table 3.35 the percentages of identification in case of three phase-to-ground fault, considering the measurement configuration of Case 4, are reported.

Table 3.35: Case 4 with uncertainties, 3 phase-to-ground faults - Branch fault detection

Faulty section	Detected branch [%]					
	1	2	3	4	5	6
1 25%	**100**	0	0	0	0	0
1 50%	**100**	0	0	0	0	0
1 75%	**100**	0	0	0	0	0
2 25%	0	**100**	0	0	0	0
2 50%	0	**100**	0	0	0	0
2 75%	0	**100**	0	0	0	0
3 25%	0	0	**99,80**	0	0	0
3 50%	0	0	**100**	0	0	0
3 75%	0	0	**96,77**	3,23	0	0
4 25%	0	0	8,37	**91,63**	0	0
4 50%	0	0	0,10	**99,36**	0,54	0
4 75%	0	0	0	**87,89**	12,11	0
5 25%	0	0	0	20,92	**78,80**	0,28
5 50%	0	0	0	3,25	**91,02**	5,73
5 75%	0	0	0	0,27	**80,65**	19,08
6 25%	0	0	0	0	30,75	**69,25**
6 50%	0	0	0	0	9,76	**90,24**
6 75%	0	0	0	0	2,46	**97,54**

Contrarily to the results presented in table 3.34, here the algorithm provides a more accurate detection, which reaches the minimum level of 70% only in the case of a fault occurring at the beginning of branch 6 (first 25% of the branch). Moreover, when an incorrect detection occurs, the identified branch is always adjacent to the actual faulty one.

Such performance is very interesting, since obtained by considering just two voltage measurements, one in the substation and one at the end of the grid.

In this scenario, also the analysis of the contributions of the delimiting nodes, to the fault current, is possible. In figure 3.6 the statistics of the occurrences depending on the contribution of node 5, when faults occur on branch 4, are presented. The contribution given by node 5 is presented on the x-axis with a resolution of 10%, where 0% denotes no contribution and 100% indicates that the fault current is entirely injected by node 5. Consequently, the histogram bar between two percentages, c_1 and c_2, represents the number of trials in which the contribution of node 5 to the fault current was between c_1 and c_2. For faults occurring at 25% of the branch, the contribution provided by node 5 is, in general, very low (it is lower than 30% for more than 6000 MC trials) which corresponds to a higher contribution coming from the other delimiting node, node 4. Same considerations hold for a fault occurring in the final section of the branch, in which the higher contribution is given by node 5. Instead, when faults occurring at 50% of the network are considered, it is evident how, in this particular case, the identification of the faulty section is less accurate, but it still gives an interesting indication.
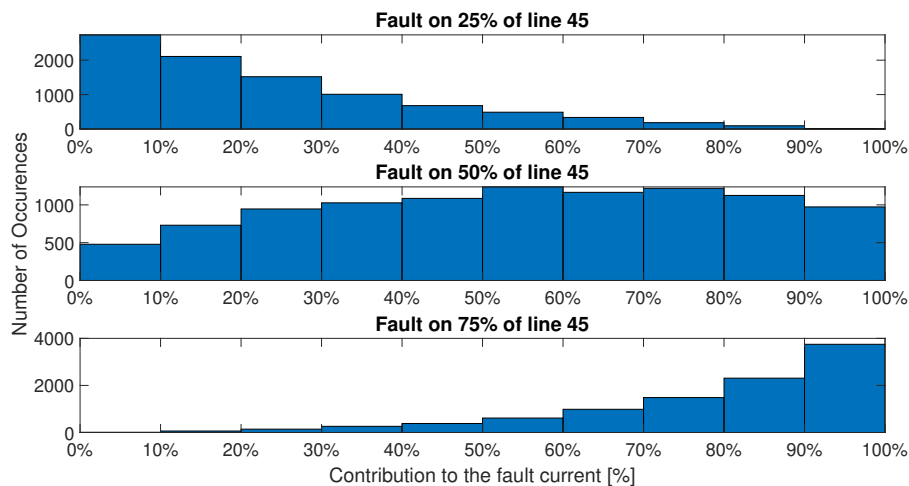
Figure 3.6: Case 4 with uncertainties, 3 phase-to-ground faults - Fault on line 4-5, contribution of node 5 to the fault.

Instead, as shown in figure 3.7, considering the contributions of node 4 to

faults on line 3, also in the case of faults occurring in the middle of the branch, the analysis of the contributions allows a better location of the fault.
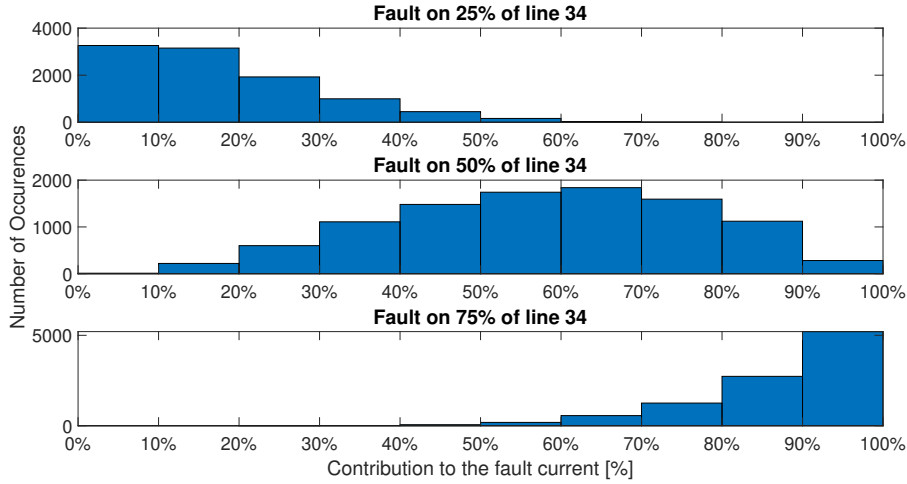
Figure 3.7: Case 4 with uncertainties, 3 phase-to-ground faults - Fault on line 3-4, contribution of node 4 to the fault.

When the measurement uncertainties are neglected, the algorithm here presented allows to perfectly identify the faulty nodes and branches. In particular, through the analysis of the current contribution given by the terminal nodes of the faulty branch, it has been shown that further information on the exact location of the fault can be carried out. Nevertheless, a degradation of the performance occurs when the measurement uncertainties are taken into account, especially when single line-to-ground faults are considered. This is due to the measurement uncertainties, which are particularly high due to the dynamics of the involved signals. Additional information should be added, in order to improve the performance of the CS-based algorithm.

3.5   Impact of branch current measurements

Until now, only voltage measurements have been considered. Usually, current measurements were neglected in fault location applications, due to the saturation of the current transformers and the consequent high uncertainties of the measurements provided in the during-fault scenario [75, 93]. Nowadays, when considering a realistic measurement scenario for smart grid applications, it is reasonable to think on the availability of measurement transformers suitable for this purpose, such as the low power current transformers (LPCT) that are the corresponding of the LPVT for current measurements. To avoid the iron core,

the working principle of these sensors is typically based on the Rogowski coil. Moreover, it is worth mentioning that combined low power transformers, which permits to monitor both voltage and current by merging the characteristics of both LPVT and LPCT, are commercially available [94, 95]. Using combined transformers together with PMUs, which allows to measure both voltages and currents with just one device, it is possible to improve the performance of the fault location algorithm with a limited number of measurement points.

In this regard, with reference to the identification of faults occurring on nodes, the model of the system under analysis presented in (3.8) should be modified, in order to include also the branch currents measurement:

$$\begin{bmatrix} \overline{\Delta \mathbf{V}} \\ \overline{\Delta \mathbf{I}_{br}} \end{bmatrix} = \begin{bmatrix} \overline{\mathbf{A}}_V \\ \overline{\mathbf{A}}_I \end{bmatrix} \overline{\Delta \mathbf{I}} + \overline{\mathbf{e}} \tag{3.13}$$

where $\overline{\Delta \mathbf{V}} \in \mathbb{C}^{m_v}$ is the vector of the m_v measured voltage variations between pre- and during fault conditions, $\overline{\Delta \mathbf{I}}_{br} \in \mathbb{C}^{m_i}$ is a similar vector including the m_i measured branch current phasor variations between pre- and during fault scenario, $\overline{\mathbf{A}}_V \in \mathbb{C}^{m_v \times n}$ is the sub-matrix linking the voltage measurements to the state vector, and $\overline{\mathbf{A}}_I \in \mathbb{C}^{m_i \times n}$ is the sensing matrix that describes the measured branch currents as functions of the bus current injections within the state vector.

In particular, if the voltage $\overline{V}_j$ at the bus j is measured, the corresponding row in $\overline{\mathbf{A}}_V$ is the j-th row of the network impedance matrix $\overline{\mathbf{Z}}_{bus}$. Instead, the row of matrix $\overline{\mathbf{A}}_I$ corresponding to the measurements of the current flowing from bus i to bus j, is obtained by multiplying a row vector composed of admittance terms by the impedance matrix $\overline{\mathbf{Z}}_{bus}$. Consequently, the sensing matrix of (3.13) can be also expressed as:

$$\overline{\mathbf{A}} = \begin{bmatrix} \overline{\mathbf{A}}_V \\ \overline{\mathbf{A}}_I \end{bmatrix} = \begin{bmatrix} \overline{\mathbf{L}}_V \\ \overline{\mathbf{L}}_I \end{bmatrix} \cdot \overline{\mathbf{Z}}_{net} \tag{3.14}$$

where $\overline{\mathbf{L}}_V \in \mathbb{C}^{m_v \times n}$ is a binary matrix, whose entries, for each row, are equal to 1 only in correspondence of the index of the node where the voltage measurement is placed, otherwise are zeros. To better understand, the voltage measurement at the j-th bus of the network will be included in the matrix $\overline{\mathbf{L}}_V$ (row k if it is the kth measurement) with the row:

$$\overline{\mathbf{L}}_{V,k} = \begin{matrix} & & j & & \\ [0 & \ldots & 1 & \ldots & 0] \end{matrix} \tag{3.15}$$

Instead, each row of the sub-matrix related to the branch current measure-

ments, $\overline{\mathbf{L}}_I \in \mathbb{C}^{m_i \times n}$, has, as non-zero elements, the longitudinal component of the admittance of the corresponding monitored branch, placed in correspondence of the indexes of the starting and receiving nodes of the branch; while the other entries are set to zero. In addition, since the branch model should also include the shunt susceptances, the shunt admittance is added to the vector entry associated to the starting node. For example, for a generic measurement of the branch current flowing from bus i to bus j, there are two non-zero elements of the corresponding l-th row of $\overline{\mathbf{L}}_I$. They are given by the branch admittance $y_{i,j}$ summed with the shunt admittance $y_{i,j\,sh}$ and by $-y_{i,j}$ in the positions i and j of the vector, respectively. The l-th row is thus:

$$\overline{\mathbf{L}}_{I,l} = \begin{bmatrix} 0 & \dots & \overset{i}{y_{i,j} + y_{i\,sh}} & 0 & \overset{j}{-y_{i,j}} & \dots & 0 \end{bmatrix} \tag{3.16}$$

Now that the meaning of the matrices in (3.13) is clear, the system can be expressed in terms of real and imaginary parts, as done in the previous section.

$$\begin{bmatrix} \Delta\mathbf{V}^r \\ \Delta\mathbf{V}^x \\ \Delta\mathbf{I}_{br}^r \\ \Delta\mathbf{I}_{br}^x \end{bmatrix} = \begin{bmatrix} \mathbf{A}_V^r & -\mathbf{A}_V^x \\ \mathbf{A}_V^x & \mathbf{A}_V^r \\ \mathbf{A}_I^r & -\mathbf{A}_I^x \\ \mathbf{A}_I^x & \mathbf{A}_I^r \end{bmatrix} \begin{bmatrix} \Delta\mathbf{J}^r \\ \Delta\mathbf{J}^x \end{bmatrix} + \begin{bmatrix} \mathbf{e}^r \\ \mathbf{e}^x \end{bmatrix} \tag{3.17}$$

$$\Delta\mathbf{Y}^{rx} = \mathbf{A}^{rx}\Delta\mathbf{J}^{rx} + \mathbf{e}^{rx}$$

Vector $\Delta\mathbf{Y}^{rx}$ in (3.17) is the vector representing the variation of the measurements between pre- and during-fault scenarios, obtained by concatenating both $\Delta\mathbf{V}^{rx}$ and $\Delta\mathbf{I}_{br}^{rx}$ vectors. Also in this case, the representation in (3.17) allows to recover the non-zero components of the state vector, $\Delta\mathbf{J}^{rx}$, by applying the BOMP algorithm, see Algorithm 2 in Section 1.6.3, considering blocks of size 2.

3.5.1 Tests and Results

The performance of the proposed solution are tested in the following, by considering the test grid already presented in Section 3.3.1, simulated on RTDS. Also in this case, the algorithm will be tested by considering a realistic uncertainty scenario.

The accuracy classes for measurements obtained by means of the current transformers (CTs), as described in the corresponding standard [96], are reported in table 3.36 and table 3.37 for measurement and protection purposes respectively.

Table 3.36: Accuracy requirements for measurement purpose current transformers [96]

Transformer purpose	Accuracy Class	Ratio error [%]				Phase displacement [± crad]			
		at current (% of rated)				at current (% of rated)			
		5	20	100	120	5	20	100	120
M	0.1	0.4	0.2	0.1	0.1	0.45	0.24	0.15	0.15
M	0.2	0.75	0.35	0.2	0.2	0.9	0.45	0.3	0.3
M	0.5	1.5	0.75	0.5	0.5	2.7	1.35	0.9	0.9
M	1	3.0	1.5	1.0	1.0	5.4	2.7	1.8	1.8

Table 3.37: Accuracy requirements for protection purpose current transformers [96]

Transformer purpose	Accuracy Class	Ratio error [%]	Phase displacement [± crad]
Protection	5P	1	1.8
	10P	3	not specified

With reference to CTs for measurement purpose, the accuracy for both ratio error and phase displacement are reported, for each accuracy class, with reference to the effective measured current, considered as a percentage of the nominal current. Instead, the maximum errors for protection purpose CTs are defined only at the rated with rated burden connected. In particular, in the following tests, the considered accuracy classes are chosen based on the ones of the most installed in distribution systems: 0.5 and $5P$ for measurement and protection purpose respectively.

With regard to the measurements provided by the PMUs, the performance in case of current measurements are the same presented in table 3.2, for the voltage measurements. Thus, the uncertainty scenario here considered is briefly summarized in the following table:

Table 3.38: Uncertainty Scenarios

	Pre-fault	During fault
CT class	0.5	5P
VT class	0.5	3P
PMU TVE_{max}	1%	3%

Moreover, since the impact of the branch current measurements on the fault location is of interest in this section, different measurement placement configuration will be considered. Starting from a case study in which only voltage measurements are available, the effects of introducing a new current measurement

in the fault location analysis will be compared with the effects corresponding to the inclusion of a new voltage measurements.

Table 3.39: Impact of branch current - Measurement placement test cases

Test case	Voltage meas.	Current meas.
Case 1	V_1, V_7	-
Case 2	V_1, V_4, V_7	-
Case 3	V_1, V_7	$I_{br_{12}}$
Case 4	V_1, V_7	$I_{br_{45}}$
Case 5	V_1, V_7	$I_{br_{12}}$, $I_{br_{45}}$
Case 6	V_1	$I_{br_{12}}$, $I_{br_{45}}$, $I_{br_{67}}$

Case 1 and Case 2 have already been presented in Section 3.3.1, with reference to the comparison between different uncertainty scenarios (respectively, Case 4 and Case 3). Now, the corresponding results with reference to the realistic uncertainty scenario, $\mathbb{S} + \mathbb{D}$, are reported again in the following, respectively in table 3.40 and table 3.41 for sake of clarity. Case 1 is considered here as a starting point, in which it is not possible to rely on the identification provided by the proposed algorithm due to the inaccurate detections, especially for faults occurring on nodes 4, 5, and 6.

Table 3.40: Case 1 with measurement uncertainties $\mathbb{S} + \mathbb{D}$

Detected node	Fault node					
	2 [%]	3 [%]	4 [%]	5 [%]	6 [%]	7 [%]
1	2,96	0	0	0	0	0
2	**87,93**	16,72	1,41	0,14	0	0
3	9,11	**59,35**	26,80	8,88	2,91	1,07
4	0	21,27	**38,32**	26,50	15,59	8,86
5	0	2,56	21,10	**26,00**	21,35	15,98
6	0	0,10	7,97	17,19	**18,40**	16,71
7	0	0	4,40	21,29	41,75	**57,38**

The first approach to improve the accuracy of the fault location could consists in adding a voltage measurement in the middle of the network, bus 4 in this case. The effect of the new measurement is particularly evident when nodes 5 or 6 are considered as fault, where the correct identifications are almost twice those of Case 1. Despite this, still the detection improvement due to the new voltage measurement is not sufficient to consider the algorithm enough accurate. In fact, there is only one case in which the correct detection occurs more the 90% of the times, when fault involves node 2.

Table 3.41: Case 2 with measurement uncertainties

Detected	Fault node					
node	2 [%]	3 [%]	4 [%]	5 [%]	6 [%]	7 [%]
1	1,48	0	0	0	0	0
2	**90,79**	14,32	0,77	0,56	0,28	0,08
3	7,73	**60,90**	25,34	9,56	1,91	0,31
4	0	20,99	**57,51**	15,62	1,75	0,16
5	0	3,79	16,18	**48,95**	25,45	7,22
6	0	0	0,20	22,54	**39,36**	26,26
7	0	0	0	2,77	31,25	**65,97**

The second solution here analyzed, Case 3, is to consider the addition of a branch current measurement, instead of the voltage one. In table 3.42 the detection rates obtained by considering the measurement of the branch current flowing in the first branch, $I_{br_{12}}$, are presented. This solution is particularly interesting, since it does not require the installation of a new measurement point in the network. In fact, the current injected from the substation to the system can be measured by using another channel of the PMU already installed in node 1, with a consequent saving in terms of costs.

The impact of the new measurement is evident, not only with reference to Case 1 but also in comparison with Case 2. The improvement in the performance is higher than the one obtained by adding the voltage measurement V_4, for each fault node. Moreover, it is interesting to see that also the wrong identifications are less spread along the network.

Table 3.42: Case 3 with measurement uncertainties

Detected	Fault node					
node	2 [%]	3 [%]	4 [%]	5 [%]	6 [%]	7 [%]
1	0	0	0	0	0	0
2	**99,28**	6,61	0	0	0	0
3	0,72	**85,90**	15,95	0,47	0	0
4	0	7,49	**66,59**	23,21	2,99	0,21
5	0	0	17,04	**50,95**	26,40	7,64
6	0	0	0,42	21,78	**39,40**	26,13
7	0	0	0	3,59	31,21	**66,02**

In order to further study the improvements obtainable by measurements current included in the fault location analysis, in Case 4 the measurement configuration with a branch current measured in the middle of the network, $I_{br_{45}}$, is tested.

The results for this test case, presented in table 3.43, are of particular interest. Over the expected increase of the performance for the detection of faults on nodes 3 and 4, a subdivision of the network can be observed. With reference

to node 4, where the new current measurement is introduced, two sections are denoted: the upstream network, from node 1 to node 4, and the downstream one, which includes the nodes between node 5 and node 7.

Table 3.43: Case 4 with measurement uncertainties

Detected node	Fault node					
	2 [%]	3 [%]	4 [%]	5 [%]	6 [%]	7 [%]
1	2,96	0	0	0	0	0
2	**87,93**	16,72	1,41	0	0	0
3	9,11	**59,35**	26,80	0	0	0
4	0	23,93	**71,79**	0	0	0
5	0	0	0	**74,59**	29,66	7,97
6	0	0	0	21,95	**38,85**	26,14
7	0	0	0	3,46	31,49	**65,89**

The results show how, when a fault occurs on a node belonging to the upstream network, the detection is always limited to the nodes belonging to that subsection. Same considerations hold when the fault involves one node between node 5, or node 7. This subdivision of the grid can be very useful, since it allows confining the location of the fault in a certain area, based only on the measurement placement. Such classification, and thus the delimitation of the fault location to a specific area, was not possible when only voltage measurements were considered (table 3.40 and table 3.41).

Consequently, by considering multiple current measurements, it is possible to create multiple areas where to delimit the inspection, thus increasing the resolution in terms of nodes, since many areas mean less nodes per area. Based on this principle, in Case 5, two current measurements are considered in addition to the measurements of the voltages V_1 and V_7: $I_{br_{12}}$ and $I_{br_{45}}$. With this measurement configuration, considering what was shown in table 3.43, the network should be divided in three areas: the first one including only the substation, the second one including nodes 2 to 4, and the third one from node 5 to node 7. These assumptions are confirmed by the detection results reported in table 3.44, where the first column indicates the different areas.

Table 3.44: Case 5 with measurement uncertainties

	Detected node	Fault node					
		2 [%]	3 [%]	4 [%]	5 [%]	6 [%]	7 [%]
Area 1	1	0	0	0	0	0	0
	2	**99,28**	6,61	0	0	0	0
Area 2	3	0,72	**85,90**	15,95	0	0	0
	4	0	7,49	**84,05**	0	0	0
	5	0	0	0	**80,63**	25,07	3,25
Area 3	6	0	0	0	18,74	**49,45**	25,84
	7	0	0	0	0,63	25,48	**70,91**

The first area, the one including only the substation (node 1), is correctly never labelled as faulty, while, in the other areas, the percentages of correct identification increase for all nodes, and the erroneous detections are limited to the nodes belonging to the area.

Same considerations hold when different POWs are considered, as shown in figure 3.8. In the figure, the detection results for Case 5 are reported with reference to POW = 30°, 60°, and 90°. The percentages of detection are presented as bars, with different colours, according to the associated POW (blue, red and yellow respectively for POW = 30°, 60°, and 90°). Each area has been highlighted by vertical red lines, delimiting the nodes of the network. It can be seen that neither the percentage of detections, neither the subdivision in areas, are affected by the different POWs.
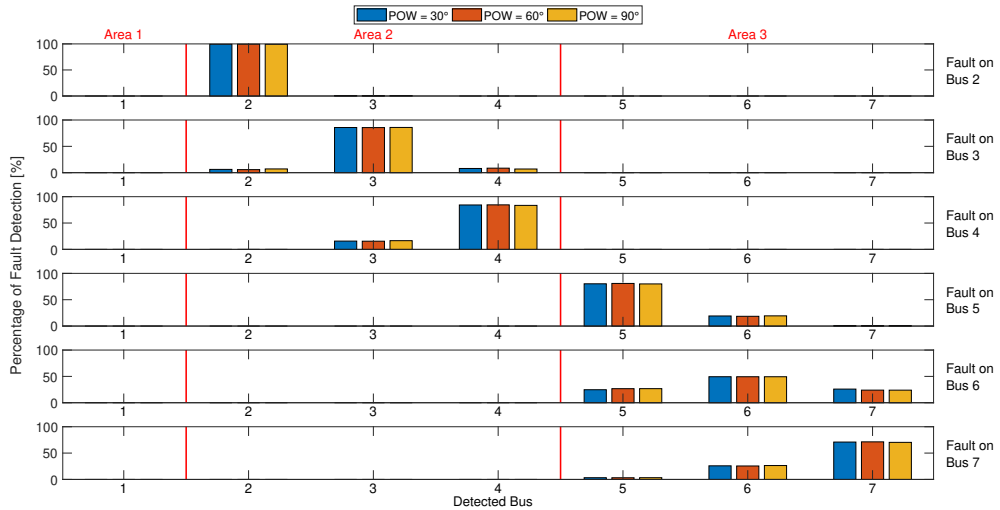
Figure 3.8: Case 5, percentage of fault detection for different POWs.

The fact that node 1 is never detected as fault could seem obvious, since no fault occurred on it, but it is worth noting that the same principle (having an area composed by a single node) can be applied to monitor a node which is critical and does not allow any erroneous fault detection.

Let us say, for example, that the load connected to node 7 is of particular interest since the faults occurring in that node are particularly critical. Thus, in Case 6, by substituting the voltage measurement V_7 with the current measurement flowing into the last branch, $I_{br_{67}}$, a single node area, containing only node 7, is obtained. Consequently, four areas have been created, as reported in the first column of table 3.45.

Area 1, and thus node 1, is never labelled as faulty, while in area 4 the identification of bus 7 as location of the fault is perfect (100% of the trials).

In the other areas, area 2 and 3, the detection is always limited to the nodes belonging to the area and the percentages of correct detection for each node increase, with reference to the previous cases.

Table 3.45: Case 6 with measurement uncertainties

	Detected node	**Fault node**					
		2 [%]	3 [%]	4 [%]	5 [%]	6 [%]	7 [%]
Area 1	*1*	0	0	0	0	0	0
Area 2	*2*	**99,87**	1,68	0	0	0	0
	3	0,13	**93,66**	8,12	0	0	0
	4	0	4,66	**91,88**	0	0	0
Area 3	*5*	0	0	0	**80,34**	42,19	0
	6	0	0	0	19,66	**57,81**	0
Area 4	*7*	0	0	0	0	0	**100**

As shown in the previous sections, the lack of measurements, together with the uncertainties related to the real signals, decrease the performance of any algorithm.

The additional information related to the area where the fault occurred can be then used by the DSO. In fact, even if there has been an unclear identification, the DSO can use the information on the area where the fault is located: to lead the crew which should manage to extinguish the fault, by reducing the area to be investigated, and to re-establish the power supply in the areas not affected by the fault.

Furthermore, it is worth mentioning that the three phase-to-ground faults are always characterized by higher percentages of correct detection, thanks to larger non-zero entries of the state vector to be recovered. As example, in figure 3.9 the identification performance of three phase-to-ground faults, with reference to the measurement configuration of Case 3, is presented for different POWs (30°, 60°and 90°). The bars, indicating the percentage of trials corresponding to a correct detection, highlight that the detection is almost perfect, for every considered POW (blue bar for POW = 30°, red bar for POW = 60°and yellow bar for POW = 90°). Moreover, it is worth mentioning that in this configuration only three measurements are considered: V_1, V_7, and $I_{br_{12}}$, but it has to be noticed that the identification of three phase-to-ground faults is always almost perfect, also when the other measurement configurations are taken into account.
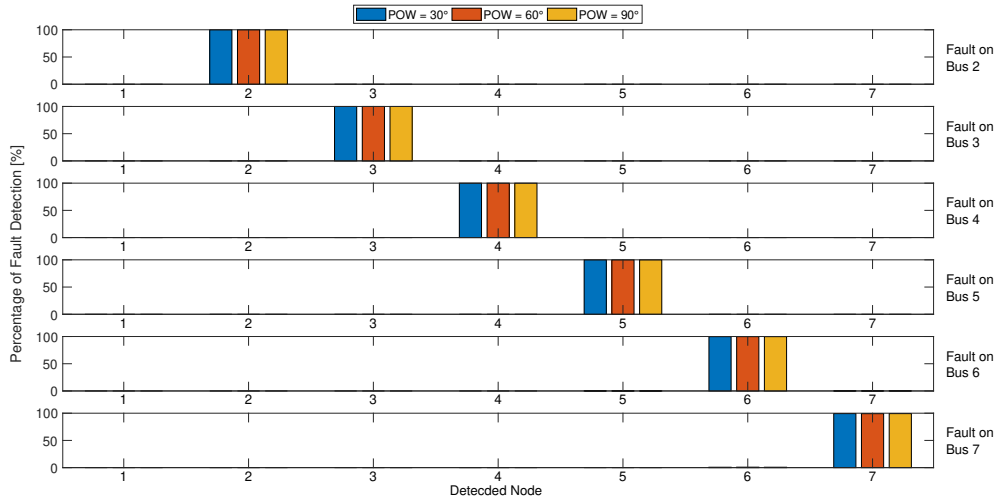
Figure 3.9: Case 3, considering 3 phase-to-ground faults, percentage of fault detection for different POWs.

3.6 Conclusions

In this chapter, the problem of locating the fault in a distribution network has been discussed. Also in this case, the few measurements commonly available in the network are not sufficient to apply standard analysis techniques, especially because most of them require redundancy of information. Moreover, during the preliminary study of the problem, the bibliographic research underlined how most of the related papers presented in literature were not properly considering the impact of measurement uncertainties. Thus, a compressive sensing based fault location technique has been proposed, and tested, in a realistic uncertainty scenario, appropriately distinguishing the performance of the measurement chain between the pre-fault, that is in steady-state operating conditions, and the during fault, when signals are highly dynamic.

The obtained results underline the impact that the measurement chain has on the performance of the algorithm. Thus, in order to improve the performance of the fault location algorithms, additional information regarding the branch current measurements have been considered. Nowadays, new generation transformers allow to overcome the problems related to the saturation of the current transformers, and here it has been shown that branch current measurements play an important role in the proposed fault location algorithm. Thanks to these additional measurements, it is possible to define "areas" where the fault is included.

Conclusions

The upcoming Smart Grid scenario will be characterized by strictly requirements in terms of reliability and efficiency of the power supply. This will require a high empowerment in the management of the distribution, and transmission, networks by the system operators.

The improvement of the monitoring infrastructure, in parallel to the development of new management policies, is strictly needed, to fully exploit the capabilities of the Smart Grids. Thus, in this transition period, it is mandatory to find algorithms and solutions aimed at supporting system operators, while managing the networks. In this thesis, the focus has been on the analysis of Compressive Sensing-based solutions for the monitoring and management of the distribution grids. In particular, methodologies for detecting the main harmonic polluting sources, and for identifying the location of faults occurring in distribution systems have been presented.

This powerful mathematical technique allows to identify, and estimate, the sparse components of the vector state when the model of the problem is characterized by measurements in number fewer than the state variables. Such scenario is very common in the analysis of modern distribution systems, and the problems here considered, the identification of the prevailing harmonic sources and the fault location, are only two of the problems for which this technique is suitable. Due to the low computational burden, and the ease of implementation, the Orthogonal Matching Pursuit has been chosen as starting point to develop algorithms for the analysis of the distribution networks. For the identification of the main harmonic sources and fault location, the proposed solutions have demonstrated the capability of finding a solution to the considered problem. Moreover, the proposed solutions have been tested under realistic uncertainty scenarios, to properly validate the algorithms.

The algorithms for the identification of the main harmonic sources proved to be robust with respect to the measurement uncertainties. The BOMP-based algorithm has proved to be suitable in main harmonic source detection, when there is the need to perform analysis on a specific harmonic order. Nevertheless,

it is known that the harmonic sources can be commonly polluting for multiple harmonic orders, and the proposed global detector, LBOMP, has been proved to be particularly suitable for general analysis, since it allows to consider multiple harmonic orders simultaneously. This technique is in fact capable to detect the polluting sources by providing an estimation of the polluting currents, for each considered scenario.

Fault location analysis is more critical, due to the higher uncertainties in measuring the dynamic signals involved during the fault. Contrarily to what commonly presented in literature, in this thesis the proper uncertainty scenarios have been considered and the difficulties in detecting the fault have been underlined. Then, considering the possibility of using the most advanced measurement chain, composed of low power transformers and PMUs, the impact of the branch current measurements on the fault location algorithm has been presented. The obtained results have underlined how, with only few measurement devices installed, the branch current measurements allow, as minimum result, to detect sections of the network, areas, which include multiple nodes, including the fault. In the absence of a monitoring system planned specifically for detection purpose, despite the possibility of having not certain identification of the faulty bus, the identification of a fault inside an area has been proved to be always correct. This is a useful information that the system operator could use to conduct further analysis.

Further studies could focus on the appropriate modellization of the impact of the measurement uncertainties, starting from the analysis of the measurement matrix so that the inevitable degradation of the accuracy performance of the measurement chain in dynamic conditions could be better faced by monitoring algorithms.

References

[1] H. Nyquist, "Certain topics in telegraph transmission theory," *Transactions of the American Institute of Electrical Engineers*, vol. 47, no. 2, pp. 617–644, April 1928.

[2] C. E. Shannon, "Communication in the presence of noise," *Proceedings of the IRE*, vol. 37, no. 1, pp. 10–21, Jan 1949.

[3] H. Cheng, *Sparse Representation, Modeling and Learning in Visual Recognition: Theory, Algorithms and Applications.* Springer Publishing Company, Incorporated, 2015.

[4] G. K. Yonina C. Eldar, *Compressed Sensing: Theory and Applications.* Cambridge University Press, 2012.

[5] D. Needell and J. Tropp, "Cosamp: Iterative signal recovery from incomplete and inaccurate samples," *Applied and Computational Harmonic Analysis*, vol. 26, no. 3, pp. 301 – 321, 2009. [Online]. Available: http://www.sciencedirect.com/science/article/pii/S1063520308000638

[6] A. Cohen, W. Dahmen, and R. DeVore, "Compressed sensing and best k-term approximation," *American Mathematical Society*, vol. 22, pp. 211–231, 01 2009.

[7] Y. C. Eldar, *Sampling Theory: Beyond Bandlimited Systems.* Cambridge University Press, 2015.

[8] D. L. Donoho and M. Elad, "Optimally sparse representation in general (nonorthogonal) dictionaries via l1 minimization," *Proc Natl Acad Sci*, pp. 100(5):2197–2202, 2003.

[9] H.-N. Lee, "Introduction to compressed sensing," *Lecture notes*, Spring Semester, 2011.

[10] S. Geršgorin, "Über dieabgrenzung der eigenwerte einer matrix," *Izv. Akad Nauk SSSR Ser Fiz.-Mat*, p. 6:749–754, 1931.

[11] E. Michael, *Sparse and Redundant Representations: From Theory to Applications in Signal and Image Processing.* New York: Springer, 2010.

[12] E. J. Candes and T. Tao, "Decoding by linear programming," *IEEE Transactions on Information Theory*, vol. 51, no. 12, pp. 4203–4215, Dec 2005.

[13] V. M. Patel and R. Chellappa, *Sparse Representations and Compressive Sensing for Imaging and Vision*, ser. SpringerBriefs in Electrical and Computer Engineering. New York: Springer-Verlag, 2013. [Online]. Available: https://www.springer.com/gp/book/9781461463801

[14] M. A. Davenport, "Random observations on random observations: Sparse signal acquisition and processing," Ph.D. dissertation, Rice University, Houston, Texas, 8 2010.

[15] E. J. Candès and Y. Plan, "A probabilistic and ripless theory of compressed sensing," *CoRR*, vol. abs/1011.3854, 2010. [Online]. Available: http://arxiv.org/abs/1011.3854

[16] A. Garnaev and E. Gluskin, "On widths of the euclidean ball." *Dokl An SSSR*, vol. 277, no. 5, pp. 1048–1052., 1984.

[17] W. Johnson and J. Lindenstrauss, "Extensions of lipschitz maps into a hilbert space," *Contemporary Mathematics*, vol. 26, pp. 189–206, 01 1984.

[18] F. Krahmer and R. Ward, "New and improved johnson-lindenstrauss embeddings via the restricted isometry property," *CoRR*, vol. abs/1009.0744, 2011. [Online]. Available: http://arxiv.org/abs/1009.0744

[19] H. Rauhut, "Compressive sensing and structured random matrices," *Theoretical Foundations and Numerical Methods for Sparse Recovery*, vol. 9, pp. 1–92, 01 2010.

[20] E. J. Candes and T. Tao, "Decoding by linear programming," *IEEE Transactions on Information Theory*, vol. 51, no. 12, pp. 4203–4215, Dec. 2005.

[21] E. J. Candès, J. K. Romberg, and T. Tao, "Stable signal recovery from incomplete and inaccurate measurements," *Communications on Pure and Applied Mathematics*, vol. 59, no. 8, pp. 1207–1223, 8 2006. [Online]. Available: https://doi.org/10.1002/cpa.20124

[22] E. J. Candès, "The restricted isometry property and its implications for compressed sensing," *Comptes Rendus Mathematique*, vol. 346, no. 9, pp. 589 – 592, 2008. [Online]. Available: http://www.sciencedirect.com/science/article/pii/S1631073X08000964

[23] H. Cheng, Z. Liu, L. Yang, and X. Chen, "Sparse representation and learning in visual recognition: Theory and applications," *Signal Processing*, vol. 93, no. 6, pp. 1408 – 1425, 2013, special issue on Machine Learning in Intelligent Image Processing. [Online]. Available: http://www.sciencedirect.com/science/article/pii/S0165168412003313

[24] S. Kim, K. Koh, M. Lustig, S. Boyd, and D. Gorinevsky, "An interior-point method for large-scaleℓ_1-regularized least squares," *IEEE Journal of Selected Topics in Signal Processing*, vol. 1, no. 4, pp. 606–617, Dec 2007.

[25] M. A. T. Figueiredo, R. D. Nowak, and S. J. Wright, "Gradient projection for sparse reconstruction: Application to compressed sensing and other inverse problems," *IEEE Journal of Selected Topics in Signal Processing*, vol. 1, no. 4, pp. 586–597, Dec 2007.

[26] I. Daubechies, M. Defrise, and C. De Mol, "An iterative thresholding algorithm for linear inverse problems with a sparsity constraint," *Communications on Pure and Applied Mathematics*, vol. 57, no. 11, pp. 1413–1457, 2004. [Online]. Available: https://onlinelibrary.wiley.com/doi/abs/10.1002/cpa.20042

[27] S. Chen, D. Donoho, and M. Saunders, "Atomic decomposition by basis pursuit," *SIAM Journal on Scientific Computing*, vol. 20, no. 1, pp. 33–61, 1998. [Online]. Available: https://doi.org/10.1137/S1064827596304010

[28] M. Iwen, "Compressed sensing with sparse binary matrices: Instance optimal error guarantees in near-optimal time," *Journal of Complexity*, vol. 30, no. 1, pp. 1 – 15, 2014. [Online]. Available: http://www.sciencedirect.com/science/article/pii/S0885064X13000642

[29] S. Jafarpour, W. Xu, B. Hassibi, and R. Calderbank, "Efficient and robust compressed sensing using optimized expander graphs," *IEEE Transactions on Information Theory*, vol. 55, no. 9, pp. 4299–4308, Sep. 2009.

[30] A. C. Gilbert, M. J. Strauss, J. A. Tropp, and R. Vershynin, "One sketch for all: Fast algorithms for compressed sensing," in *Proceedings of the Thirty-ninth Annual ACM Symposium on Theory of Computing*, ser. STOC '07. New York, NY, USA: ACM, 2007, pp. 237–246. [Online]. Available: http://doi.acm.org/10.1145/1250790.1250824

[31] M. Iwen, "Combinatorial sublinear-time fourier algorithms," *Foundations of Computational Mathematics*, vol. 10, pp. 303–338, 06 2010.

[32] S.-H. Cha, "Comprehensive survey on distance/similarity measures between probability density functions," *Int. J. Math. Model. Meth. Appl. Sci.*, vol. 1, 01 2007.

[33] M. A. Davenport and M. B. Wakin, "Analysis of orthogonal matching pursuit using the restricted isometry property," *IEEE Transactions on Information Theory*, vol. 56, no. 9, pp. 4395–4401, Sep. 2010.

[34] J. A. Tropp, "Greed is good: algorithmic results for sparse approximation," *IEEE Transactions on Information Theory*, vol. 50, no. 10, pp. 2231–2242, Oct 2004.

[35] D. L. Donoho, "For most large underdetermined systems of equations, the minimal l-norm near-solution approximates the sparsest near-solution," *Communications on Pure and Applied Mathematics*, vol. 59, no. 7, pp. 907–934, 2006. [Online]. Available: https://onlinelibrary.wiley.com/doi/abs/10.1002/cpa.20131

[36] J. Wang, "Support recovery with orthogonal matching pursuit in the presence of noise," *IEEE Transactions on Signal Processing*, vol. 63, no. 21, pp. 5868–5877, Nov 2015.

[37] T. T. Cai and L. Wang, "Orthogonal matching pursuit for sparse signal recovery with noise," *IEEE Transactions on Information Theory*, vol. 57, no. 7, pp. 4680–4688, July 2011.

[38] D. L. Donoho, M. Elad, and V. N. Temlyakov, "Stable recovery of sparse overcomplete representations in the presence of noise," *IEEE Transactions on Information Theory*, vol. 52, no. 1, pp. 6–18, Jan 2006.

[39] T. Blumensath and M. E. Davies, "Gradient pursuits," *IEEE Transactions on Signal Processing*, vol. 56, no. 6, pp. 2370–2382, June 2008.

[40] B. Mailhe, R. Gribonval, F. Bimbot, and P. Vandergheynst, "A low complexity orthogonal matching pursuit for sparse signal approximation with shift-invariant dictionaries," in *2009 IEEE International Conference on Acoustics, Speech and Signal Processing*, April 2009, pp. 3445–3448.

[41] G. Golub, C. Van Loan, C. Van Loan, and P. Van Loan, *Matrix Computations*, ser. Johns Hopkins Studies in the Mathematical Sciences. Johns Hopkins University Press, 1996. [Online]. Available: https://books.google.it/books?id=mlOa7wPX6OYC

[42] H. Crowder and P. Wolfe, "Linear convergence of the conjugate gradient method," *IBM Journal of Research and Development*, vol. 16, no. 4, pp. 431–433, July 1972.

[43] D. L. Donoho, Y. Tsaig, I. Drori, and J. Starck, "Sparse solution of under-determined systems of linear equations by stagewise orthogonal matching pursuit," *IEEE Transactions on Information Theory*, vol. 58, no. 2, pp. 1094–1121, Feb 2012.

[44] T. Blumensath and M. E. Davies, "Stagewise weak gradient pursuits," *IEEE Transactions on Signal Processing*, vol. 57, no. 11, pp. 4333–4346, Nov 2009.

[45] K. Schnass and P. Vandergheynst, "Average performance analysis for thresholding," *IEEE Signal Processing Letters*, vol. 14, no. 11, pp. 828–831, Nov 2007.

[46] Y. C. Eldar, P. Kuppinger, and H. Bolcskei, "Block-sparse signals: Uncertainty relations and efficient recovery," *IEEE Transactions on Signal Processing*, vol. 58, no. 6, pp. 3042–3054, June 2010.

[47] Z. Ben-Haim and Y. C. Eldar, "Near-oracle performance of greedy block-sparse estimation techniques from noisy measurements," *IEEE Journal of Selected Topics in Signal Processing*, vol. 5, no. 5, pp. 1032–1047, Sep. 2011.

[48] M. H. J. Bollen, "What is power quality?" *Electric Power Systems Research*, vol. 66, no. 1, pp. 5–14, Jul. 2003.

[49] *Electromagnetic compatibility (EMC) – Part 3-6: Limits – Assessment of emission limits for the connection of distorting installations to MV, HV and EHV power systems*, IEC IEC TR 61000-3-6:2008, Feb. 2008.

[50] E. J. Davis, A. E. Emanuel, and D. J. Pileggi, "Evaluation of single-point measurements method for harmonic pollution cost allocation," *IEEE Transactions on Power Delivery*, vol. 15, no. 1, pp. 14–18, Jan 2000.

[51] C. F. M. Almeida and N. Kagan, "Harmonic state estimation through optimal monitoring systems," *IEEE Transactions on Smart Grid*, vol. 4, no. 1, pp. 467–478, March 2013.

[52] C. Rakpenthai, S. Uatrongjit, N. R. Watson, and S. Premrudeepreechacharn, "On harmonic state estimation of power system with uncertain network parameters," *IEEE Transactions on Power Systems*, vol. 28, no. 4, pp. 4829–4838, Nov 2013.

[53] A. Farzanehrafat and N. R. Watson, "Power quality state estimator for smart distribution grids," *IEEE Transactions on Power Systems*, vol. 28, no. 3, pp. 2183–2191, Aug 2013.

[54] K. K. C. Yu, N. R. Watson, and J. Arrillaga, "Error analysis in static harmonic state estimation: a statistical approach," *IEEE Transactions on Power Delivery*, vol. 20, no. 2, pp. 1045–1050, April 2005.

[55] G. D'Antona, C. Muscas, and S. Sulis, "Localization of Nonlinear Loads in Electric Systems Through Harmonic Source Estimation," *IEEE Transactions on Instrumentation and Measurement*, vol. 60, no. 10, pp. 3423–3430, Oct. 2011.

[56] G. D'Antona, C. Muscas, P. A. Pegoraro, and S. Sulis, "Harmonic Source Estimation in Distribution Systems," *IEEE Transactions on Instrumentation and Measurement*, vol. 60, no. 10, pp. 3351–3359, Oct. 2011.

[57] D. Carta, C. Muscas, P. A. Pegoraro, and S. Sulis, "Harmonics Detector in Distribution Systems based on Compressive Sensing," in *2017 IEEE International Workshop on Applied Measurements for Power Systems (AMPS)*, Sep. 2017, pp. 1–5.

[58] D. Carta, C. Muscas, P. A. Pegoraro, and S. Sulis, "Identification and estimation of harmonic sources based on compressive sensing," *IEEE Transactions on Instrumentation and Measurement*, vol. 68, no. 1, pp. 95–104, Jan 2019.

[59] *Electromagnetic compatibility (EMC) - Part 4-7: Testing and measurement techniques - General guide on harmonics and interharmonics measurements and instrumentation, for power supply systems and equipment connected thereto*, IEC IEC 61000-4-7:2002+AMD1:2008 CSV, Oct. 2009.

[60] JCGM, "Evaluation of data - guide to the expression of uncertainty in measurement," *JCGM 100:2008*, Sep. 2008.

[61] N. Locci, C. Muscas, and S. Sulis, "Experimental comparison of mv voltage transducers for power quality applications," in *2009 IEEE Instrumentation and Measurement Technology Conference*, May 2009, pp. 92–97.

[62] W. H. Kersting, "Radial distribution test feeders," *IEEE Transactions on Power Systems*, vol. 6, no. 3, pp. 975–985, Aug. 1991.

[63] T. Gonen, *Electric power distribution engineering*. CRC press, 2015.

[64] S. Shilpa G, H. Mokhlis, and H. Illias, "Fault location and detection techniques in power distribution systems with distributed generation: A review," *Renewable and Sustainable Energy Reviews*, vol. 74, pp. 949–958, 07 2017.

[65] A. Bahmanyar, S. Jamali, A. Estebsari, and E. Bompard, "A comparison framework for distribution system outage and fault location methods," *Electric Power Systems Research*, vol. 145, pp. 19–34, Apr. 2017. [Online]. Available: http://www.sciencedirect.com/science/article/pii/S0378779616305302

[66] W. H. Kersting, *Distribution system modeling and analysis*. CRC press, 2006.

[67] R. Krishnathevar and E. E. Ngu, "Generalized impedance-based fault location for distribution systems," *IEEE Transactions on Power Delivery*, vol. 27, no. 1, pp. 449–451, Jan 2012.

[68] F. C. L. Trindade, W. Freitas, and J. C. M. Vieira, "Fault location in distribution systems based on smart feeder meters," *IEEE Transactions on Power Delivery*, vol. 29, no. 1, pp. 251–260, Feb 2014.

[69] A. Borghetti, M. Bosetti, C. A. Nucci, M. Paolone, and A. Abur, "Integrated use of time-frequency wavelet decompositions for fault location in distribution networks: Theory and experimental validation," *IEEE J PWRD*, vol. 25, no. 4, pp. 3139–3146, Oct 2010.

[70] W. C. Santos, F. V. Lopes, N. S. D. Brito, and B. A. Souza, "High-impedance fault identification on distribution networks," *IEEE J PWRD*, vol. 32, no. 1, pp. 23–32, Feb 2017.

[71] Z. Q. Bo, G. Weller, and M. A. Redfern, "Accurate fault location technique for distribution system using fault-generated high-frequency transient voltage signals," *IEE Proceedings - Generation, Transmission and Distribution*, vol. 146, no. 1, pp. 73–79, Jan 1999.

[72] M. Majidi, M. Etezadi-Amoli, and M. Sami Fadali, "A novel method for single and simultaneous fault location in distribution networks," *IEEE Transactions on Power Systems*, vol. 30, no. 6, pp. 3368–3376, Nov 2015.

[73] D. Thukaram, H. P. Khincha, and H. P. Vijaynarasimha, "Artificial neural network and support vector machine approach for locating faults in radial distribution systems," *IEEE Transactions on Power Delivery*, vol. 20, no. 2, pp. 710–721, April 2005.

[74] M. Majidi, A. Arabali, and M. Etezadi-Amoli, "Fault Location in Distribution Networks by Compressive Sensing," *IEEE Transactions on Power Delivery*, vol. 30, no. 4, pp. 1761–1769, Aug. 2015.

[75] M. Majidi and M. Etezadi-Amoli, "A new fault location technique in smart distribution networks using synchronized/nonsynchronized measurements," *IEEE Transactions on Power Delivery*, vol. 33, no. 3, pp. 1358–1368, Jun. 2018.

[76] D. Carta, P. A. Pegoraro, and S. Sulis, "Impact of measurement accuracy on fault detection obtained with compressive sensing," in *2018 IEEE 9th International Workshop on Applied Measurements for Power Systems (AMPS)*, Sept 2018, pp. 1–5.

[77] F. Yang, J. Tan, J. Song, and Z. Han, "Block-wise compressive sensing based multiple line outage detection for smart grid," *IEEE Access*, vol. 6, pp. 50 984–50 993, 2018.

[78] M. Saha, J. Izykowski, and E. Rosolowski, *Fault Location on Power Networks*, 01 2010, vol. 48.

[79] E. B. Makram, M. A. Bou-Rabee, and A. A. Girgis, "Three-phase modeling of unbalanced distribution systems during open conductors and/or shunt fault conditions using the bus impedance matrix," *Electric Power Systems Research*, vol. 13, no. 3, pp. 173–183, Dec. 1987. [Online]. Available: http://www.sciencedirect.com/science/article/pii/0378779687900022

[80] IEC, "Instrument transformers - Part 3: Additional requirements for inductive voltage transformers," *Standard IEC 61869-3*, 2011.

[81] S. Jamali, A. Bahmanyar, and E. Bompard, "Fault location method for distribution networks using smart meters," *Measurement*, vol. 102, pp. 150 – 157, 2017. [Online]. Available: http://www.sciencedirect.com/science/article/pii/S0263224117301033

[82] F. C. L. Trindade, W. Freitas, and J. C. M. Vieira, "Fault location in distribution systems based on smart feeder meters," *IEEE Transactions on Power Delivery*, vol. 29, no. 1, pp. 251–260, Feb 2014.

[83] A. Angioni, G. Lipari, M. Pau, F. Ponci, and A. Monti, "A low cost pmu to monitor distribution grids," in *2017 IEEE International Workshop on Applied Measurements for Power Systems (AMPS)*, Sep. 2017, pp. 1–6.

[84] P. Romano, M. Paolone, T. Chau, B. Jeppesen, and E. Ahmed, "A high-performance, low-cost pmu prototype for distribution networks based on fpga," in *2017 IEEE Manchester PowerTech*, June 2017, pp. 1–6.

[85] C. G. C. Carducci, G. Lipari, N. Bosbach, T. D. Raimondo, F. Ponci, and A. Monti, "A versatile low-cost os-based phasor measurement unit,"

in *2019 IEEE International Instrumentation and Measurement Technology Conference (I2MTC)*, May 2019, pp. 1–6.

[86] IEEE, "IEEE standard for synchrophasor measurements for power systems," *IEEE Std C37.118.1-2011 (Revision of IEEE Std C37.118-2005)*, pp. 1–61, Dec. 2011.

[87] ——, "IEEE standard for synchrophasor measurements for power systems – amendment 1: Modification of selected performance requirements," *IEEE Std C37.118.1a-2014 (Amendment to IEEE Std C37.118.1-2011)*, pp. 1–25, Apr. 2014.

[88] *IEEE/IEC International Standard - Measuring relays and protection equipment - Part 118-1: Synchrophasor for power systems - Measurements*, IEEE/IEC IEC/IEEE 60255-118-1:2018, Dec 2018.

[89] S. H. Mortazavi, Z. Moravej, and S. M. Shahrtash, "A searching based method for locating high impedance arcing fault in distribution networks," *IEEE Transactions on Power Delivery*, vol. 34, no. 2, pp. 438–447, April 2019.

[90] S. F. Alwash, V. K. Ramachandaramurthy, and N. Mithulananthan, "Fault-location scheme for power distribution system with distributed generation," *IEEE Transactions on Power Delivery*, vol. 30, no. 3, pp. 1187–1195, June 2015.

[91] S. Das, N. Karnik, and S. Santoso, "Distribution fault-locating algorithms using current only," *IEEE Transactions on Power Delivery*, vol. 27, no. 3, pp. 1144–1153, July 2012.

[92] D. Carta, P. A. Pegoraro, S. Sulis, M. Pau, F. Ponci, and A. Monti, "A compressive sensing approach for fault location in distribution grid branches," in *2019 International Conference on Smart Energy Systems and Technologies (SEST)*, Sep. 2019, pp. 1–6.

[93] M. Stanbury and Z. Djekic, "The impact of current-transformer saturation on transformer differential protection," *IEEE Transactions on Power Delivery*, vol. 30, no. 3, pp. 1278–1287, June 2015.

[94] "ALTEA CVS-24-I-WB data sheet," Altea Solutions, Amsterdam, Netherlands. [Online]. Available: http://www.alteasolutions.com/pdf/Technical%20specifications%20CVS-24-I-WB%20Altea.pdf

[95] "ABB KEVCD A data sheet," ABB. [Online]. Available: https://search-ext.abb.com/library/Download.aspx?DocumentID=

1VLC000588%20Rev%20.%20en&LanguageCode=en&DocumentPartId=
&Action=Launch

[96] IEC, "Instrument transformers - Part 2: Additional requirements for current transformers," *Standard IEC 61869-2*, 2012.

List of Figures

List of Tables

Acronyms

BOMP Block-Orthogonal Matching Pursuit

BPDN Basis Pursuit with Denoise

CS Compressive Sensing

CSHD Compressive Sensing Harmonics Detector

CT Current Transformer

DSO Distribution System Operator

FL Fault Location

FLISR Fault Location, Isolation and Supply Restoration

HHS Heavy Hitters on Steroids

HSE Harmonic Source Estimation

IEC International Electrotechnical Commission

IEEE Institute of Electrical and Electronic Engineers

LBOMP Load Block-Orthogonal Matching Pursuit

LPCT Low Power Current Transformers

LPVT Low Power Voltage Transformer

LV Low Voltage

MC Monte Carlo

MV Medium Voltage

NP non-deterministic polynomial acceptable problems

NSP Null Space Property

OMP Orthogonal Matching Pursuit

PMU Phasor Measurement Unit

POW Phase of Waveform

PQ Power Quality

REF Reference

RIP Restricted Isometry Property

RTDS Real Time Digital Simulator

SE State Estimation

STD Standard

THD Total Harmonic Distortion

TVE Total Vector Error

UTC Coordinated Universal Time

VT Voltage Transformer

WLS Weighted Least Square